Nanostructured Titanium Dioxide Thin Films Synthesized by Mist CVD for Applications in Metal Oxide Thin Film Gas Sensors

by

Qiang Zhang

Student ID Number: 1216005

A dissertation submitted to the
Engineering Course, Department of Engineering,
Graduate School of Engineering,
Kochi University of Technology,
Kochi, Japan

Doctor of Philosophy

Assessment Committee:
Supervisor: Prof. Chaoyang Li
Co-Supervisor: Prof. Toshiyuki Kawaharamura
Co-Supervisor: Prof. Hiroshi Furuta
Committee Member: Prof. Helmut Baumgart, Old Dominion University, Virginia, USA
Committee Member: Prof. Akimitsu Hatta

March 2020

Abstract

Nanostructured Titanium Dioxide Thin Films Synthesized by Mist CVD for Applications in Metal Oxide Thin Film Gas Sensors

Metal oxide gas sensors have been widely applied in various fields. Among the different types of metal oxide gas sensors, metal oxide thin-film gas sensors have attracted considerable interest, as they readily facilitate integration and miniaturization in structure. In addition, such thin-film gas sensors have higher sensitivity and shorter response time than thick film-type metal oxide gas sensors.

Recently, titanium dioxide (TiO_2) thin films have been investigated as a promising sensing material for application in various thin-film reducing gas sensors due to their outstanding sensing properties, chemical stability and electrical properties.

TiO_2 naturally crystallizes in three phases, which were known as rutile, anatase and brookite. The thermal stability of brookite phase TiO_2 is poorer than anatase phase and rutile phase TiO_2, which limits the application of brookite phase TiO_2. In addition, brookite is the most difficult TiO_2 phase to fabricate in thin-film form. Compared with rutile phase TiO_2 films, anatase phase TiO_2 has greater sensitivity to H_2 and volatile organic compound gases than rutile phase TiO_2.

Hitherto, anatase phase TiO_2 thin films have been synthesized by various techniques, including magnetron sputtering, high-vacuum chemical vapor deposition, atomic layer deposition, electron beam evaporation, and sol-gel method. However, it is a challenging endeavor to obtain pure anatase phase TiO_2 with good uniformity, high thermal stability and high crystallinity using current synthesis methods. Firstly, the TiO_2 thin films obtained by these conventional methods are mostly a mixture of anatase and rutile phase TiO_2. Although there are some reports on fabricating pure anatase phase TiO_2 films, their thermal stability is poor due to the presence of (112) surface in anatase phase TiO_2, which limits the application of anatase phase TiO_2 films as sensing material. Particularly, it is difficult to fabricate anatase phase TiO_2 thin films with good crystallinity by spray pyrolysis, conventional chemical vapor deposition, atomic layer deposition or high vacuum chemical vapor deposition.

In order to fabricate pure anatase phase TiO_2 film with good uniformity and high crystallinity, it is necessary to develop a novel synthesis method. According to our previous research experience, we found the mist chemical vapor deposition is a suitable method to synthesize metal oxide thin film, by which the growth orientation, uniformity and grain size of thin film could be precisely controlled. Therefore, mist chemical vapor deposition is expected to an alternative method to synthesize pure anatase phase TiO_2 thin films.

In this thesis, a mist chemical vapor deposition system with novel designed reaction chamber was applied to deposit pure anatase phase TiO_2 thin films. In order to enhance the surface area of TiO_2, TiO_2 films were coated onto ZnO nanorods to fabricate ZnO/TiO_2 core-shell nanostructures.

Until now, there remain a number of shortcomings and challenges in state-of-the-art anatase phase TiO_2 based thin-film gas sensors:

(1) The fabricated TiO_2 is mostly a mixture of rutile phase and anatase phase. The fabrication of pure anatase phase TiO_2 is difficult.

(2) The properties of anatase phase TiO_2 (including uniformity, surface area and crystallinity) are still insufficient, which limits the performance of gas sensor.

(3) Due to the high surface energy, the {001} facets of anatase phase TiO_2 could significantly enhanced the gas sensitivity. However, it was difficult to enhance the growth of {001} facets with conventional methods.

(4) The working temperature of gas sensors are still high (over 200 °C).

(5) The response time and recovery time of gas sensors are too long.

(6) The cost of some methods for gas sensors fabrication is relatively high, such as RF sputtering and ALD method.

(7) The thermal stability of anatase phase TiO_2 based thin-film gas sensors is poor.

(8) The sensitivity to some gases (H_2, methanol) is still low.

In my research, I addressed the shortcomings of state-of-the-art TiO_2 gas sensors and some of the above challenges were solved. In particular, the following objectives were achieved:

(1) Pure anatase phase TiO_2 was successfully fabricated by mist chemical vapor deposition method.

(2) The obtained pure anatase phase TiO_2 showed excellent uniformity, high crystallinity and relative high surface area with nanosheet morphology.

(3) The growth of the anatase phase TiO_2 {001} facets was significantly enhanced by using methanol as solvent.

(4) Pure anatase phase TiO_2 based gas sensor could be fabricated by mist chemical vapor deposition with potentially lower cost.

(5) The obtained anatase phase TiO_2 showed an ultra-high thermal stability.

(6) The surface-to-volume ratio was significantly increased by synthesizing TiO_2 nanosheets as a coating on a high density of nanorods.

Academic novelty or originality of the research

(1) Pure anatase phase TiO_2 films were fabricated by mist CVD method for the first time.

(2) The mechanism of fabricating anatase phase TiO_2 films from TTIP by mist CVD was investigated for the first time.

(3) A new method was found to effectively enhance the growth of {001} facets of pure anatase phase TiO_2 by using methanol as solvent.

The main work will be discussed in terms of fabrication of anatase phase TiO_2 thin films with ethanol as solvent, fabrication of anatase phase TiO_2 thin films with methanol as solvent to optimize {001} facets, and fabrication of ZnO nanorods receiving mist CVD coatings of TiO_2 nanosheets for fabricating ZnO/TiO_2 core-shell nanorods.

1. Fabrication of anatase phase TiO_2 thin films with ethanol as solvent

In order to solve the issues of fabrication pure anatase phase TiO_2 films with good uniformity, high thermal stability, and high crystallinity, a mist chemical vapor deposition system with novel designed reaction chamber was applied to deposit pure anatase phase TiO_2 thin films. The effects of deposition temperature, concentration of titanium tetraisopropoxide precursor, film thickness and substrate on the properties of TiO_2 films were investigated.

The crystallinity of TiO_2 films was significantly improved by increasing deposition temperature. Pure anatase phase TiO_2 films with good uniformity were obtained from 300 °C to 400 °C. The roughness of all TiO_2 films was less than 7 nm and showed a variation tendency to increase as the deposition temperature increased from 200 °C to 400 °C.

The crystallinity of TiO_2 films showed a variation tendency to increase as the titanium tetraisopropoxide concentration increased from 0.05 mol/L to 0.40 mol/L. The best crystallinity was obtained under the titanium tetraisopropoxide concentration of 0.05 mol/L. The roughness of all TiO_2 films was less than 10 nm regardless of titanium tetraisopropoxide concentration variation. The crystallinity of TiO_2 films increases with the increase of film thickness. The surface of obtained TiO_2 films with different thicknesses are uniform. With the thickness increasing, the roughness of TiO_2 film shows a tendency of further increase.

The TiO_2 films deposited on all substrates showed the same dominant (101) growth orientation. The crystallinity of TiO_2 films grown on different substrates increased in an order of glass, quartz glass, p-type silicon and gallium oxide doped ZnO. It was confirmed by Raman spectroscopy and GIXRD that TiO_2 films deposited on four kinds of substrates were pure anatase phase. The TiO_2 thin film deposited on p-type silicon showed the highest percentage of exposed {001} facets. The TiO_2 films with good uniformity were obtained on all of the substrates. The surface area of TiO_2 films deposited on p-type silicon substrate was larger than that of TiO_2 films deposited on quartz glass, glass and gallium oxide doped ZnO substrates. The TiO_2 film deposited on p-type silicon is expected to have higher gas sensitivity and be applicable to thin film gas sensors.

In summary, pure anatase phase TiO_2 films with excellent uniformity, excellent thermal stability, high crystallinity and relative high surface area were successfully fabricated by mist chemical vapor deposition method.

2. Fabrication of anatase phase TiO_2 thin films with methanol as solvent

In order to control the deposition rate of TiO_2 and the growth of preferred {001} facets well, a

methanol based precursor solution was developed.

Compared with ethanol, methanol is much easier to atomize ultrasonically. The deposition rate of TiO_2 thin films will be more controllable by using methanol as a solvent. However, the titanium tetraisopropoxide is not stable in pure methanol. Recently, we obtained a stable mixture of titanium tetraisopropoxide and methanol by adding acetylacetone as stabilizer.

Until now, the growth of preferred {001} facets could be controlled only by a few methods. Among these approaches, the F- ion methods were mostly used to enhance the growth of {001} facets because F- could be strongly absorbed on {001} facets. However, F- is a dangerous ion which is corrosive to the fabrication equipment and harmful to human skin. Compared with the use of F-, we found that changing the water-to-methanol ratio is a safer method to control the growth of {001} facets.

In this part, pure anatase phase TiO_2 films were fabricated on aluminum oxide doped ZnO and glass substrates with methanol as a solvent by mist chemical vapor deposition. The effects of film thickness and water-to-methanol ratio on the properties of TiO_2 films were investigated.

Uniform TiO_2 films with different thicknesses were obtained. With the thickness increasing, the roughness and surface area of TiO_2 film showed a tendency to increase. The crystallinity of TiO_2 films increases with the increasing of film thickness. With the thickness increasing, the optical transmittance of TiO_2 films decreased from around 80 % to around 65 % gradually.

During the deposition, the growth of {001} facets and surface area were significantly influenced by the water-to-methanol ratio. By decreasing the water-to-methanol ratio, the growth of {001} facets was enhanced, while the growth of {101} facets was suppressed. The surface roughness and surface area of TiO_2 films showed the same trend of increasing with a decrease of the water-to-methanol ratio. The highest surface roughness and maximized surface area was obtained with a water-to-methanol of 0 %. The transmittance of all TiO_2 films was higher than 70 % in the visible region. The photocatalytic efficiency of TiO_2 films showed an increasing trend with the decrease of the water-to-methanol ratio. The TiO_2 films deposited with pure methanol as solvent showed the highest photocatalytic efficiency due to a maximum number of {001} facets and an optimum surface area.

In summary, pure anatase phase TiO_2 films with excellent uniformity and relative high surface area were successfully fabricated by mist chemical vapor deposition method. The methanol system was found to be a new method to effectively enhance the growth of {001} facets of pure anatase phase TiO_2.

3. Fabrication of ZnO nanorods and ZnO/TiO_2 core-shell nanorods.

In order to further enlarge the surface-to-volume ratio of TiO based gas sensors, TiO_2 films were deposited onto the surface of a dense array of ZnO nanorods by mist chemical deposition.

In this part, a dense array of ZnO nanorods and a dense array of ZnO/TiO_2 core-shell nanorods were fabricated on conductive aluminum oxide doped ZnO seed films. The effects of solution concentration and deposition time on the properties of ZnO nanorods were investigated. The effects

of TiO_2 film coating time on the properties of ZnO/TiO_2 core-shell nanorods were investigated.

The solution concentration had a significant influence on the morphological, structural, and optical properties of ZnO nanorods. It was found that well-arrayed ZnO nanorods with hexagonal structure were obtained with solution concentration ranging from 100 % to 40 %. With the decreasing of solution concentration, the crystallinity of ZnO nanorods showed a tendency of decrease, and the transmittance of ZnO nanorods increased gradually in the visible range. Oxygen vacancies and oxygen interstitials inside of ZnO nanorods were confirmed by PL measurements.

The morphological, structural and optical properties of ZnO nanorods were significantly influenced by the deposition time. A dense array of ZnO nanorods with hexagonal structure were obtained with a deposition time of 5 hours and 10 hours. With the deposition time increasing from 5 hours to 10 hours, the crystallinity of ZnO nanorods increased significantly, and the transmittance of ZnO nanorods in the visible region decreased from around 75 % to around 35 %.

The TiO_2 wrap-around shell coatings on ZnO nanorods were confirmed as pure anatase phase, which will contribute to high chemical stability as photoanodes. The surface area of ZnO nanorods was significantly increased with increase in TiO_2 coating time. The transmittance of ZnO nanorods decreased from 75 % to 65 % after 15 minutes coating TiO_2. The dense array of ZnO/TiO_2 core-shell nanorods will contribute to excellent chemical stability, and relatively large surface-to-volume ratio for gas absorption, which are expected to be applied as sensing material to improve the performance of gas sensors.

In summary, a dense array of ZnO nanorods were successfully fabricated by chemical bath deposition. ZnO/TiO_2 core-shell nanorods with large surface area were successfully fabricated by coating nanostructured pure anatase phase TiO_2 films onto the surface of ZnO nanorods by mist chemical vapor deposition method.

List of Figures

Fig. 1.1 Texture of TiO_2.....1
Fig. 1.2 TiO_2 tubular nanostructures prepared by different methods.....2
Fig. 1.3 TiO_2 nanobelts prepared by different methods.....3
Fig. 1.4 3D dendritic TiO_2 nanostructures prepared by different methods.....3
Fig. 2.1 The diagrammatic sketch of mist CVD process.....11
Fig. 2.2 The diagrammatic sketch of CBD apparatus.....12
Fig. 2.3 The diagrammatic sketch of RF sputtering apparatus.....13
Fig. 2.4 Schematic of a typical scanning electron microscope and imaging process.....14
Fig. 2.5 FE-SEM instrument.....14
Fig. 2.6 XRD instrument.....16
Fig. 2.7 The schematic diagram of PL spectroscopy measurement.....17
Fig. 2.8 The instrument of PL spectroscopy.....17
Fig. 2.9 Raman spectroscopy instrument.....18
Fig. 2.10 U-4100 UV-Vis-IR spectrophotometer.....19
Fig. 2.11 The schematic diagram of AFM measurement.....20
Fig. 2.12 AFM instrument.....20
Fig. 2.13 Gas sensitivity evaluation system.....21
Fig. 3.1 XRD patterns of TiO_2 films deposited under different temperatures using the mist CVD method.....25
Fig. 3.2 AFM images of TiO_2 films deposited under different temperatures using the mist CVD method. ((**a**) 200 °C; (**b**) 250 °C; (**c**) 300 °C; (**d**) 350 °C; (**e**) 400 °C).....26
Fig. 3.3 Reaction rate constant of TTIP pyrolysis and hydrolysis reactions under different temperatures.....28
Fig. 3.4 Mechanism of TiO_2 films deposition during the mist CVD process.....29
Fig. 3.5 SEM images of TiO_2 films deposited with different TTIP concentrations by mist CVD. ((**a**) 0.05 mol/L; (**b**) 0.10 mol/L; (**c**) 0.20 mol/L; (**d**) 0.30 mol/L; (**e**) 0.40 mol/L; (**1**) top view; (**2**) cross section view).....31
Fig. 3.6 Deposition rate and aspect ratio of TiO_2 nanosheets.....32
Fig. 3.7 AFM images of TiO_2 films deposited with different TTIP concentrations by mist CVD. ((**a**) 0.05 mol/L; (**b**) 0.10 mol/L; (**c**) 0.20 mol/L; (**d**) 0.30 mol/L; (**e**) 0.40 mol/L).....32
Fig. 3.8 GIXRD results of TiO_2 films deposited with different TTIP concentrations by mist CVD. ((**a**) GIXRD patterns of TiO_2 films; (**b**) (101) peak intensity and FWHM of TiO_2 films).....33
Fig. 3.9 High-resolution XPS spectra of TiO_2 films deposited with different TTIP concentrations by

mist CVD. ((**a**) O 1s; (**b**) Ti 2p).....35
Fig. 3.10 Raman spectra of TiO_2 films deposited with different TTIP concentrations by mist CVD.....36
Fig. 3.11 Transmittance of TiO_2 films deposited with different TTIP concentrations by mist CVD.....36
Fig. 3.12 GIXRD patterns of TiO_2 films with different thicknesses deposited by mist CVD.....38
Fig. 3.13 Raman spectra of TiO_2 films with different thicknesses deposited by mist CVD.....39
Fig. 3.14 AFM images of TiO_2 films deposited with different thicknesses by mist CVD method. ((**a**) 100 nm; (**b**) 200 nm; (**c**) 300 nm; (**d**) 400 nm; (**e**) 500 nm).....39
Fig. 3.15 Transmittance of TiO_2 films deposited with different thicknesses by mist CVD.....40
Fig. 3.16 GIXRD results of TiO_2 films deposited on different substrates by mist CVD. ((**a**) GIXRD patterns of TiO_2 films; (**b**) GIXRD intensity of TiO_2 films).....42
Fig. 3.17 Raman results of TiO_2 films deposited on different substrates by mist CVD. ((**a**) Raman spectra of TiO_2 films; (**b**) Raman intensity of TiO_2 films).....44
Fig. 3.18 AFM images of TiO_2 films deposited on different substrates by mist CVD. ((**a**), (**e**): quartz glass; (**b**), (**f**): glass; (**c**), (**g**): GZO; (**d**), (**h**): silicon).....45
Fig. 3.19 SEM images of TiO_2 films deposited on different substrates by mist CVD. ((**a**) quartz glass; (**b**) glass; (**c**) GZO; (**d**) silicon; (**1**) top view; (**2**) cross section view).....46
Fig. 3.20 Transmittance of TiO_2 films deposited on different substrates by mist CVD.....47
Fig. 4.1 SEM images of TiO_2 films deposited with different thicknesses by mist CVD method. ((**a**) 100 nm; (**b**) 200 nm; (**c**) 300 nm; (**d**) 400 nm; (**e**) 500 nm).....56
Fig. 4.2 AFM images of TiO_2 films deposited with different thicknesses by mist CVD method. ((**a**) 100 nm; (**b**) 200 nm; (**c**) 300 nm; (**d**) 400 nm; (**e**) 500 nm).....56
Fig. 4.3 GIXRD patterns of TiO_2 films with different thicknesses deposited by mist CVD.....57
Fig. 4.4 Raman spectra of TiO_2 films with different thicknesses deposited by mist CVD.....58
Fig. 4.5 Transmittance of TiO_2 films deposited with different thicknesses by mist CVD.....59
Fig. 4.6 SEM images of TiO_2 films deposited under different water-to-methanol ratio by mist CVD. ((**a**) 20 %; (**b**) 10 %; (**c**) 5 %; (**d**) 1 %; (**e**) 0 %).....61
Fig. 4.7 AFM images of TiO_2 films deposited under different water-to-methanol ratio by mist CVD. ((**a**) 20 %; (**b**) 10 %; (**c**) 5 %; (**d**) 1 %; (**e**) 0 %).....62
Fig. 4.8 GIXRD results of TiO_2 films deposited under different water-to-methanol ratio by mist CVD. ((**a**) GIXRD patterns of TiO_2 films; (**b**) GIXRD intensity of TiO_2 films).....63
Fig. 4.9 Raman spectra of TiO_2 films deposited under different water-to-methanol ratio by mist CVD.....64
Fig. 4.10 Transmittance of TiO_2 films deposited under different water-to-methanol ratio by mist CVD.....65
Fig. 4.11 The result of MR solution photodegradation by TiO_2 films deposited under different water-

to-methanol ratio by mist CVD. ((**a**) absorption spectra of MR solution; (**b**) the concentration of MR solution after photodegradation) 66
Fig. 5.1 SEM images of ZnO nanorods deposited with different solution concentrations. ((**a**) 100 %; (**b**) 80 %; (**c**) 60 %; (**d**) 40 %; (**e**) 20 %; (**1**) top view; (**2**) cross section view) 72
Fig. 5.2 XRD results of ZnO nanorods deposited with different solution concentrations. ((**a**) XRD patterns of ZnO nanorods; (**b**) intensity and FWHM of XRD peaks).....73
Fig. 5.3 Transmission spectra of ZnO nanorods deposited with different solution concentrations...74
Fig. 5.4 PL spectra of ZnO nanorods deposited with different solution concentrations.....74
Fig. 5.5 SEM images of ZnO nanorods deposited with different time. ((**a**) 5 h; (**b**) 10 h; (**1**) top view; (**2**) cross section view).....76
Fig. 5.6 XRD patterns of ZnO nanorods deposited with different time.....77
Fig. 5.7 Transmission spectra of ZnO nanorods deposited with different time.....77
Fig. 5.8 Mechanism of ZnO/TiO_2 core-shell nanorods fabrication.....80
Fig. 5.9 SEM images of (**a**) as-deposited ZnO nanorods and ZnO nanorods coated with TiO_2 by mist CVD ((**b**) 30s; (**c**) 2 min; (**d**) 5min; (**e**) 10min; (**f**) 15 min; (**1**) top view; (**2**) cross section view).....81
Fig. 5.10 The EDS elemental mapping images of ZnO nanorods coated with TiO_2 for 10 minutes ((**a**) FE-SEM image; (**b**) zinc element mapping image; (**c**) titanium element mapping image; (**d**) oxygen element mapping image).....82
Fig. 5.11 GIXRD patterns of as-deposited ZnO nanorods and ZnO nanorods coated with TiO_2 by mist CVD.....83
Fig. 5.12 Raman spectra of as-deposited ZnO nanorods and ZnO nanorods coated with TiO_2 by mist CVD.....84
Fig. 5.13 (**a**) PL spectra of TiO_2 film on glass, as-deposited ZnO nanorods and ZnO nanorods coated with TiO_2 by mist CVD; (**b**) PL spectra curve fitting of as-deposited ZnO nanorods; (**c**) PL spectra curve fitting of ZnO nanorods coated with TiO_2 for 10 min.....86
Fig. 5.14 (**a**) Transmission spectra of as-deposited ZnO nanorods and ZnO nanorods coated with TiO_2 by mist CVD; (**b**) Variation of $(ahv)^2$ of the as-deposited ZnO nanorods and ZnO nanorods coated with TiO_2 as a function of the photon energy (hv).....88
Fig. 6.1 Schematic depiction of the sensing mechanism of TiO_2 nanosheet exposed to ethanol vapors.....94
Fig. 6.2 Schematics of band diagram compared with the grain boundary when TiO_2 nanosheets surface is exposed to oxygen and ethanol vapor.....95
Fig. 6.3 Schematic diagram of the TiO_2 sensor upon exposure to the reducing gas.....96
Fig. 6.4 Gas sensitivity measurement result (with different working temperatures) of TiO_2 films deposited with a TTIP concentration of 0.40 mol/L.....97
Fig. 6.5 Gas sensitivity measurement result (with a working temperature of 320 °C) of TiO_2 films

deposited with a TTIP concentration of 0.40 mol/L.....98
Fig. 6.6 Gas sensitivity measurement result (with a working temperature of 300 °C) of TiO_2 films deposited with different TTIP concentrations.....98

List of Tables

Table 3.1 Deposition condition of temperature dependence.....24
Table 3.2 Surface roughness of TiO_2 films deposited under different temperatures. 26
Table 3.3 Deposition condition of TTIP concentration dependence.....30
Table 3.4 Surface roughness of TiO_2 films deposited with different TTIP concentrations.....33
Table 3.5 Deposition condition of film thickness dependence.....37
Table 3.6 Surface roughness of TiO_2 films with different thicknesses.....39
Table 3.7 Deposition condition of substrate dependence.....41
Table 3.8 Value of texture coefficient.....43
Table 3.9 Surface roughness and surface area of TiO_2 films deposited on different substrates.....45
Table 4.1 Deposition condition of AZO film.....55
Table 4.2 Deposition condition of film thickness dependence.....55
Table 4.3 Surface roughness and surface area of TiO_2 films with different thicknesses.....57
Table 4.4 Deposition condition of water-to-methanol ratio dependence.....60
Table 4.5 Surface roughness and surface area of glass and TiO_2 films.....63
Table 5.1 Deposition condition of ZnO nanorods with different solution concentration.....71
Table 5.2 Deposition condition of ZnO nanorods with different deposition time.....75
Table 5.3 Deposition condition of ZnO nanorods.....78
Table 5.4 Deposition condition of TiO_2 coating.....79

Contents

List of Figures VII

List of Tables XI

Chapter 1 Introduction 1

1.1 Basic properties of TiO_2 1

1.2 Introduction of TiO_2 based gas sensor 2

1.3 Fabrication issues of TiO_2 thin film based gas sensors 4

1.4 Objectives and structure of this thesis 5

1.5 References 7

Chapter 2 Fabrication equipment and characterization techniques 10

2.1 Introduction 10

2.2 Fabrication equipment 10

2.2.1 Mist chemical vapor deposition 10

2.2.2 Chemical bath deposition 11

2.2.3 Radio frequency magnetron sputtering system 12

2.3 Characterization techniques 13

2.3.1 Field emission scanning electron microscope 13

2.3.2 X-ray diffraction 15

2.3.3 Photoluminescence spectroscopy 16

2.3.4 Raman spectroscopy 18

2.3.5 Spectrophotometer 18

2.3.6 Atomic force microscopy 19

2.3.7 Gas sensitivity measurement system 21

2.4 References 22

Chapter 3 Fabrication and characterization of anatase phase TiO_2 thin films with ethanol as solvent by mist CVD method 23

3.1 Introduction 23

3.2 Effects of deposition temperature on the properties of TiO_2 thin films 24

3.2.1 Experimental 24

3.2.2 Results and discussion 24
3.2.3 Summary 29
3.3 Effects of TTIP concentration on the properties of TiO_2 thin films 29
3.3.1 Experimental 29
3.3.2 Results and discussion 30
3.3.3 Summary 36
3.4 Effects of film thickness on the properties of TiO_2 thin films 37
3.4.1 Experimental 37
3.4.2 Results and discussion 37
3.4.3 Summary 40
3.5 Effects of substrate on the properties of TiO_2 thin films 40
3.5.1 Experimental 40
3.5.2 Results and discussion 41
3.5.3 Summary 47
3.6 Conclusions 47
3.7 References 49
Chapter 4 Fabrication and characterization of anatase phase TiO_2 thin films with methanol as solvent by mist CVD method 53
4.1 Introduction 53
4.2 Effects of film thickness on the properties of TiO_2 thin films 54
4.2.1 Experimental 54
4.2.2 Results and discussion 55
4.2.3 Summary 59
4.3 Effects of water to methanol ratio on the properties of TiO_2 thin films 59
4.3.1 Experimental 59
4.3.2 Results and discussion 60
4.3.3 Summary 66
4.4 Conclusions 66
4.5 References 68
Chapter 5 Fabrication and characterization of ZnO nanorods and ZnO-TiO_2 core-shell nanorods by chemical bath deposition and mist CVD

method **70**
5.1 Introduction 70
5.2.1 Experimental 71
5.2.2 Results and discussion 71
5.2.3 Summary 75
5.3 Effects of deposition time on the properties of ZnO nanorods 75
5.3.1 Experimental 75
5.3.2 Results and discussion 75
5.3.3 Summary 78
5.4 Fabrication and characterization of ZnO-TiO_2 core-shell nanorods 78
5.4.1 Experimental 78
5.4.2 Results and discussion 79
5.4.3 Summary 88
5.5 Conclusions 88
5.6 References 90
Chapter 6 Gas sensitivity characterization of TiO_2 thin films **93**
6.1 Introduction 93
6.2 Experimental 96
6.3 Results and discussion 97
6.4 Conclusions 99
6.5 References 100
Chapter 7 Conclusions **101**
List of publications **104**
Acknowledgements **107**

Chapter 1

Introduction

1.1 Basic properties of TiO_2

Titanium dioxide (TiO_2) is a metal oxide semiconductor with wide direct bandgap around 3.2 eV [1]. Recently, TiO_2 have attracted considerable interest because of their outstanding properties, such as chemical stability, electrical and optical properties, especially a wide band gap of around 3.2 eV [1-2].

TiO_2 naturally crystallizes in three phases, which were known as rutile, anatase and brookite. The structures of three phases TiO_2 were shown in Fig. 1.1 [3]. As shown in Fig. 1.1, rutile phase and anatase phase TiO_2 showed a tetragonal structure, and brookite phase TiO_2 showed an orthorhombic structure. The thermal stability of brookite phase TiO_2 is poorer than anatase phase and rutile phase TiO_2, which limits the application of brookite phase TiO_2. In addition, brookite is the most difficult TiO_2 phase to fabricate in thin-film form [4,5]. Compared with rutile phase TiO_2 films, anatase phase TiO_2 has greater sensitivity to H_2 and volatile organic compound gases than rutile phase TiO_2 [6,7].

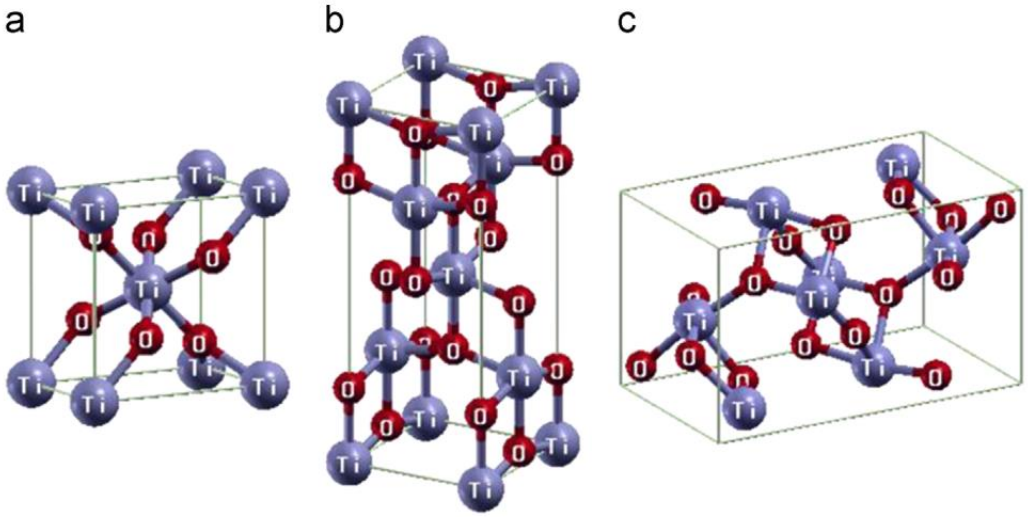

Fig. 1.1 Texture of TiO_2 ((a) rutile; (b) anatase; (c) brookite) [4].

1.2 Introduction of TiO_2 based gas sensor

Recently, TiO_2 nanomaterials with different compositions and structures (as shown in Fig. 1.2, Fig. 1.3 and Fig. 1.4) have been applied to various sensors, including biosensor, environmental sensor, electric sensor, optical sensor, gas sensor. As a typical n-type semiconductor, TiO_2 based gas sensor is favored due to its fast response, high gas sensitivity, long lifetime, excellent chemical stability, and low cost. TiO_2 shows an extensive gas sensitivity to both oxidative gases (NO_2, O_2) and reductive gases (H_2, H_2S, NH_3, CO, VOCs). Normally, the microscopic reactions between these gases and TiO_2 surface are much different, the sensing mechanism is more complicated, and the sensor performance could be affected by many factors [8]. The sensing mechanism of TiO_2 based gas sensors can be explained by the following processes.

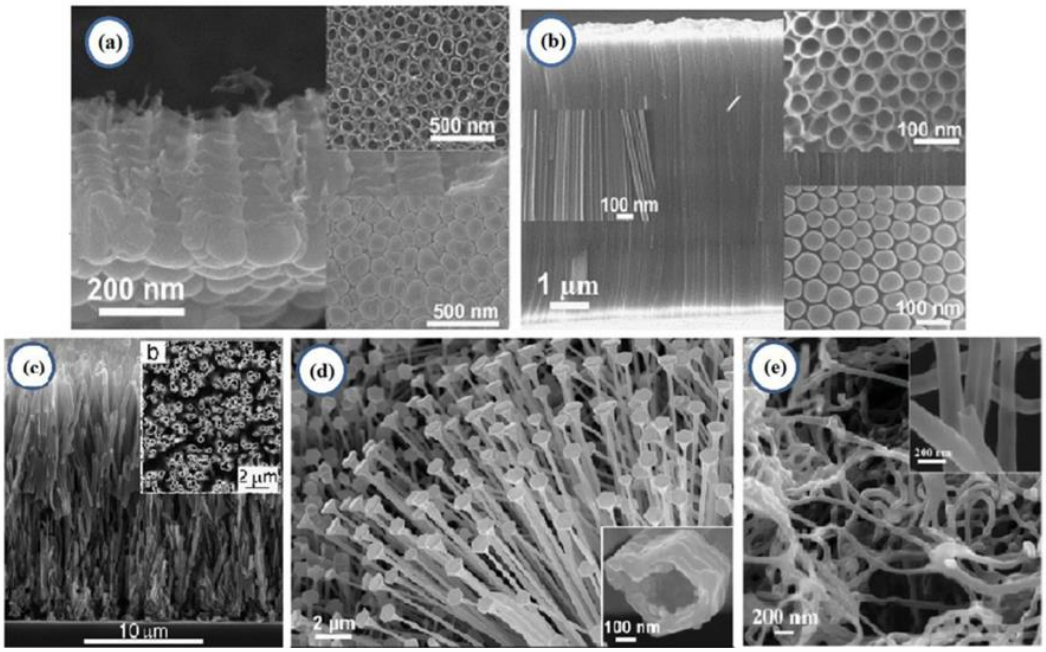

Fig. 1.2 TiO_2 tubular nanostructures prepared by different methods [8].

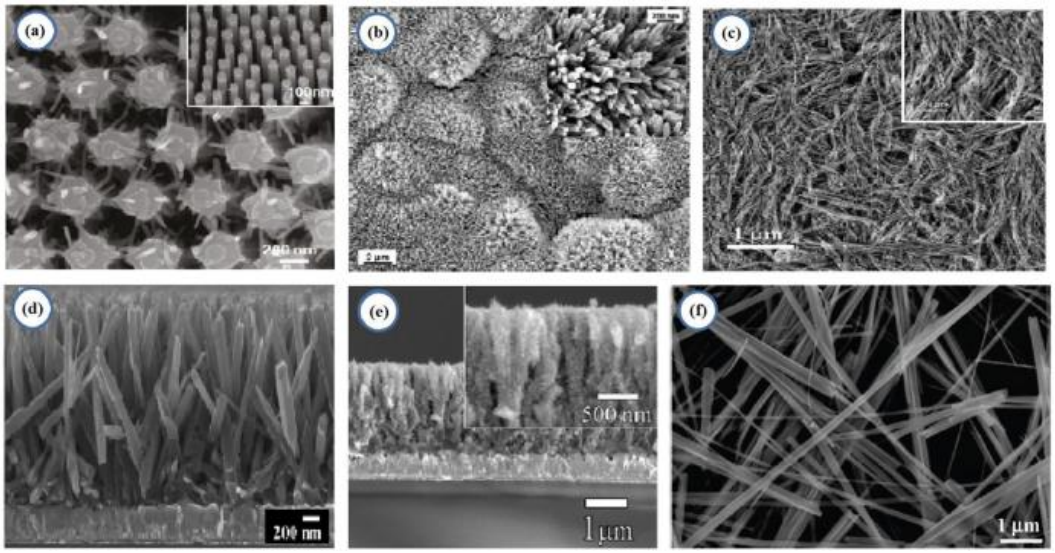

Fig. 1.3 TiO_2 nanobelts prepared by different methods [8].

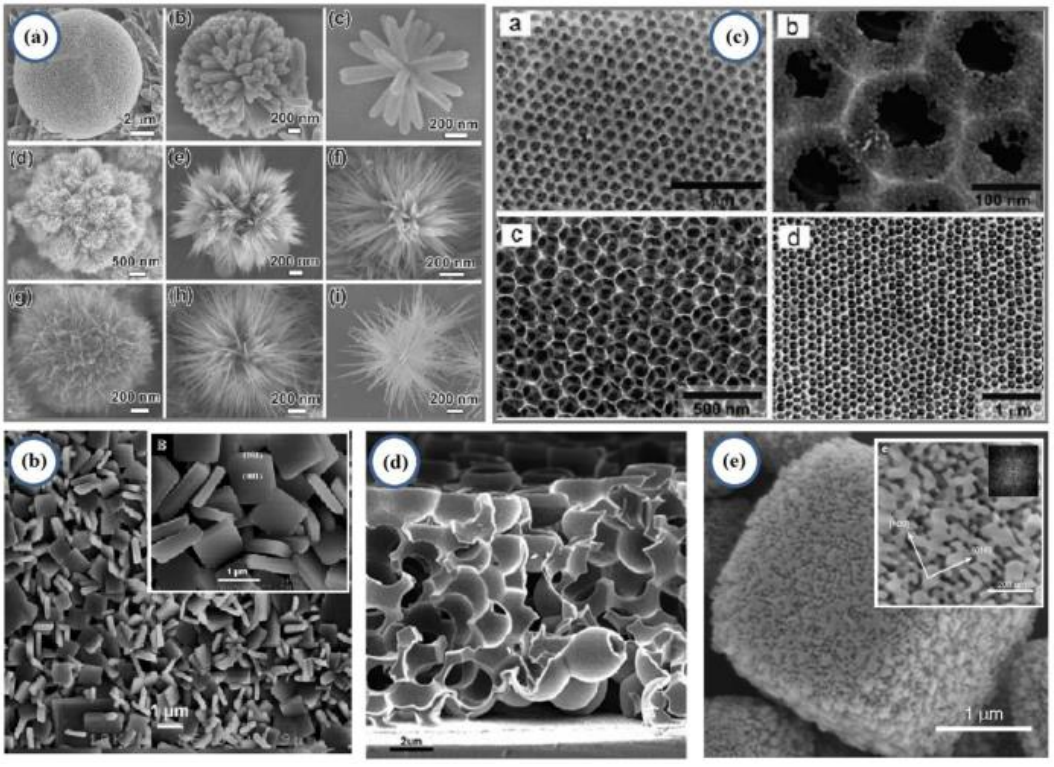

Fig. 1.4 3D dendritic TiO_2 nanostructures prepared by different methods [8].

When the TiO_2 film is exposed to air, due to the surface oxygen vacancies, oxygen molecules are easily absorbed on the surface of TiO_2 and form oxygen ions. Therefore, the electron density of the TiO_2 surface will be reduced (even changed into p-type), which will form depletion layer

and band bending on the film surface. The band bending on the surface of TiO_2 grains will cause a barrier for carrier transport between the grains, which will decrease the conductivity of TiO_2 film.

When the TiO_2 film is exposed to reductive gases, the gas molecules will be adsorbed and react with oxygen ions, which will cause a transfer of electrons back to the surface of TiO_2. Therefore, the thickness of depletion layer will be reduced and the band bending will be released. As a result, the conductivity of TiO_2 film will be improved. When the TiO_2 film is exposed to oxidative gases, the gas molecules will be adsorbed on the surface oxygen ions. The oxidative gases will attract electrons from oxygen ions, which will increase the depletion layer thickness and decrease the conductivity [1,6,7-13].

The conductivity variation of TiO_2 films can be easily converted to resistance signal. Thus, the oxidative gases and reductive gases can be detected by analyzing the resistance signal of TiO_2 films.

1.3 Fabrication issues of TiO_2 thin film based gas sensors

Hitherto, anatase phase TiO_2 thin films have been synthesized by various techniques, including magnetron sputtering, high-vacuum chemical vapor deposition (HV-CVD), atomic layer deposition (ALD), electron beam evaporation, and sol-gel method [1,12-25]. However, the obtained TiO_2 thin films obtained by these methods are mostly a mixture of anatase and rutile phase TiO_2 [21-26]. Although there are some reports on fabricating pure anatase phase TiO_2 films, their thermal stability is poor [14,24,28] due to the presence of (112) surface in anatase phase TiO_2 [27-31], which limits the application of anatase phase TiO_2 films as sensing material.

Until now, it is still strict issue to obtain pure anatase phase TiO_2 with good uniformity and high crystallinity using current synthesis methods [12,20-22,32-38]. Particularly, it is difficult to fabricate anatase phase TiO_2 thin films with good crystallinity by spray pyrolysis, conventional chemical vapor deposition, atomic layer deposition or high vacuum chemical vapor deposition. When these methods are applied with a low deposition temperature (not higher than 350 ˚C), the deposition of anatase phased TiO_2 film is kinetically controlled [1], which means the growth of anatase phased TiO_2 film is limited by low decomposition rate of precursor. As a result, the crystallinity of obtained TiO_2 film is poor [21,35,36]. When deposition temperature is increased, the deposition will become controlled by mass transport [1], and the growth of anatase phased

TiO_2 film is limited by the lack of precursor, resulting in a poor thickness uniformity of deposited TiO_2 film [21,37,38].

Moreover, for anatase phase TiO_2, due to the high surface energy, the {001} facets were more reactive for the adsorption of gases and the photodegradation of organic pollutants, which significantly enhanced the gas sensitivity and photocatalytic activity of the pure anatase phase TiO_2 [39,40]. However, for most anatase TiO_2 film deposition methods, it is difficult to control the growth of {001} facets. Thus, the anatase TiO_2 films obtained by these methods suffer from a low gas sensitivity and a low photocatalytic efficiency in the gas sensing application. Until now, the growth of preferred {001} facets could be controlled by only a few methods. Among these approaches, the F^- ion methods were mostly used to enhance the growth of {001} facets because F^- could be strongly absorbed on {001} facets. However, F^- is a dangerous ion, which is corrosive to the fabrication equipment and harmful to human skin.

In order to fabricate pure anatase phase TiO_2 film with good uniformity, high crystallinity, high thermal stability and enhanced {001} facets, it is necessary to develop a novel synthesis method.

1.4 Objectives and structure of this thesis

This Ph.D. research is addressing the shortcomings of the commercial thin film synthesis method for anatase phase TiO_2 MOS gas sensors.

The present work is improving the state of the art in the anatase phase TiO_2 synthesis by developing a novel method of mist CVD, which improves the crystallinity, morphology, surface area, ratio of (001) facets and thermal stability, which will translate into the superior anatase TiO_2 gas sensors.

In my research, there are several academic novelties or originalities to improve performance of TiO_2 based gas sensor.

(1) Pure anatase phase TiO_2 films were fabricated by mist CVD method for the first time.

(2) The mechanism of fabricating anatase phase TiO_2 films from TTIP by mist CVD was investigated for the first time. Base on the calculation and investigation, the fabricating mechanism of TiO_2 films deposited from 300 °C to 400 °C was confirmed as the pyrolysis of TTIP.

(3) The methanol system was found to be a new method to effectively enhance the growth of {001} facets of pure anatase phase TiO_2.

The main work will be discussed in terms of fabrication of anatase phase TiO_2 thin films with ethanol as solvent, fabrication of anatase phase TiO_2 thin films with methanol as solvent, and fabrication of ZnO nanorods and ZnO/TiO_2 core-shell nanorods.

Chapter 1: Research background of TiO_2 material and TiO_2-based gas sensors including the development and applications was introduced in details. The objectives of thesis were proposed and the structure of thesis was settled.

Chapter 2: The principle and measurement methods of fabrication and characterization equipment were briefly introduced.

Chapter 3: Fabrication and characterization of anatase phase TiO_2 thin films with ethanol as solvent were investigated in detail.

Chapter 4: Fabrication and characterization of anatase phase TiO_2 thin films with methanol as solvent were investigated in detail.

Chapter 5: Fabrication and characterization of ZnO nanorods and ZnO-TiO_2 core-shell nanorods by chemical bath deposition and mist CVD method were investigated. The deposition and characterization of pure anatase TiO_2 film was also discussed in detail.

Chapter 6: The gas sensitivity of TiO_2 film and ZnO nanorods were evaluated. The effects of TiO_2 deposition conditions and the coating time on the gas sensitivity of DSSC were investigated.

Chapter 7: The main results of this thesis were summarized. The future improvement and application were discussed.

1.5 References

[1] M.V. Baryshnikova, L.A. Filatov, A.S. Petrov, S.E. Alexandrov. CVD deposited titania thin films for gas sensors with improved operating characteristics. Chem. Vap. Depos. 21 (2015) 327-333.

[2] T.-J. Ha, C.-S. Park, M.-H. Hong, H.-H. Park. Introduction of a pore connection network into mesoporous TiO_2 films to enhance CO gas sensitivity. J. Electrochem. Soc. 162 (2015) B180-B184.

[3] M. Mohamad, B.U. Haq, R. Ahmed, A. Shaari, N. Ali, R. Hussain. A density functional study of structural, electronic and optical properties of titanium dioxide: Characterization of rutile, anatase and brookite polymorphs. Mater. Sci. Semicond. Process. 31 (2015) 405-414.

[4] M.P. Moret, R. Zallen, D.P. Vijay, S.B. Desu. Brookite-rich titania films made by pulsed laser depositionThin Solid Films 366 (2000) 8-10.

[5] A.D. Paola, M. Bellardita, L. Palmisano. Brookite, the least known TiO_2 photocatalyst. Catalysts 3 (2013) 36-73.

[6] M. Epifani, A. Helwig, J. Arbiol, R. Díaz, L. Francioso, P. Siciliano, G. Mueller, J. R. Morante. TiO_2 thin films from titanium butoxide: synthesis, Pt addition, structural stability, microelectronic processing and gas-sensing properties. Sens. Actuators B Chem. 130 (2008) 599-608.

[7] E. Sennik, N. Kilinc, Z. Z. Ozturk. Electrical and VOC sensing properties of anatase and rutile TiO_2 nanotubes. J. Alloys Compd. 616 (2014) 89-96.

[8] J. Bai, B. Zhou. Titanium dioxide nanomaterials for sensor applications. Chemical reviews 114 (2014) 10131-10176.

[9] G. Sakai, N. Matsunaga, K. Shimanoe, N. Yamazoe. Theory of gas-diffusion controlled sensitivity for thin film semiconductor gas sensor. Sens. Actuators B Chem. 80 (2001) 125-131.

[10] J.R. Brown, M.T. Cheney, P.W. Haycock, D.J. Houlton, A.C. Jones, E.W. Williams. The gas-sensing properties of tin oxide thin films deposited by metallorganic chemical vapor deposition. J. Electrochem. Soc. 144 (1997) 295-299.

[11] J. Zhang, C. Zhao, P.A. Hu, Y.Q. Fu, Z. Wang, W. Cao, B. Yang, F. Placido. A UV light enhanced TiO_2/graphene device for oxygen sensing at room temperature. RSC Adv. 3 (2013) 22185-22190.

[12] B. Comert, N. Akin, M. Donmez, S. Saglam, S. Ozcelik. Titanium dioxide thin films as methane gas sensors. IEEE Sens. J. 16 (2016) 889-8896.

[13] D.S.R. Josephine, K.J. Babu, G.P.G. Kumar, K. Sethuraman. Titanium dioxide anchored graphene oxide nanosheets for highly selective voltammetric sensing of dopamine. Microchim. Acta 184 (2017) 781-790.

[14] L. Chen, X. Liao, W. Jiang. Effect of heat treatment temperature on super-hydrophilic property of enamels with titanium dioxide thin film. J. Sol-Gel Sci. Technol. 80 (2016) 606-611.

[15] V. Scuderi, M.A. Buccheri, G. Impellizzeri, A.D. Mauro, G. Rappazzo, K. Bergum, B.G. Svensson, V. Privitera. Photocatalytic and antibacterial properties of titanium dioxide flat film. Mater. Sci. Semicond. Process. 42 (2016) 32-35.

[16] B. Scheffel, T. Modes, C. Metzner. Reactive high-rate deposition of titanium oxide coatings using electron beam evaporation, spotless arc and dual crucible. Surf. Coat. Technol. 287 (2016) 138-144.

[17] M. Mazur. Analysis of the properties of functional titanium dioxide thin films deposited by pulsed DC magnetron sputtering with various O_2: Ar ratios. Opt. Mater. 69 (2017) 96-104.

[18] B. Karunagaran, P. Uthirakumar, S.J. Chung, S. Velumani, E.K. Suh. TiO_2 thin film gas sensor for monitoring ammonia. Mater. Charact. 58 (2007) 680–684.

[19] R. Klaysri, M. Ratova, P. Praserthdam, P.J. Kelly. Deposition of Visible Light-Active C-Doped Titania Films via Magnetron Sputtering Using CO_2 as a Source of Carbon. Nanomaterials 7 (2017) 113.

[20] K.-H. Choi, K.-B. Chung, H.-K. Kim. d-orbital ordering of oxygen-deficient amorphous and anatase TiO_2−x channels for high mobility thin film transistors. Appl. Phys. Lett. 102 (2013) 153511.

[21] C. Jin, B. Liu, Z. Lei, J. Sun. Structure and photoluminescence of the TiO_2 films grown by atomic layer deposition using tetrakis-dimethylamino titanium and ozone. Nanoscale Res. Lett. 10 (2015) 95-104.

[22] Y. Chimupala, G. Hyett, R. Simpson, R. Mitchell, R. Douthwaite, S.J. Milne, R.D. Brydson. Synthesis and characterization of mixed phase anatase TiO_2 and sodium-doped TiO_2(B) thin films by low pressure chemical vapour deposition (LPCVD). RSC Adv. 4 (2014) 48507-48515.

[23] T. Ban, T. Nakatani, Y. Ohya. Morphology of anatase crystals and their aggregates synthesized hydrothermally from aqueous mixtures of titanium alkoxide and different alkylammonium hydroxides. J. Ceram. Soc. Jpn. 117 (2009) 268-272.

[24] S.A. Campbell, H.S. Kim, D.C. Gilmer, B. He, T. Ma, W.L. Gladfelter. Titanium dioxide (TiO_2)-based gate insulators. IBM J. Res. Dev. 43 (1999) 383-392.

[25] J. Wu, S. Hao, J. Lin, M. Huang, Y. Huang, Z. Lan, P. Li. Crystal morphology of anatase titania nanocrystals used in dye-sensitized solar cells. Cryst. Growth Des. 8 (2008) 247-252.

[26] J. Zhang, J. Liao, F. Yang, M. Xu, S. Lin. Regulation of the electroanalytical performance of ultrathin titanium dioxide nanosheets toward lead ions by non-metal doping. Nanomaterials 7 (2017) 327.

[27] P.I. Gouma, M.J. Mills. Anatase-to-rutile transformation in titania powders. J. Am. Ceram. Soc. 84 (2001) 619-622.

[28] R.L. Penn, J.F. Banfield. Formation of rutile nuclei at anatase {112} twin interfaces and the phase transformation mechanism in nanocrystalline titania. Am. Miner. 84 (1999) 871-876.

[29] Y. Zhou, K.A. Fichthorn. Microscopic view of nucleation in the anatase-to-rutile transformation. J. Phys. Chem. C 116 (2012) 8314-8321.

[30] G.H. Lee, J.M. Zuo. Growth and phase transformation of nanometer-sized titanium oxide powders produced by the precipitation method. J. Am. Ceram. Soc. 87 (2004) 473-479.

[31] D.A.H. Hanaor, C.C. Sorrell. Review of the anatase to rutile phase transformation. J. Mater. Sci. 46 (2011) 855-874.

[32] L. Romero, A.B. Jorge, P.F. McMillan, R. Binions. Enhanced photocatalytic properties of titanium dioxide thin films produced from the ac electric field assisted chemical vapor deposition of titanium (IV) chloride in toluene. ECS J. Solid State Sci. Technol. 3 (2014) N107-N113.

[33] R.A. Fisher, M.R. Watt, R. Konjeti, W.J. Ready. Atomic layer deposition of titanium oxide for pseudocapacitive functionalization of vertically-aligned carbon nanotube supercapacitor electrodes. ECS J. Solid State Sci. Technol. 4 (2015) M1-M5.

[34] H. Yoon, B. Joshi, S.-H. Na, S.S. Yoon. Antibacterial activity and photocatalysis of electrosprayed titania films. J. Electrochem. Soc. 159 (2012) H823-H827.

[35] S. Dhanapandian, A. Arunachalam, C. Manoharan. Effect of deposition parameters on the properties of TiO_2 thin films prepared by spray pyrolysis. J. Sol-Gel Sci. Technol. 77 (2016) 119-135.

[36] P. Reckers, M. Dimamay, J. Klett, S. Trost, K. Zilberberg, T. Riedl, B.A. Parkinson, J. Brötz, W. Jaegermann, T. Mayer. Deep and shallow TiO_2 gap states on cleaved anatase single crystal (101) surfaces, nanocrystalline anatase films, and ALD titania ante and post annealing. J. Phys. Chem. C, 119 (2015) 9890-9898.

[37] V.G. Krishnan, A. Purushothaman, P. Elango. Effect of thickness on the physical properties and gas sensing application: anatase titanium dioxide nanofilms by automated nebulizer spray pyrolysis (ANSP). J. Mater. Sci.: Mater. Electron. 28 (2017) 11473-11481.

[38] M. Reinke, E. Ponomarev, Y. Kuzminykh, P. Hoffmann. Combinatorial characterization of TiO_2 chemical vapor deposition utilizing titanium isopropoxide. ACS Comb. Sci. 17 (2015) 413-420.

[39] Y. Yang, Y. Liang, G. Wang, L. Liu, C. Yuan, T. Yu, Q. Li, F. Zeng, G. Gu. Enhanced gas-sensing properties of the hierarchical TiO_2 hollow microspheres with exposed high-energy {001} crystal facets. ACS Appl. Mater. Interfaces 7 (2015) 24902-24908.

[40] W. Zeng, T. Liu, Z. Wang, S. Tsukimoto, M. Saito, Y. Ikuhara. Oxygen adsorption on anatase TiO_2 (101) and (001) surfaces from first principles. Mater. Trans. 51 (2010) 171-175.

Chapter 2

Fabrication equipment and characterization techniques

2.1 Introduction

The equipments used to fabricate and characterize thin films, nanorods, and core-shell nanostructures were briefly described in this chapter. The aluminum doped ZnO (AZO) films were deposited by radio frequency (RF) magnetron sputtering system. ZnO nanorods were fabricated by chemical bath deposition (CBD). TiO_2 thin films and ZnO-TiO_2 core-shell structures were fabricated by mist chemical vapor deposition (mist CVD). After fabrication, the morphological, structural, and optical properties of samples were evaluated with variety of analysis devices. The morphologies of films and nanostructures were observed with a field emission scanning electron microscope (FE-SEM) system. Surface roughness and surface area were characterized by an atomic force microscope (AFM). The crystallinity was evaluated with an X-ray diffraction (XRD) system. The luminescent property of nanostructures was performed by photoluminescence (PL) measurement. Raman spectroscopy was measured with a confocal Raman microscope. Optical transmittance spectra were characterized by a spectrophotometer. All the measurements were carried out at room temperature. In next two sections, the equipments were interpreted in detail.

2.2 Fabrication equipment

2.2.1 Mist chemical vapor deposition

Mist CVD is a novel method to fabricate metal oxide films and nanoparticles. The schematic diagram of mist CVD is shown in Fig. 2.1 [1]. The conventional mist CVD system mainly consists of two parts. The first part is the mist generator unit, in which the solution is atomized to mist droplets by ultrasonic transducer. The frequency of ultrasonic is 2.4 MHz. The second part is the reaction unit. The mist droplets were transferred to the reaction unit by carrier gas. The dilution gas dilutes the density of the mist droplets. After mist droplets reach the reaction unit, the droplets will burst into much smaller droplets due to the high temperature and high vapor pressure. In this

design of reaction chamber, there is a novel designed big area named as “mist gas mixing section” and a designed narrow channel structure named as ‘‘fine channel’’. When the mist droplets were transferred from the mist gas mixing section to the fine channel, the pressure and kinetic energy of mist droplets decreased because the space of the fine channel was much smaller than that of mist gas mixing section. Due to gravity and absorption, the mist droplets moved effectively onto the substrate that was set on the heating plate. Therefore, the mass transport of precursor was improved. By using this novel designed reaction chamber, precise growth controllability and large area deposition, as well as low cost and simplicity, could be achieved.

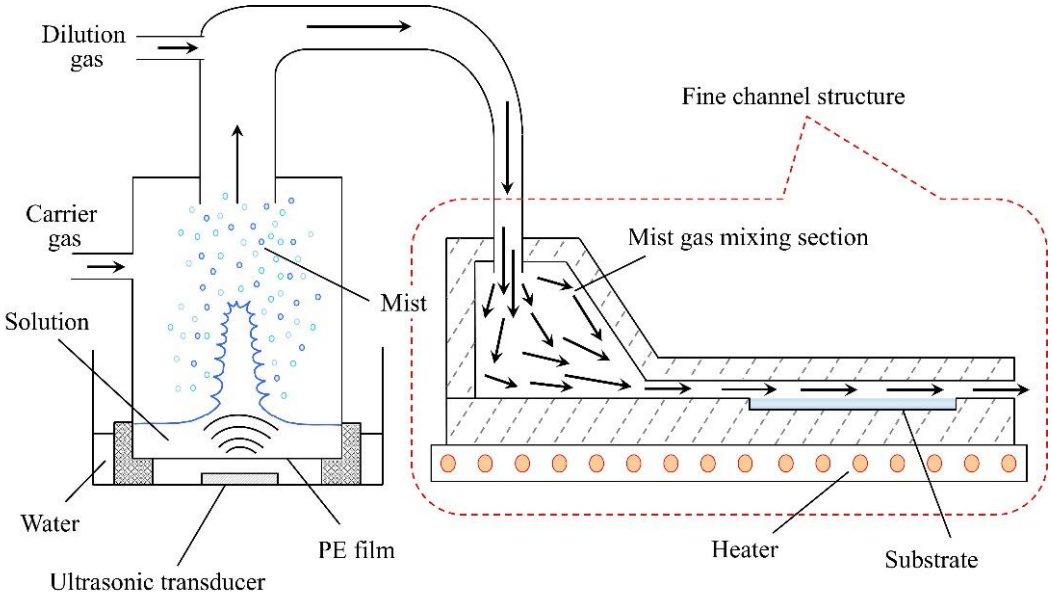

Fig. 2.1 The diagrammatic sketch of mist CVD process [1].

In this research, mist CVD was used to fabricate TiO_2 film and ZnO-TiO_2 core-shell nanorods. The deposition conditions were optimized to control the quality of thin films and nanostructures. The details of experimental conditions were interpreted in chapter 3, chapter 4 and chapter 5.

2.2.2 Chemical bath deposition

CBD method is one of the easiest and cheapest methods to deposit thin films and nanomaterials due to non-expensive equipment and potentiality for large area deposition [2]. The CBD method contains a heating unit and reaction unit, shown in Fig. 2.2. The heating unit is used to heat the water or other solutions at a certain temperature for reaction. The reaction unit is for the

fabrication of thin films or nanomaterials, which is strongly dependent on the chemical reactions. The major advantage of CBD is that it requires only solution containers and substrate mounting devices.

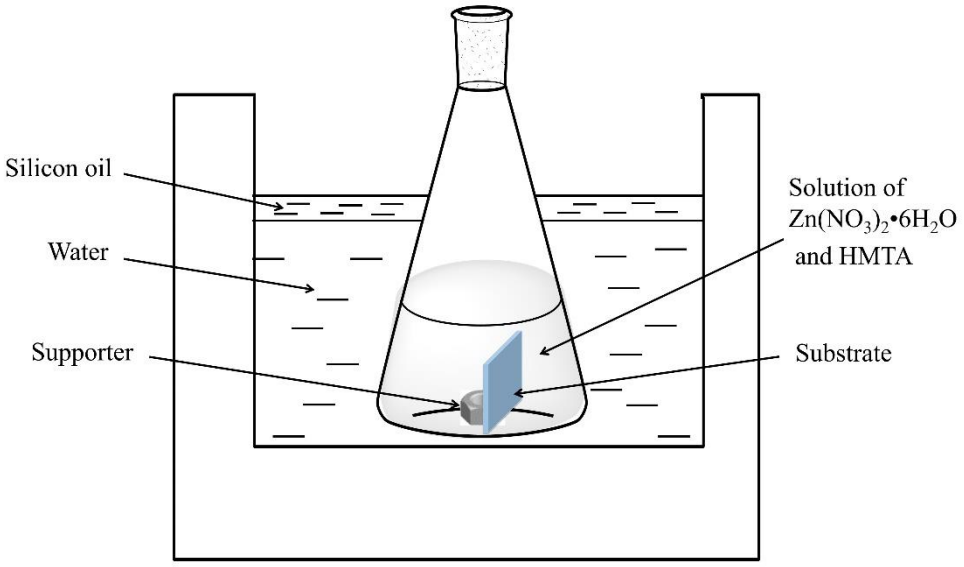

Fig. 2.2 The diagrammatic sketch of CBD apparatus.

In this research, CBD method was used to synthesize ZnO nanorods on ZnO based substrates. The CBD conditions including solution concentrations and growth time were investigated.

2.2.3 Radio frequency magnetron sputtering system

RF magnetron sputtering is a widely applied to the deposition of insulating and semiconducting thin films on different substrates [3].

The processes of sputtering can be interpreted as follows. Firstly, the ionic plasma is produced from inlet gas such as argon by applying a high voltage to the glow tube. Then the ions bombard the target located in cathode and the target atoms are ejected from the cathode by energy and momentum transfer. As a result, the sputtered atoms are deposited on the substrate located on the anode. Due to rapidly changing electric field for RF sputtering, the plasma moves to substrate and target back and forth. The potential difference between cathode and anode can be maintained. Therefore, the insulator and semiconducor can be deposited by RF sputtering.

As for the magnetron effect, the magnetron field is oriented parallel to the cathode surface, resulting in that the plasma forms a closed loop in the local polarity of magnetron field. Due to

the increased confinement of plasma, the plasma density will be much higher. Therefore, more target atoms are ejected. The sputtered atoms are not affected by the magnetron field due to their electrical neutrality.

In this research, AZO films were deposited by a conventional RF (13.56 MHz) magnetron sputtering system, which was shown in Fig. 2.3.

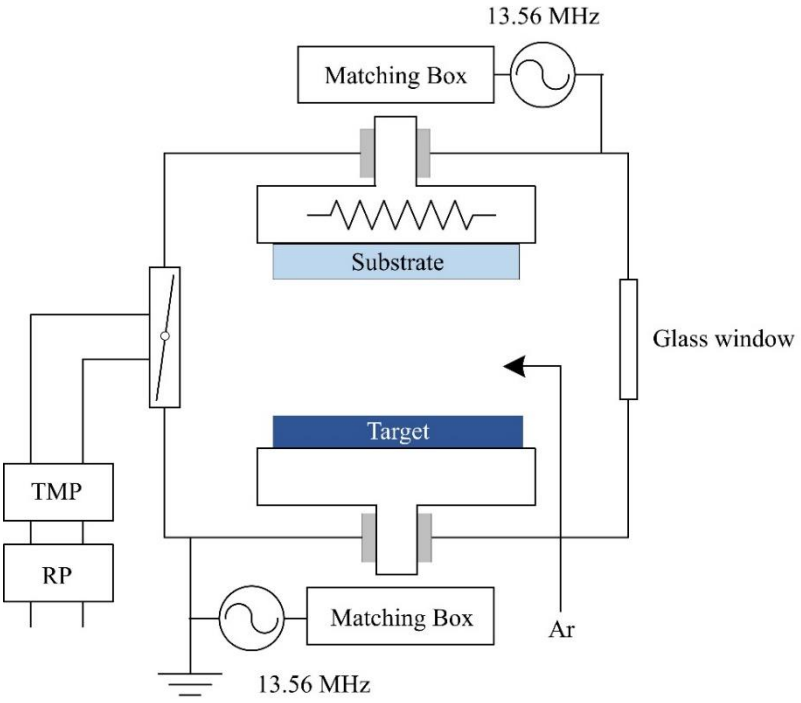

Fig. 2.3 The diagrammatic sketch of RF magnetron sputtering apparatus.

2.3 Characterization techniques

2.3.1 Field emission scanning electron microscope

Morphological property of the samples was obtained by a FE-SEM system. As shown in Fig. 2.4, the FE-SEM system contains electron gun, focus coils, detector system and vacuum system [4]. A focused beam of high-energy electrons is used to generate a variety of signals at the surface of solid specimens. These signals include secondary electrons, backscattered electrons (BSE), diffracted backscattered electrons (DBSE), photons (characteristic X-rays), visible light (cathodoluminescence), and heat. The signals reveal information of the sample including external morphology, chemical composition, crystalline structure, and orientation of materials.

In this research, the morphologies of samples were measured by a FE-SEM equipment (Hitachi SU8020), which is shown in Fig. 2.5.

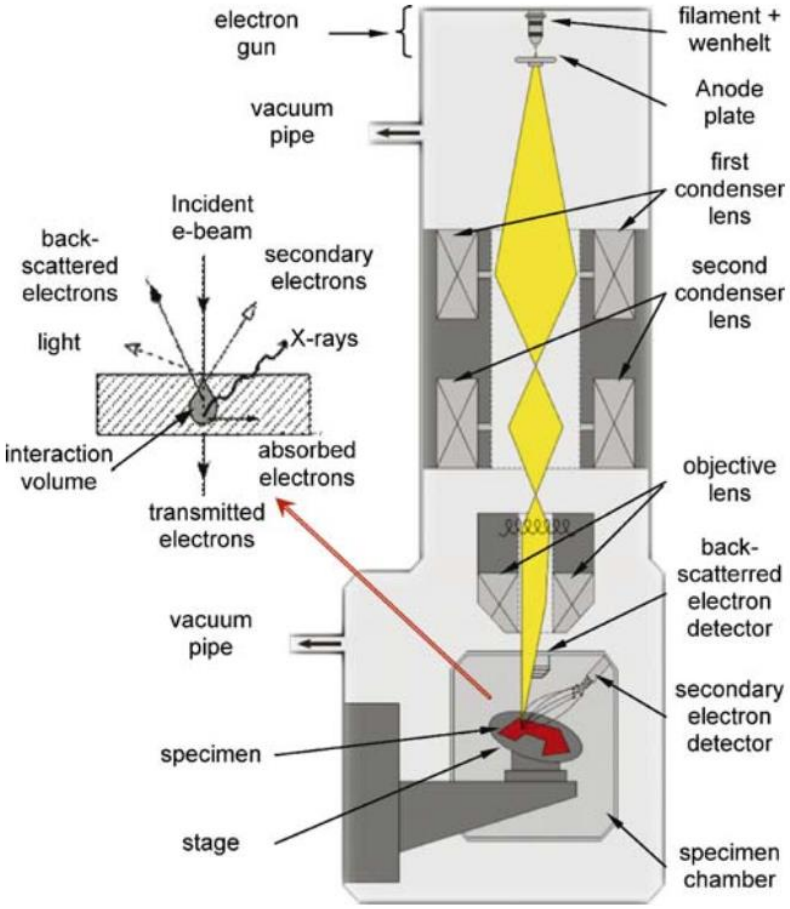

Fig. 2.4 Schematic of a typical scanning electron microscope and imaging process [5].

Fig. 2.5 FE-SEM instrument.

2.3.2 X-ray diffraction

X-ray is one kind of electromagnetic radiation with the wavelength of 0.1 nm, which equals to the diameter of the atom. X-ray diffraction is one of most popular non-destructive techniques for probing the crystalline structure at atomic level.

Crystal, which means regularity and symmetry, is a regular three-dimensional distribution of atoms in space. A series of parallel planes separated with a distance d are well arranged, which are dependent on various structure and packing method for different materials. According to Bragg's law, when a monochromatic X-ray with the wavelength of λ incident to a crystal sample at an angle of θ, X-ray will be diffracted by parallel planes of atoms [5].

$$n\lambda = 2d \sin\theta \tag{2.1}$$

where, n is integer that represents the order of the reflection, λ is the wavelength of X-ray, d is the spacing between diffracting planes, θ is the incident angle. Therefore, the characteristic of the materials can be evaluated in detail.

In this research, Rigaku ATX-G was used to measure the structural properties of films and nanostructures, shown in Fig. 2.6. The structural properties of ZnO nanorods were measured by using 2θ-ω scanning and employing a Cu Kα tube (λ = 0.154178 nm) radiation (50 kV, 300 mA) in the range from 20 ° to 40 °. The structural properties of TiO_2 films and ZnO/TiO_2 core-shell nanorods were measured by grazing incidence x-ray diffraction (GIXRD) model at a 0.35 ° incidence angle in the range from 20 ° to 80 °.

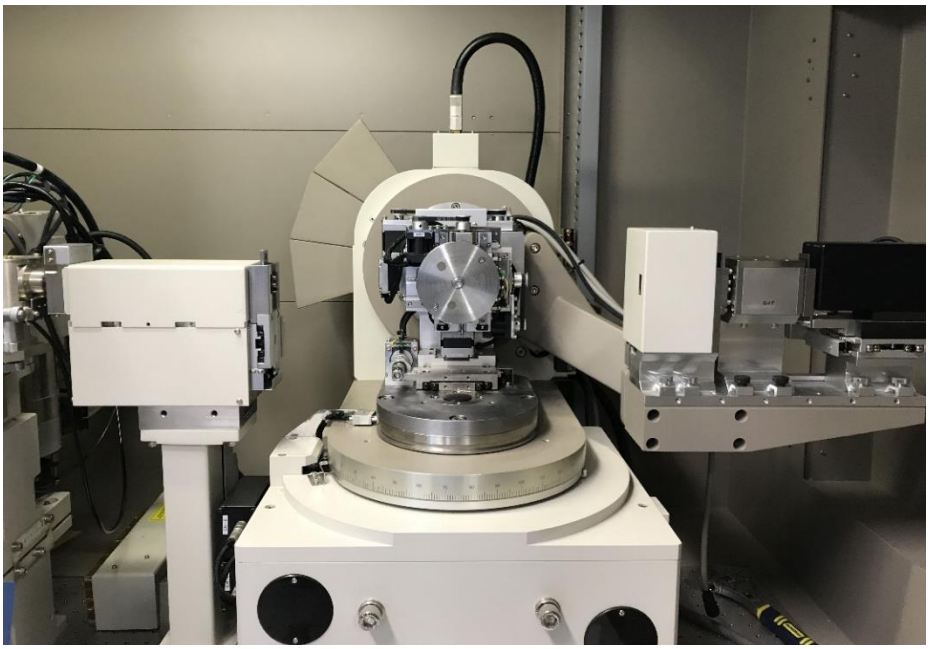

Fig. 2.6 XRD instrument.

2.3.3 Photoluminescence spectroscopy

PL spectroscopy is a contactless, nondestructive method to probe the electrical properties of materials. Photo-excitation occurs when the light incidents on the sample. Photo-excitation causes electrons with the materials to transmit into other possible energy leves. When the electrons return to the equilibrium states, the energy is leased as photons. The photons can be detected by the CCD camera. The photon energy is dependent on the defects level or dopants level of material. Therefore, the photoluminescence provides a good method to study the electrical property of material [6].

In this research, PL measurements were performed with an iHR320 Micro-PL/Raman spectroscope (Horiba Ltd.) using a He-Cd laser with a wavelength of 325.25 nm as an excitation light source. The composition of PL measurement was shown in Fig. 2.7. The instrument of PL spectroscopy was shown in Fig. 2.8.

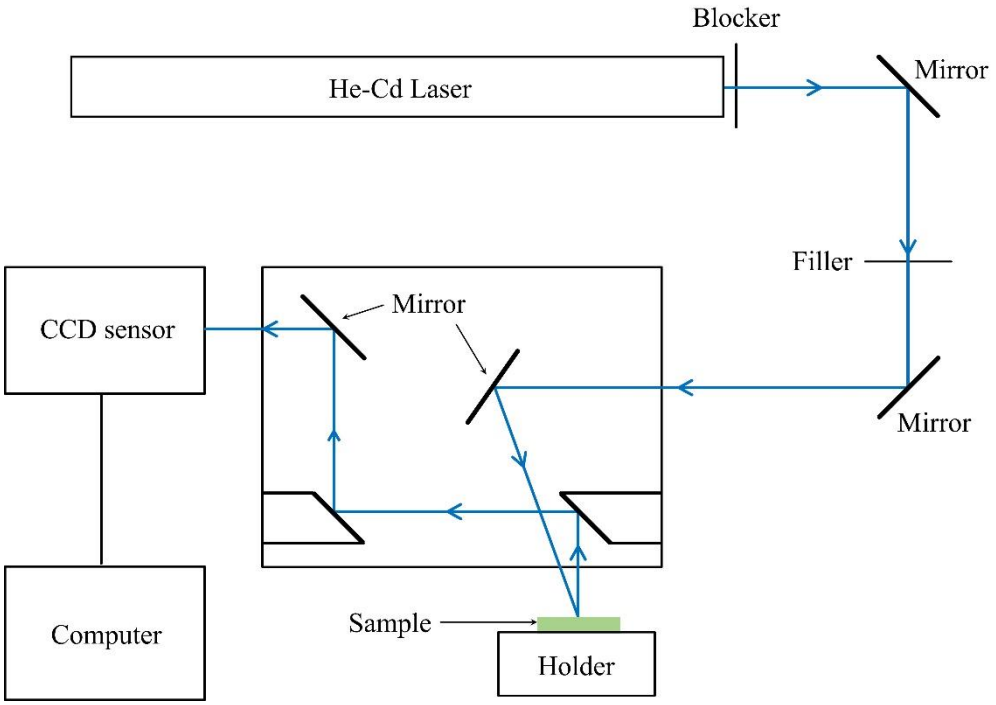

Fig. 2.7 The schematic diagram of PL spectroscopy measurement.

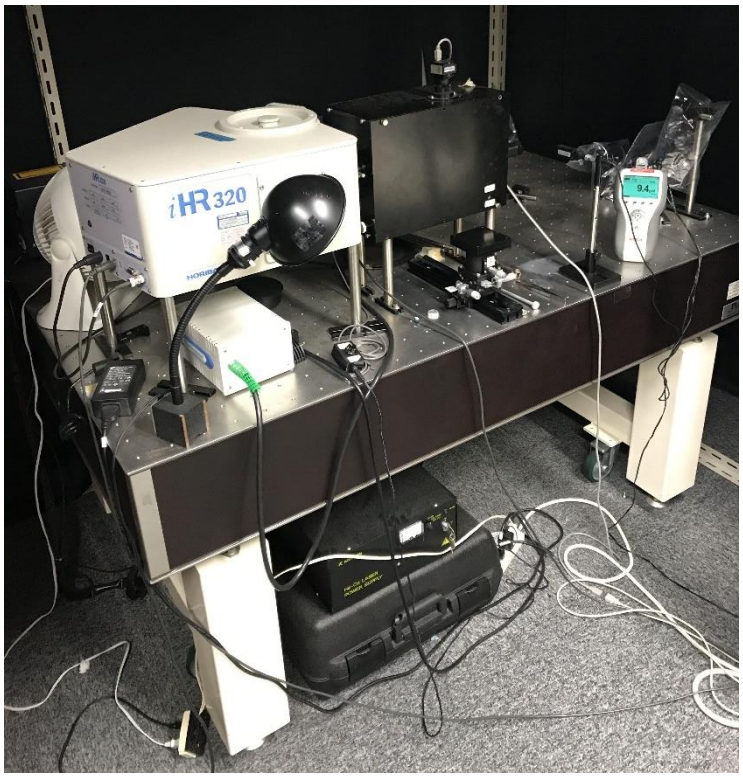

Fig. 2.8 The instrument of PL spectroscopy.

2.3.4 Raman spectroscopy

Raman spectroscopy is a spectroscopic technique to observe vibrational, rotational, and other low-frequency modes in a system. When laser interacts with molecular vibrations, rotations, or phonons in the materials, the energy of the laser photons is shifted left or right. The shift in energy gives information about the vibrational modes in the system. Raman spectroscopy can be used for both qualitative and quantitative applications. The spectra are very specific for different material or different phase of same materials. Chemical identifications can be performed by using search algorithms against digital databases [7].

In this research, a confocal Raman microscope (HORIBA, LabRAM HR800) (shown in Fig. 2.9) with 532.8 nm excitation laser was used to confirm the phase of TiO_2 films.

Fig. 2.9 Raman spectroscopy instrument.

2.3.5 Spectrophotometer

Spectrophotometer is one of most basic techniques for analyzing the optical properties of samples in the light range from near UV light to infrared. It is a non-destructive system to measure the optical properties. Light passes through a sample to be registered by a detector and compared to original light. Using this transmission spectroscopy, we can obtain the information of the sample including the absorption coefficient of the sample, the reflectance and refractive

index, the dielectric constant, and coarse calculation of bandgap [8].

In this research, optical transmission spectra measurements of samples were performed using an ultraviolet-visible-infrared (UV-Vis-IR) spectrophotometer (U-4100, Hitachi Corp), shown in Fig. 2.10. The measurement region ranges from 176 nm to 2500 nm. The transmittance spectra of TiO_2 films, ZnO nanorods, and core-shell structures were evaluated by this equipment.

Fig. 2.10 U-4100 UV-Vis-IR spectrophotometer.

2.3.6 Atomic force microscopy

AFM is one of the most powerful microscopy technology to study the surface morphology. It is non-destructive and can provide structural, mechanical and functional information under physiological conditions [9]. The schematic diagram of AFM was shown in Fig. 2.11 [10]. The main unit for AFM is the sharp cantilever tip. When the tip approaches to the sample surface, the local force between tip and surface will be detected. Via scanning the sample surface, the microscopic features of the samples will be detected. Because the images are acquired by the atomic force, the images with good resolution are possible. Therefore, the AFM is a useful instrument for analyzing surface roughness.

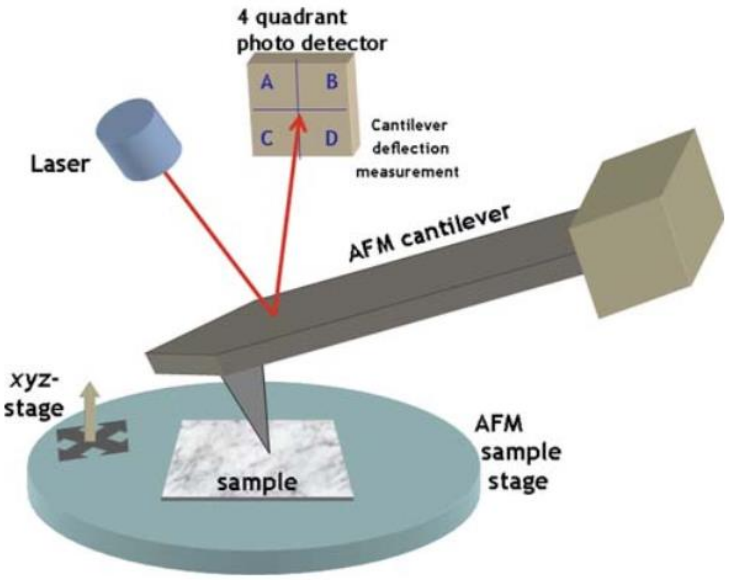

Fig. 2.11 The schematic diagram of AFM measurement [10].

In this research, the AFM (Nano-R2, Pacific Nanotechnology) was used to measure the surface root mean squre roughness of ZnO based films, which is shown in Fig. 2.12.

Fig. 2.12 AFM instrument.

2.3.7 Gas sensitivity measurement system

In this research, the gas sensitivity measurement was performed with a homemade measurement system at Old Dominion University. The instrument of gas sensitivity measurement system was shown in Fig. 2.13. The measurements were carried out with ethanol vapor at different temperatures. The resistivities of samples in the ethanol atmosphere were recorded to evaluate the gas sensitivity.

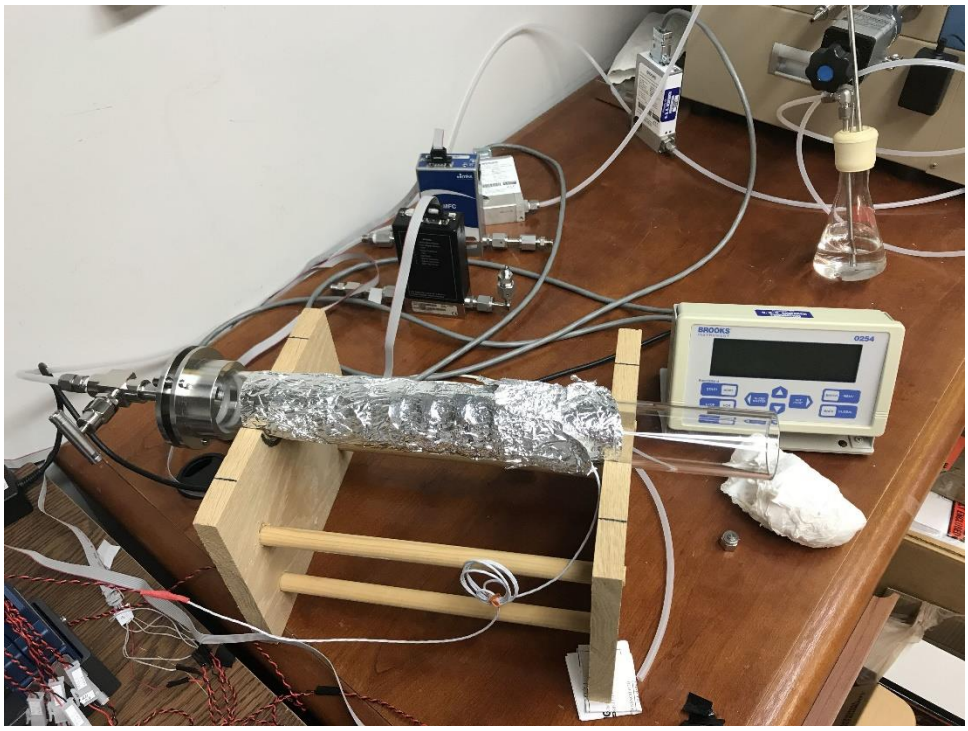

Fig. 2.13 Gas sensitivity evaluation system.

2.4 References

[1] T. Kawaharamura, S. Fujita. An approach for single crystalline zinc oxide thin films with fine channel mist chemical vapor deposition method. Phys. Status Solidi c 5 (2008) 3138-3140.

[2] B. Cao, W. Cai. From ZnO nanorods to nanoplates: chemical bath deposition growth and surface-related emissions. J. Phys. Chem. C 112 (2008) 680-685.

[3] J.L. Vossen, W. Kern. Thin film processes II. Academic press, San diego, (2012) 177-200.

[4] M.A. Sutton, N. Li, D.C. Joy, A.P. Reynolds,X. Li. Scanning electron microscopy for quantitative small and large deformation measurements Part I: SEM imaging at magnifications from 200 to 10,000. Experimental Mechanics 47 (2007) 775-787.

[5] J.M. Jensen, A.B. Oelkers, R. Toivola, D.C. Johnson, J.W. Elam, S.M George. X-ray reflectivity characterization of ZnO/Al_2O_3 multilayers prepared by atomic layer deposition. *Chem. Mater.* 14 (2002) 2276-2282.

[6] G.D. Gilliland. Photoluminescence spectroscopy of crystalline semiconductors. Mater. Sci. Eng. R-Rep. 18 (1997) 99-399.

[7] S. Ahmed, C.M. Hussain. Green and Sustainable Advanced Materials: Processing and Characterization, Volume 1. John Wiley & Sons: Beverly, MA, USA, 2018.

[8] S. Hong, T. Joo, W.I. Park, Y.H. Jun, G.-C. Yi. Time-resolved photoluminescence of the size-controlled ZnO nanorods. Appl. Phys. Lett. 83 (2003) 4157-4159.

[9] G. Binnig, C.F. Quate, C. Gerber. Atomic force microscope. Phys. Rev. Lett. 56 (1986) 930-933.

[10] S. Kim, K.D. Kihm, T. Thundat. Fluidic applications for atomic force microscopy (AFM) with microcantilever sensors. Exp. Fluids 48 (2010) 721-736.

Chapter 3

Fabrication and characterization of anatase phase TiO_2 thin films with ethanol as solvent by mist CVD method

3.1 Introduction

Hitherto, anatase phase TiO_2 thin films have been synthesized by various techniques, including magnetron sputtering, high-vacuum chemical vapor deposition (HV-CVD), atomic layer deposition (ALD), electron beam evaporation, and sol-gel method [1-15]. However, the obtained TiO_2 thin films obtained by these methods are mostly a mixture of anatase and rutile phase TiO_2 [10-15]. Although there are some reports on fabricating pure anatase phase TiO_2 films, their thermal stability is poor [3,13,17] due to the presence of (112) surface in anatase phase TiO_2 [16-20], which limits the application of anatase phase TiO_2 films as sensing material.

Moreover, it is still strict issue to obtain pure anatase phase TiO_2 with good uniformity and high crystallinity using current synthesis methods [9-11,21-28]. Particularly, it is difficult to fabricate anatase phase TiO_2 thin films with good crystallinity by spray pyrolysis, conventional chemical vapor deposition, ALD or HV-CVD. When these methods are applied with a low deposition temperature (not higher than 350 ˚C), the deposition of anatase phased TiO_2 film is kinetically controlled [1], which means the growth of anatase phased TiO_2 film is limited by low decomposition rate of precursor. As a result, the crystallinity of obtained TiO_2 film is poor [10,25,26]. When deposition temperature is increased, the deposition will become controlled by mass transport [1], and the growth of anatase phased TiO_2 film is limited by the lack of precursor, resulting in a poor thickness uniformity of deposited TiO_2 film [10,27,28].

In order to fabricate pure anatase phase TiO_2 film with good uniformity, high crystallinity and high thermal stability, it is necessary to develop a novel synthesis method. In our previous research, we used a novel mist CVD to synthesize zinc oxide films [29]. Compared with other reported methods, even several publications using similar mist droplets source supply stage [30,31], this novel mist CVD had advantages in terms of precise growth controllability and large area deposition, as well as low cost and simplicity [29,32]. Therefore, mist CVD is expected to

an alternative method to synthesize pure anatase phase TiO_2 thin films.

In this chapter, the mist CVD method was used to synthesize pure anatase phase TiO_2 thin films. The deposition temperature, solution concentration, film thickness and substrate are significant parameters for mist CVD method, which can greatly influence the properties of TiO_2 film. Therefore, the effects of deposition temperature, TTIP concentration in the solution, film thickness and substrate on the structural properties of TiO_2 thin films were investigated.

3.2 Effects of deposition temperature on the properties of TiO_2 thin films

3.2.1 Experimental

The deposition condition is shown in Table 3.1. TTIP (Wako Pure Chemical Industries, Ltd., Osaka, Japan) was dissolved in ethanol (Wako Pure Chemical Industries, Ltd., Osaka, Japan) to prepare a solution of precursor. Compressed air was used as both a carrier and a dilution gas. The flow rates of the carrier gas and dilution gas were set at 2.5 L/min and 4.5 L/min respectively. Quartz glass was selected as a substrate and set in the reaction chamber. To investigate the influence of deposition temperature, the temperature was set at a range from 200 °C to 400 °C with an interval of 50 °C.

Table 3.1 Deposition condition of temperature dependence.

Solute	TTIP
Solvent	Ethanol
Concentration (mol/L)	0.10
Substrate	Quartz glass
Deposition temperature (°C)	200, 250, 300, 350, 400
Carrier gas, flow rate (L/min)	Compressed air, 2.5
Dilution gas, flow rate (L/min)	Compressed air, 4.5

3.2.2 Results and discussion

Figure 3.1 shows the GIXRD patterns of TiO_2 films deposited under different temperatures. There were no obvious peaks observed in the GIXRD patterns of TiO_2 films deposited at temperatures from 200 °C to 250 °C. The diffraction peaks were identified clearly as the

deposition temperature increased from 300 °C to 400 °C, which corresponded with the reflections from (101), (103), (004), (112), (200), (105), (211), (201), (204), and (215) crystal planes of the anatase phase TiO_2, respectively. It was clear that the (101) peaks were the predominant peaks, indicating that the (101)-oriented anatase facets were dominant for the as-deposed TiO_2 films during deposition at temperatures from 300 °C to 400 °C. The crystallinity of anatase TiO_2 film was significantly improved with the increase in temperature. The highest (101) peak intensity was obtained at 400 °C, which suggested that the TiO_2 films with the best crystallinity were obtained at this temperature.

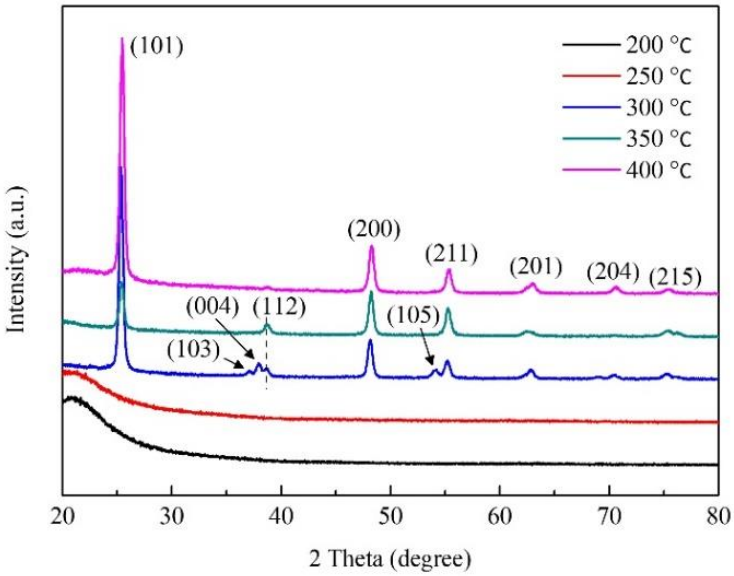

Fig. 3.1 XRD patterns of TiO_2 films deposited under different temperatures using the mist CVD method.

To confirm the uniformity, the TiO_2 films deposited under different temperatures were imaged by AFM, as shown in Fig. 3.2. It was clearly observed that the TiO_2 films fabricated at different temperatures were uniform and flat. The root mean square (RMS) values of the film surface roughness are summarized in Table 3.2. The roughnesses of all TiO_2 films were less than 7 nm and showed a tendency to increase as the deposition temperature increased from 200 °C to 400 °C.

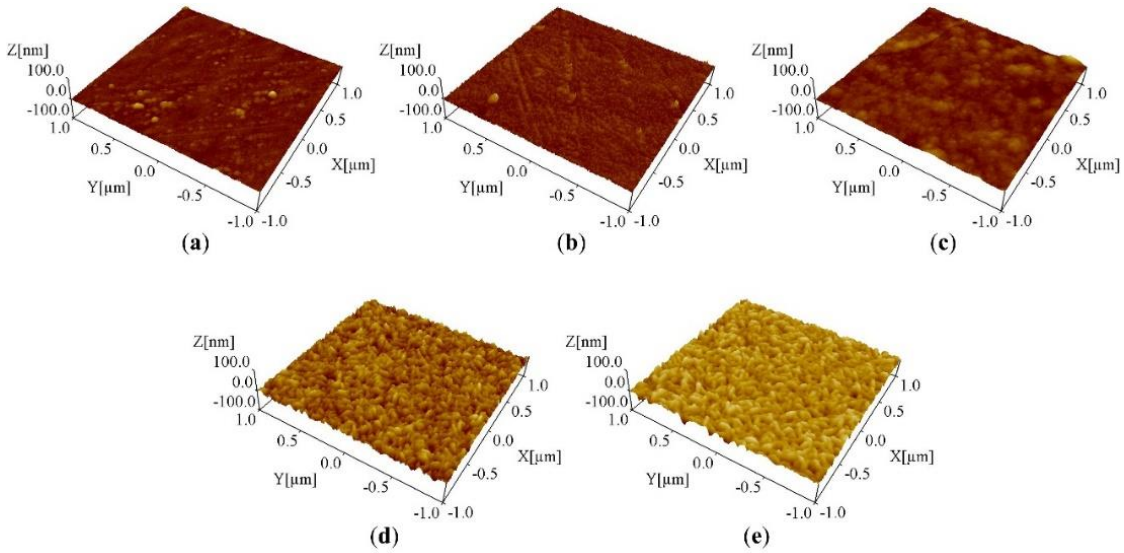

Fig. 3.2 AFM images of TiO_2 films deposited under different temperatures using the mist CVD method. ((**a**) 200 °C; (**b**) 250 °C; (**c**) 300 °C; (**d**) 350 °C; (**e**) 400 °C).

Table 3.2 Surface roughness of TiO_2 films deposited under different temperatures.

Deposition temperature (°C)	Surface roughness (nm)
200	1.45
250	3.26
300	2.86
350	6.56
400	6.18

During the deposition process, the chemical reactions significantly depended on the temperature. It was reported that the thermal decomposition mechanism of TTIP could be separated as two reactions, including both pyrolysis (Equation (3.1)) and hydrolysis (Equation (3.2)) [33].

$$Ti(OC_3H_7)_4 \rightarrow TiO_2 + 4C_3H_6 + 2H_2O \quad (3.1)$$

$$Ti(OC_3H_7)_4 + 2H_2O \rightarrow TiO_2 + 4C_3H_7OH \quad (3.2)$$

The required temperature of pyrolysis was higher than 250 °C. The required temperature of hydrolysis was higher than 175 °C in the presence of H_2O [34].

During the mist CVD process, the pyrolysis of TTIP would not occur when the deposition temperature was lower than 250 °C. Because there was no additional H_2O participating, the hydrolysis of TTIP (Equation (3.2)) could not occur at 200 °C (although this reaction temperature was higher than 175 °C). This is the reason no peaks were observed in GIXRD patterns for the TiO_2 film deposited at 200 °C and 250 °C.

The thermal decomposition mechanism of TTIP in ALD and HV-CVD was analyzed and reported by some groups [28,33-37]. Reinke et al. [36] investigated the surface reaction kinetics of TTIP in HV-CVD and proposed a comprehensive surface kinetic model. Based on the surface kinetic parameters from their model, the reaction rate constant (k) under different temperatures can be calculated using the Arrhenius equation (Equation (3.3)).

$$k = A\exp(-E_a/RT) \tag{3.3}$$

where A is the frequency factor, E_a the activation energy of reaction, R the universal gas constant and T the reaction temperature (in kelvin).

As shown in Fig. 3.3, the reaction rate constants of hydrolysis (k_h) and pyrolysis (k_p) in the mist CVD processes were calculated using the Arrhenius equation. During the calculation, the activation energies of hydrolysis and pyrolysis were set as 86 kJ/mol and 185 kJ/mol [36]. It was found that both k_h and k_p increased with an increase in temperature. When the deposition temperature was 250 °C, k_p was lower than k_h, because the frequency factor of pyrolysis was much lower than that of hydrolysis. Because the activation energy of pyrolysis was higher than that of hydrolysis, k_p showed a faster growth speed than that of k_h. When the temperature was lower than 274.56 °C, k_h was higher than k_p. When the temperature was greater than 274.56 °C, k_p was higher than k_h, which suggested that the TiO_2 films deposited from 300 °C to 400 °C could be obtained by the pyrolysis of TTIP.

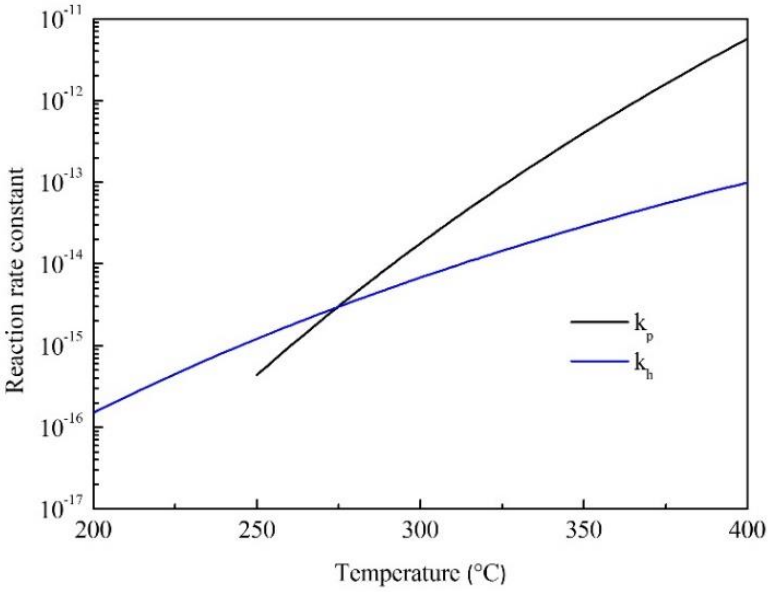

Fig. 3.3 Reaction rate constant of TTIP pyrolysis and hydrolysis reactions under different temperatures.

Based on the above calculation and relevant research [32], we propose a model (as shown in Fig. 3.4) to describe the mechanism of TiO_2 films deposition using the mist CVD process. In the mist droplets source supply stage, the mist droplets—including both TTIP and ethanol—were transformed from the solution of precursors by ultrasonic transducers. Following that, the mist droplets were transported into mist gas mixing section by carrier and dilution gases. During the transportation of mist droplets in the reaction chamber, the size of mist droplets decreased from a few micrometers to a few nanometers under the influence of heat, evapotranspiration and burst. The mist droplets could maintain the nanoscale in the area of fine channel. Due to gravity and absorption, the mist droplets moved effectively onto the substrate, which was set on the heating plate. In this experiment, when the deposition temperature was set from 300 °C to 400 °C, TTIP was decomposed due to the pyrolysis reaction resulting in the generation of anatase phase TiO_2 films.

To investigate the effect of TTIP concentration in solution of precursor on the structural properties of the TiO_2 thin films, the optimized temperature of 400 °C was selected for further investigation on TTIP concentration dependence.

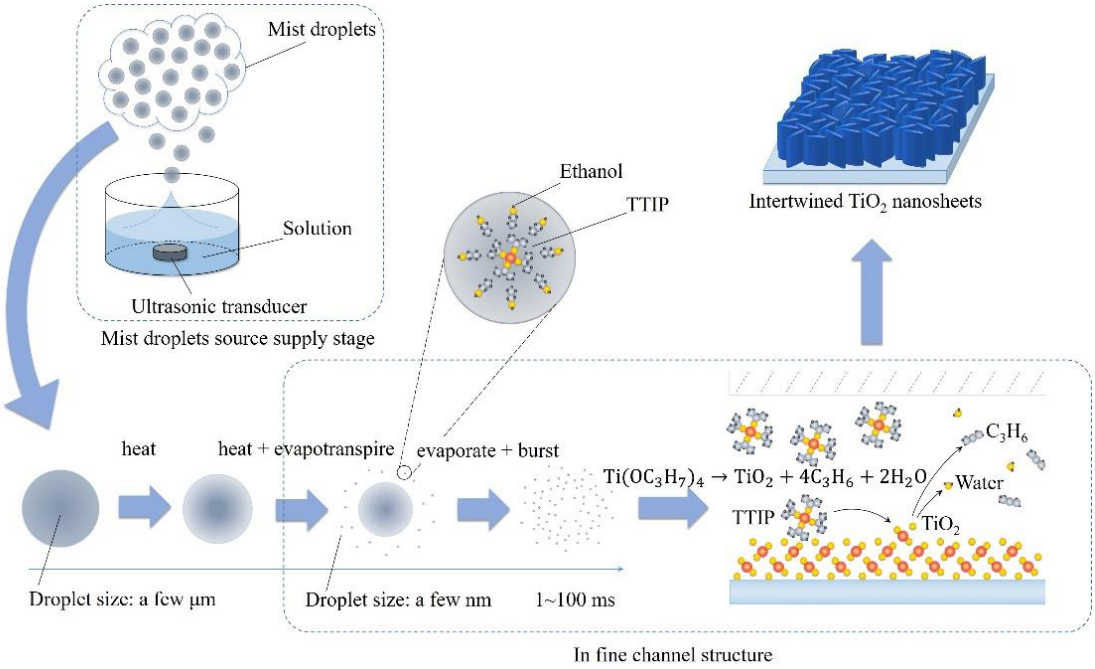

Fig. 3.4 Mechanism of TiO_2 films deposition during the mist CVD process.

3.2.3 Summary

Pure anatase phase TiO_2 films have been fabricated using the mist CVD method. The effects of deposition temperature on the structural properties of TiO_2 films were investigated. The crystallinities of TiO_2 films were significantly improved by increasing deposition temperature. Pure anatase phase TiO_2 films with good uniformity were obtained from 300 °C to 400 °C. The roughnesses of all TiO_2 films were less than 7 nm and showed a variation tendency of increase as the deposition temperature increased from 200 °C to 400 °C.

3.3 Effects of TTIP concentration on the properties of TiO_2 thin films

3.3.1 Experimental

Based on the results of temperature dependence, an optimized temperature of 400 °C was chosen as the deposition temperature for further solution dependence experiments. To investigate the effect of TTIP concentration on structural properties of TiO_2 films, the TTIP concentration was adjusted from 0.05 mol/L to 0.40 mol/L for comparison, as shown in Table 3.3. The other deposition parameters including carrier gas, dilution gas and their flow rates were the same as section 3.2. Before the deposition, the deposition rates at different TTIP

concentrations were measured and confirmed. The deposition times at different TTIP concentrations were adjusted to keep the thickness of all TiO_2 films at 300 nm.

Table 3.3 Deposition condition of TTIP concentration dependence.

Solute	TTIP
Solvent	Ethanol
Concentration (mol/L)	0.05, 0.10, 0.20, 0.30, 0.40
Substrate	Quartz glass
Deposition temperature (°C)	400
Carrier gas, flow rate (L/min)	Compressed air, 2.5
Dilution gas, flow rate (L/min)	Compressed air, 4.5

3.3.2 Results and discussion

The SEM images of TiO_2 films deposited at different TTIP concentrations are shown in Fig. 3.5. In the top view images, intertwined TiO_2 nanosheets with good uniformity were observed. It was found that the aspect ratio of TiO_2 nanosheets changed with an increase in TTIP concentration. When the TTIP concentration increased from 0.05 mol/L to 0.40 mol/L, the length of TiO_2 nanosheets first increased and then decreased, while the variation tendency of width was contrary to that of length. The highest aspect ratio of TiO_2 nanosheets was obtained with a TTIP concentration of 0.20 mol/L. It was observed that TiO_2 nanosheets were vertical to substrate from SEM cross section view images.

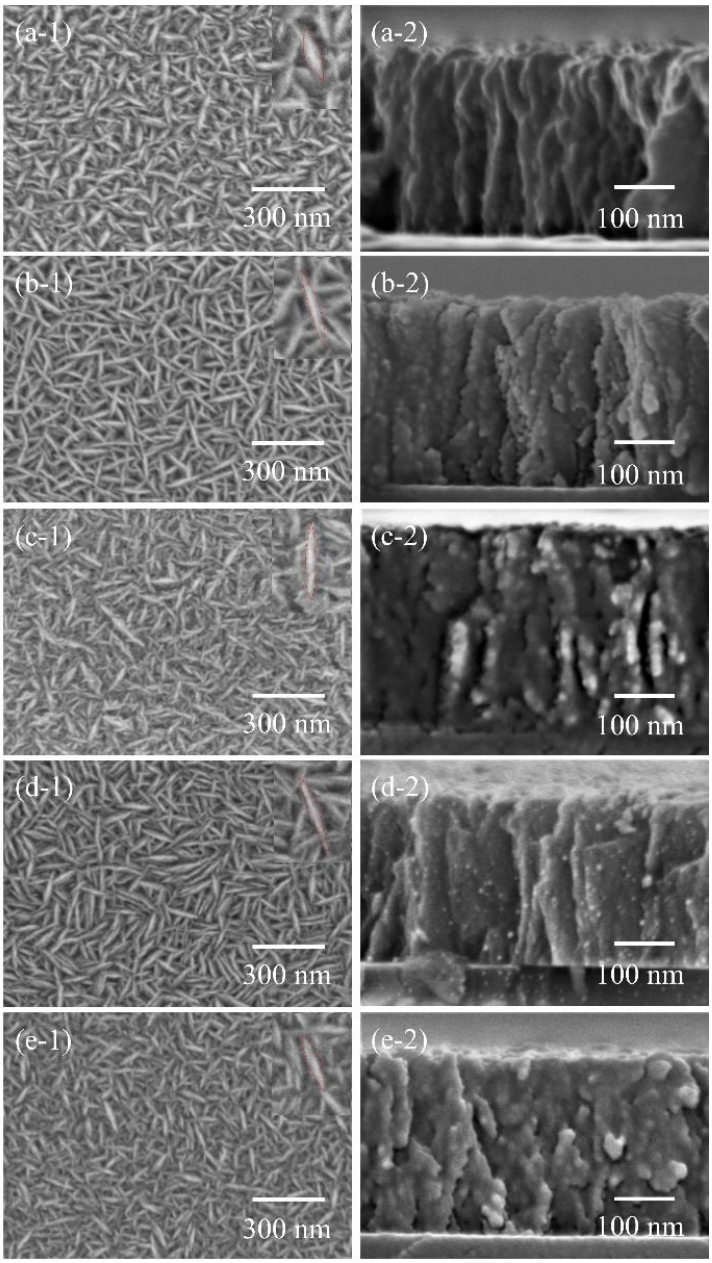

Fig. 3.5 SEM images of TiO_2 films deposited with different TTIP concentrations by mist CVD. ((**a**) 0.05 mol/L; (**b**) 0.10 mol/L; (**c**) 0.20 mol/L; (**d**) 0.30 mol/L; (**e**) 0.40 mol/L; (**1**) top view; (**2**) cross section view).

Figure 3.6 shows the deposition rate and aspect ratio of TiO_2 nanosheets. The aspect ratio changed with changing deposition rate. Due to an increase of TTIP content in conjunction with a relative decrease of ethanol content in the mist, the deposition rate of film increased as the solution concentration rose from 0.05 mol/L to 0.20 mol/L. As the solution concentration increased from 0.20 mol/L to 0.40 mol/L, the deposition rate of film decreased because of the reduction in the total number of mist droplets.

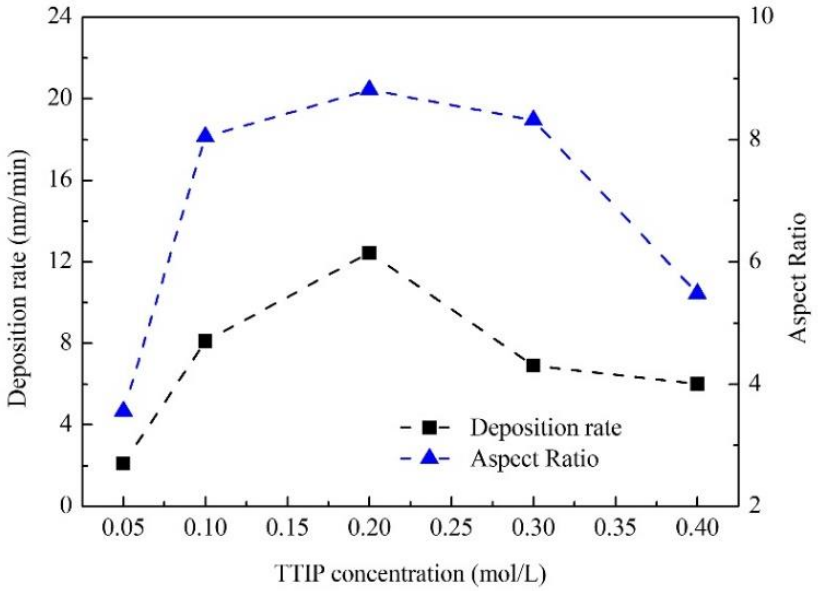

Fig. 3.6 Deposition rate and aspect ratio of TiO_2 nanosheets.

The AFM images of TiO_2 films deposited with different TTIP concentrations by mist CVD were shown in Fig. 3.7. It was clearly observed that the TiO_2 films fabricated with different TTIP concentrations were uniform and flat. The RMS values of the film surface roughness are summarized in Table 3.4. The roughnesses of all TiO_2 films were less than 10 nm regardless of TTIP concentration variation. The lowest surface roughness of TiO_2 film was obtained with a TTIP concentration of 0.40 mol/L, and the highest surface roughness of TiO_2 film was obtained with a TTIP concentration of 0.30 mol/L.

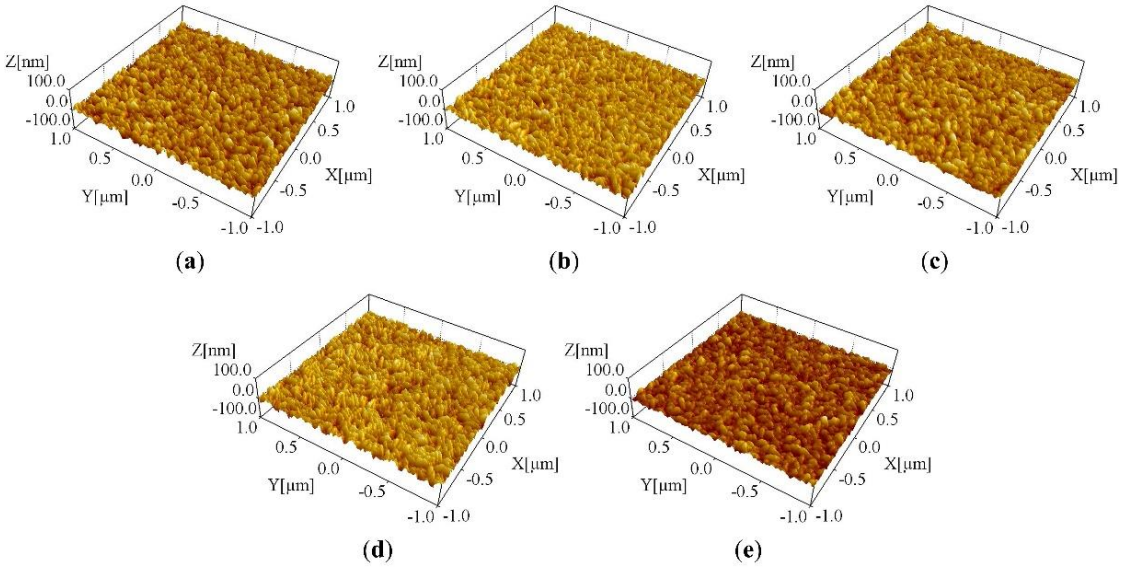

Fig. 3.7 AFM images of TiO_2 films deposited with different TTIP concentrations by mist CVD. ((**a**) 0.05 mol/L; (**b**) 0.10 mol/L; (**c**) 0.20 mol/L; (**d**) 0.30 mol/L; (**e**) 0.40 mol/L).

Table 3.4 Surface roughness of TiO_2 films deposited with different TTIP concentrations.

TTIP concentration (mol/L)	Surface roughness (nm)
0.05	8.93
0.10	8.37
0.20	6.19
0.30	9.41
0.40	6.13

Figure 3.8a shows the GIXRD patterns of TiO_2 films deposited with TTIP concentration from 0.05 mol/L to 0.40 mol/L. All of the peaks corresponded with the reflections from (101), (200), (211), (201), (204), and (215) crystal planes of the anatase phase TiO_2, which suggested that pure anatase phase TiO_2 thin films were obtained, regardless of TTIP concentration variation. Obviously, the diffraction peak, (101) peak located at 2 theta of 25.46°, was dominant with much higher intensity compared with other diffraction peaks for all of the five samples.

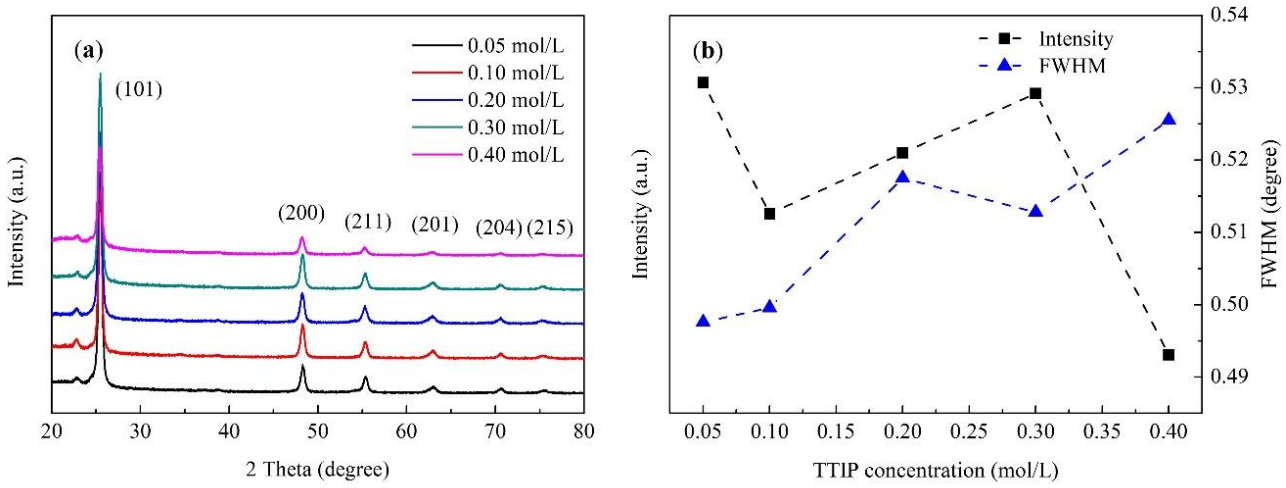

Fig. 3.8 GIXRD results of TiO_2 films deposited with different TTIP concentrations by mist CVD. ((**a**) GIXRD patterns of TiO_2 films; (**b**) (101) peak intensity and FWHM of TiO_2 films).

The dependence of the concentration and the (101) peak intensity and full width at half maximum (FWHM) of TiO_2 films are shown in Fig. 3.8b. It was found that the highest intensity and narrowest FWHM of (101) peak was obtained at a TTIP concentration of 0.05 mol/L resulting in the best crystallinity of TiO_2 film. This might be due to the influence of ethanol. When the TTIP concentration was 0.05 mol/L, ethanol has a strong influence on the growth of TiO_2 film due to the lower ratio of TTIP/ethanol. It has been reported that the average surface

free energy of the anatase (101) surface is lower than that of other anatase surfaces [38]. Therefore, more ethanol molecules were absorbed on the other anatase surface than the (101) surface during the deposition, suppressing the growth of TiO_2 in these directions. Consequently, the preferred growth of TiO_2 in the (101) direction was greatly enhanced. As a result, the best crystallinity was obtained under a TTIP concentration of 0.05 mol/L

However, the variation tendency of the peak intensity was different to that of TTIP concentration, which might be due to the influence of TTIP/ethanol ratio during the deposition process of TiO_2. Compared with ethanol, pure TTIP was much more difficult to atomize ultrasonically because of its high viscosity [39]. The atomization of ethanol was lessened by the increase in the TTIP/ethanol ratio in a certain amount of the solution. As a result, the number of ethanol molecules, which were atomized and transported to the reaction chamber, decreased.

The surface chemical states and electronic structures of the TiO_2 films deposited with different TTIP concentrations were analyzed by XPS. As shown in Fig. 3.9a, the peak in each O 1s spectrum was asymmetric, suggesting the existence of at least two chemical states. After curve fitting, the asymmetric peak (solid line) in each O 1s spectrum was divided into two symmetric peaks (dash line). The peak located from 531.0 eV to 532.2 eV corresponded with Ti-OH bond, and the peak located from 529.3 eV to 530.4 eV corresponded with Ti-O bond. It is reported that the peak shift is attributed to oxygen vacancies [40,41].

As shown in Fig. 3.9b, two symmetric peaks were observed in the Ti 2p XPS spectra. The peak located from 464.0 eV to 464.8 eV corresponded with the Ti $2p_{1/2}$ and Ti $2p_{3/2}$ peaks of Ti^{4+}, and the peak ranged from 458.3 eV to 459.0 eV corresponded with the Ti $2p_{3/2}$ peaks of Ti^{4+}.

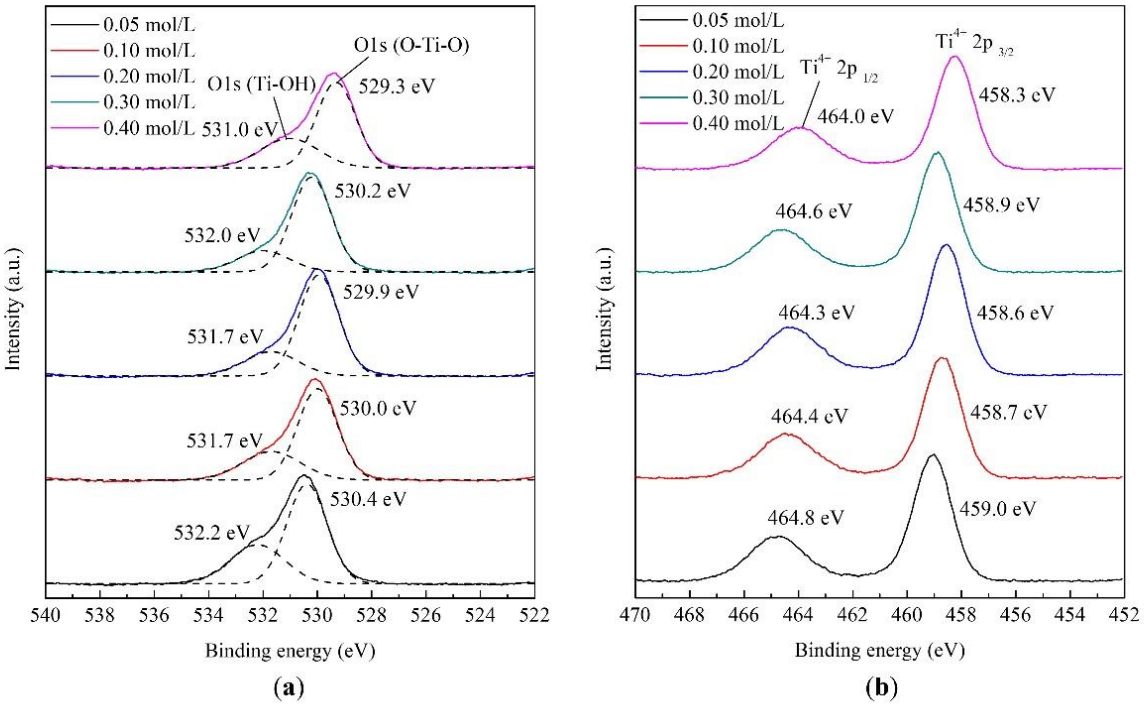

Fig. 3.9 High-resolution XPS spectra of TiO_2 films deposited with different TTIP concentrations by mist CVD. ((**a**) O 1s; (**b**) Ti 2p).

The Raman spectra of TiO_2 films deposited with different TTIP concentrations by mist CVD are shown in Fig. 3.10. Three peaks were observed in the spectra. The peaks at 398 cm^{-1} and 638 cm^{-1} corresponded with the B_{1g} mode and E_g mode of anatase phase TiO_2 respectively. The peak at 514 cm^{-1} was a doublet of the A_{1g} and B_{1g} modes of the anatase phase TiO_2. All of the peaks corresponded with the anatase phase TiO_2, which indicated all of the deposited TiO_2 films were pure anatase phase. This result was in agreement with that of the GIXRD measurement.

The transmission spectra of TiO_2 films deposited with different TTIP concentrations by mist CVD is shown in Fig. 3.11. The transmittance of TiO_2 films deposited with different TTIP concentrations was higher than 75% in the visible region. It was confirmed that the TTIP concentration had little influence on the transmittance of TiO_2 films in the visible region.

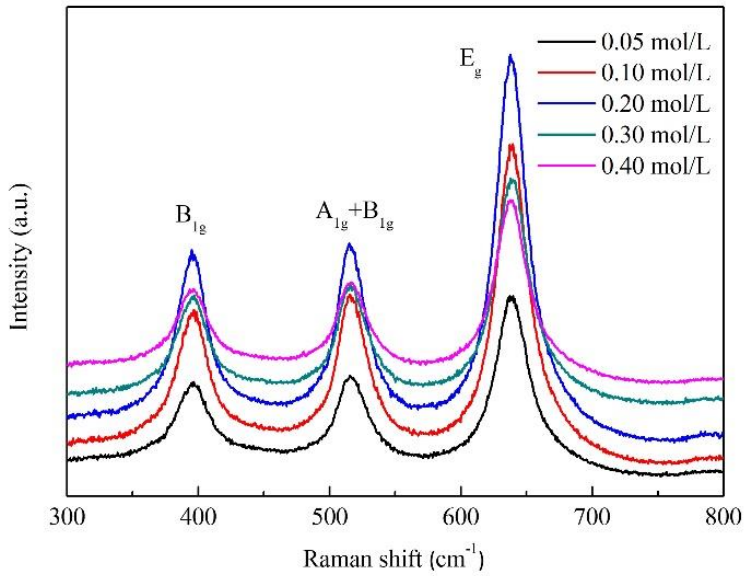

Fig. 3.10 Raman spectra of TiO_2 films deposited with different TTIP concentrations by mist CVD.

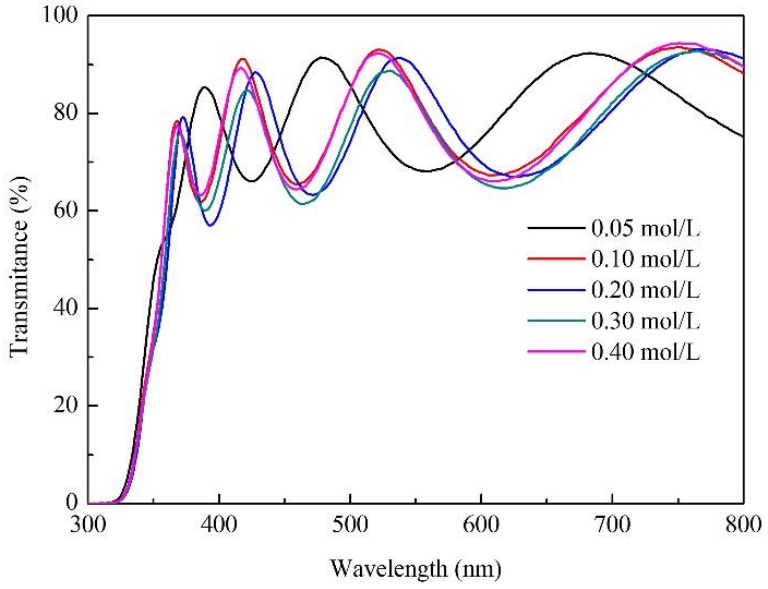

Fig. 3.11 Transmittance of TiO_2 films deposited with different TTIP concentrations by mist CVD.

3.3.3 Summary

Pure anatase phase TiO_2 films were fabricated under different TTIP concentrations by mist CVD method. The effects of TTIP concentration on the structural properties of TiO_2 films were investigated. When the TTIP concentration increased from 0.05 mol/L to 0.40 mol/L, the aspect ratio of TiO_2 nanosheets first increased then decreased. The highest aspect ratio of TiO_2 nanosheets was obtained at a TTIP concentration of 0.20 mol/L. The deposition rate of TiO_2

films had the same variation tendency with aspect ratio. The roughnesses of all TiO_2 films were less than 10 nm regardless of TTIP concentration variation. The crystallinity of TiO_2 films showed a variation tendency of increase as the TTIP concentration increased from 0.05 mol/L to 0.40 mol/L. The best crystallinity was obtained under the TTIP concentration of 0.05 mol/L.

3.4 Effects of film thickness on the properties of TiO_2 thin films

3.4.1 Experimental

The deposition conditions were summarized in Table 3.5. Firstly, a solution of precursors was prepared by dissolving TTIP in ethanol. Secondly, the solution was transformed into mist droplets by ultrasonic atomization. Thirdly, the mist droplets were transferred to the reaction chamber by carrier and dilution gases. Finally, TiO_2 thin film was deposited on glass substrate in the reaction chamber. TiO_2 films with different thicknesses (from 100 nm to 500 nm) were prepared for comparison.

Table 3.5 Deposition condition of film thickness dependence.

Solute	TTIP
Solvent	Ethanol
Concentration (mol/L)	0.10
Substrate	Glass (Eagle XG)
Deposition temperature (°C)	400
Carrier gas, flow rate (L/min)	Compressed air, 2.5
Dilution gas, flow rate (L/min)	Compressed air, 4.5

3.4.2 Results and discussion

The X-ray diffraction pattern of TiO_2 films with different thicknesses deposited by mist CVD is shown in Fig. 3.12. The observed peaks are corresponding to the diffractions from (101), (200), (211), (201), (204), and (215) surface of the anatase phase of TiO_2. The main peak is corresponding to the diffraction from (101) surface. The intensity of (101) peaks increases gradually with the thickness of film increasing from 100 nm to 500 nm. It indicates that the crystallinity of TiO_2 films increases with the increasing of film thickness and TiO_2 preferred to

grow in the (101) direction.

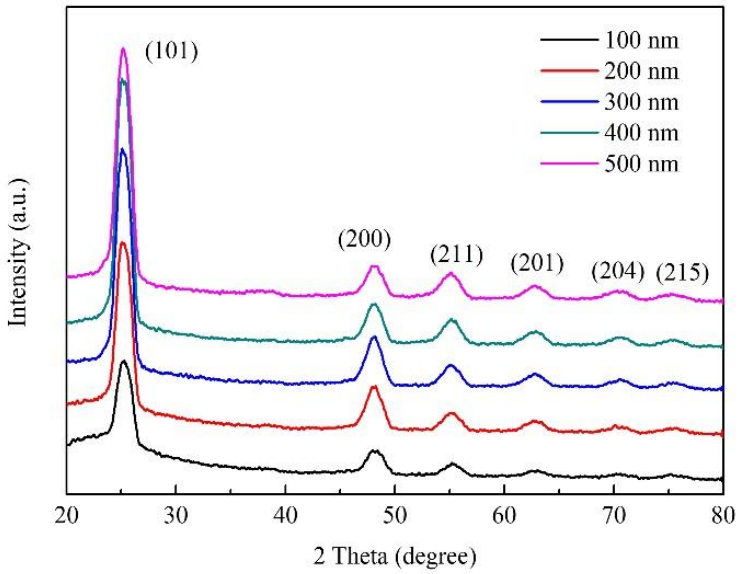

Fig. 3.12 GIXRD patterns of TiO_2 films with different thicknesses deposited by mist CVD.

Figure 3.13 shows the Raman spectra of TiO_2 films with different thicknesses deposited by mist CVD. Three peaks are observed in the Raman spectra. The peaks at 398 cm^{-1} and 638 cm^{-1} are corresponding to the B_{1g} mode and E_g mode of anatase phase TiO_2 respectively. The peak at 514 cm^{-1} is a doublet of the A_{1g} and B_{1g} modes of the anatase phase TiO_2. No peaks of the rutile or brookite phase TiO_2 are observed in the Raman spectra. It indicates the TiO_2 films are pure anatase phase, which is consistent with the XRD result. The intensity of all Raman peaks increases gradually with the thickness of film increasing from 100 nm to 500 nm, which indicates that the crystallinity of TiO_2 films increases gradually.

Figure 3.14 shows the AFM images of TiO_2 films with different thicknesses deposited by mist CVD. The RMS values of the surface roughness of the films were obtained based on the AFM data and shown in Table 3.6. The obtained TiO_2 films with different thicknesses are uniform. With the thickness increasing from 100 nm to 500 nm, the RMS roughness of TiO_2 film shows tendency of increase. This is because the TiO_2 preferred to grow in (101) direction. With the growth of TiO_2, the difference of TiO_2 nanostructure size increased.

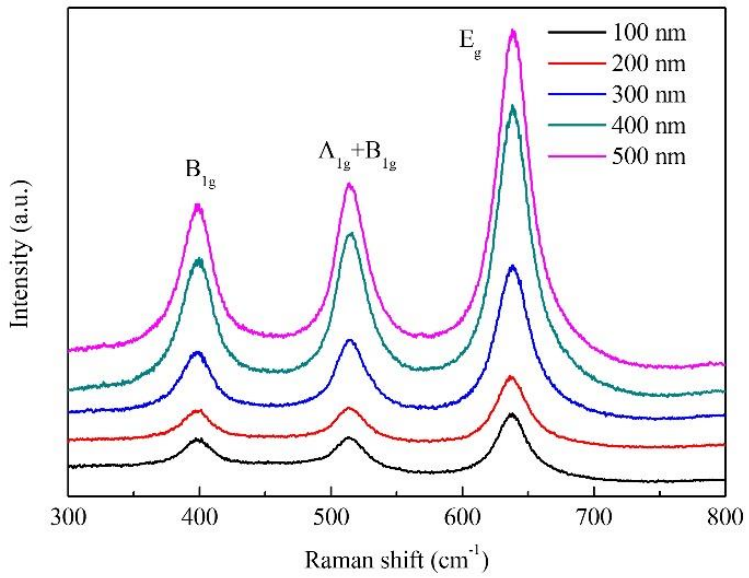

Fig. 3.13 Raman spectra of TiO_2 films with different thicknesses deposited by mist CVD.

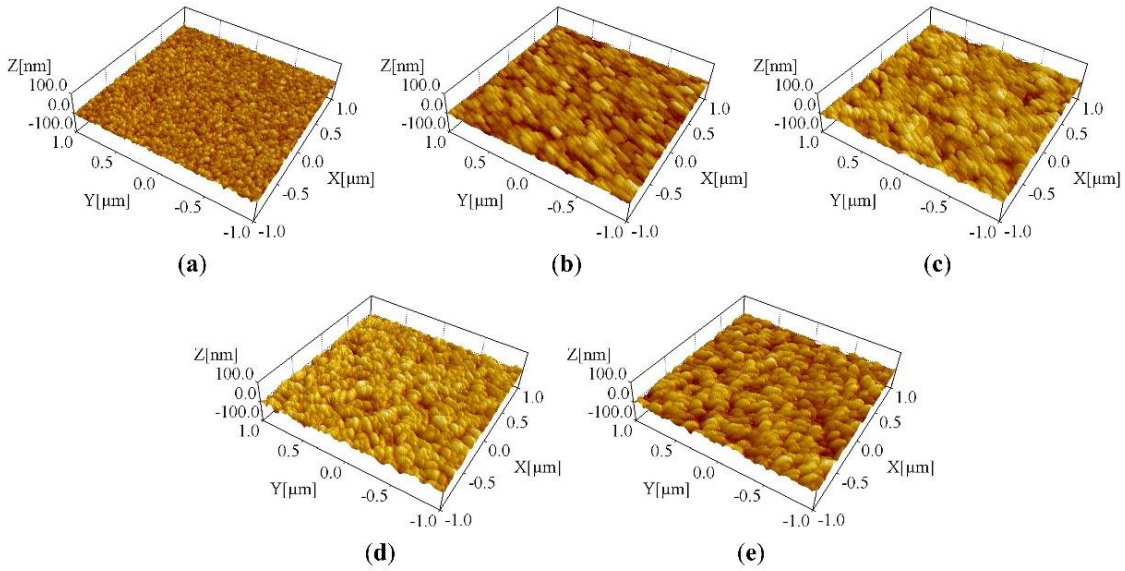

Fig. 3.14 AFM images of TiO_2 films deposited with different thicknesses by mist CVD method. ((**a**) 100 nm; (**b**) 200 nm; (**c**) 300 nm; (**d**) 400 nm; (**e**) 500 nm).

Table 3.6 Surface roughness of TiO_2 films with different thicknesses.

Film thickness (nm)	Surface roughness (nm)
100	3.89
200	3.73
300	6.00
400	7.67
500	7.12

The transmission spectra of TiO_2 films with different thicknesses deposited by mist CVD is shown in Fig. 3.15. It is found that the transmittance of TiO_2 films in the visible region is almost independent of film thickness. The transmittance of TiO_2 films is more than 75% in the visible region.

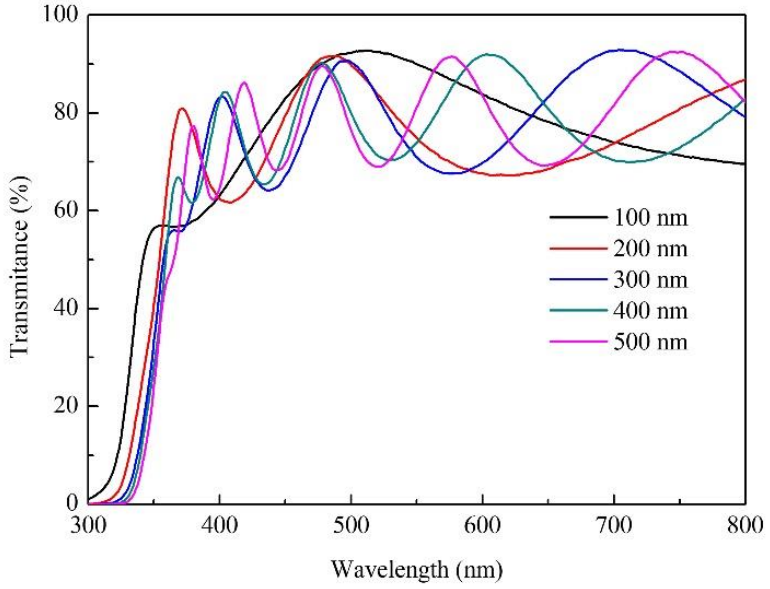

Fig. 3.15 Transmittance of TiO_2 films deposited with different thicknesses by mist CVD.

3.4.3 Summary

The crystallinity of TiO_2 films increases with the increasing of film thickness. The transmittance of all TiO_2 films is more than 75% in the visible region and almost independent of film thickness. The surface of obtained TiO_2 films with different thicknesses are uniform. With the thickness increasing, the roughness of TiO_2 film shows tendency of increase.

3.5 Effects of substrate on the properties of TiO_2 thin films

3.5.1 Experimental

In order to investigate the effect of substrates on structural and optical properties of TiO_2 films fabricated by mist CVD method, four kinds of substrates including quartz glass (MITORIKA GLASS), glass (Corning, EAGLE XG), gallium oxide (5.7 wt.%) doped zinc oxide (GZO, 300 nm, on EAGLE XG glass) substrate and p-type silicon wafer <100> (ADVANTEC Co., Ltd) were selected for comparison because they have been widely used for

the research and manufacture of electronic devices, especially thin-film gas sensors and solar cells. The deposition condition is shown in Table 3.7. During the mist CVD process, a solution of mixed precursors was prepared by dissolving TTIP in ethanol. Mist droplets were generated from the solution by ultrasonic transducers and transferred to the reaction chamber by compressed air. The substrate was set in the reaction chamber, which was heated and kept at 400 ˚C during the deposition process. TiO_2 films with a thickness of 300 nm were obtained on different substrates after deposition.

Table 3.7 Deposition condition of substrate dependence.

Solute	TTIP
Solvent	Ethanol
Concentration (mol/L)	0.10
Substrate	Quartz glass, Glass, GZO, Silicon
Deposition temperature (°C)	400
Carrier gas, flow rate (L/min)	Compressed air, 2.5
Dilution gas, flow rate (L/min)	Compressed air, 4.5

3.5.2 Results and discussion

Figure 3.16a shows the GIXRD patterns of TiO_2 films grown on different substrates. The observed peaks corresponded to the diffractions from (101), (112), (200), (211), (201), (204), and (215) surface of the anatase phase of TiO_2. All of the diffraction peaks were identified and corresponded to the anatase phase of TiO_2 (JCPDS 21-1272). This result suggests pure anatase phase TiO_2 films were obtained on different substrates. The dominant peaks of each GIXRD patterns were the same as the diffraction from (101) orientation, indicating that the preferred growth of TiO_2 films existed on different substrates. The peak intensity and FWHM of (101) diffraction peak was shown in Fig. 3.16b. It was found that the TiO_2 films deposited on quartz glass and glass with higher peak intensity and narrower FWHM showed better crystallinity than those grown on GZO and p-type silicon substrates.

As is well established, the preferred orientation of a certain crystal surface in the film can be described with the evaluation of the texture coefficient (TC), as shown in equation (3.4) [42,43].

$$TC = \frac{I/I_0}{(1/N)\sum I/I_0} \tag{3.4}$$

where I is the intensity of each diffraction peak from measured sample; I_0 is the standard intensity referred to American society for testing and materials (ASTM) of each diffraction peak from the corresponding powder; and N is the number of diffraction peaks considered in the analysis. As the definition, a TC value above 1 means that direction is a preferred growth orientation. If TC value is higher, the preferred growth in that orientation is higher too.

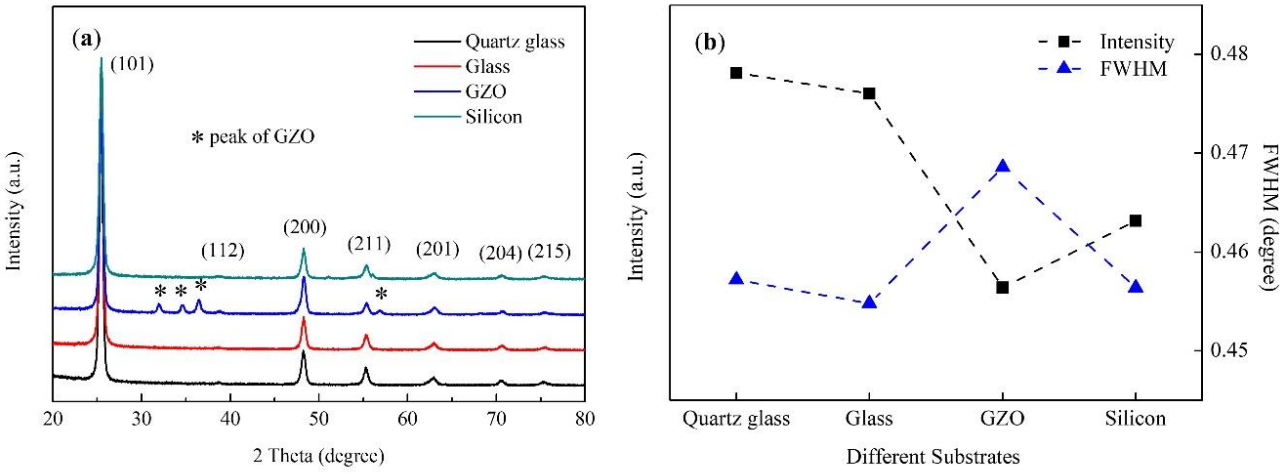

Fig. 3.16 GIXRD results of TiO_2 films deposited on different substrates by mist CVD. ((**a**) GIXRD patterns of TiO_2 films; (**b**) GIXRD intensity of TiO_2 films).

The TC value of TiO_2 films calculated based on the GIXRD data is shown in Table 3.8. From the TC value results, it can be inferred that the preferred growth of the TiO_2 film was influenced by the substrates. The TiO_2 film grown on glass substrate showed the highest TC value and narrowest FWHM for (101) peak, indicating that TiO_2 film with best crystallinity was obtained on glass. The crystallinity of TiO_2 film on GZO substrate was the worst due to the lowest TC value and highest value of FWHM.

Table 3.8 Value of texture coefficient

Substrate	Texture coefficient						
	(101)	(112)	(200)	(211)	(201)	(204)	(215)
Quartz glass	2.13	0.61	1.15	0.98	0.66	0.94	0.52
Glass	2.21	0.55	1.19	0.92	0.69	0.94	0.50
GZO	1.82	0.71	1.50	0.75	0.74	0.97	0.51
Silicon	2.09	0.61	1.25	0.95	0.63	0.92	0.56

Figure 3.17a shows the Raman spectra of TiO_2 films deposited on different substrates by mist CVD. Three peaks were observed in the Raman spectra. The peaks at 398 cm^{-1} and 638 cm^{-1} corresponded to the B_{1g} mode and E_g mode of anatase phase TiO_2 respectively. The peak at 514 cm^{-1} was a doublet of the A_{1g} and B_{1g} modes of the anatase phase TiO_2. However, in the case of TiO_2 film on silicon substrate, the anatase peak at 514 cm^{-1} was completely overlapped by a strong substrate peak (LO phonon line of silicon at 520 cm^{-1}). There were no peaks of the rutile or brookite phase TiO_2 observed in the Raman spectra, which indicated the obtained TiO_2 films were pure anatase phase on four kinds of substrates. This result was in a good agreement with the GIXRD result.

The intensities of B_{1g} mode and E_g mode Raman peaks are shown in Fig. 3.17b. The ratio of B_{1g} peak intensity to E_g peak intensity was calculated and shown as dash line with point. The TiO_2 on quartz glass and silicon showed a greater intensity of B_{1g} and E_g peaks than those on glass and GZO substrates. It is reported that the Raman peak intensity of anatase phase TiO_2 has a relationship with the exposed facets. The intensity of B_{1g} peak is proportional to the number of exposed {001} facets, and the intensity of E_g peak is proportional to the number of exposed {101} facets [44]. Therefore, the percentage of exposed {001} facets in anatase TiO_2 could be compared by the peak intensity ratio of the B_{1g} and E_g peaks.

As shown in Fig. 3.17b, for TiO_2 film on silicon, the ratio of B_{1g} peak intensity to E_g peak intensity was higher than other substrates, which suggested that the TiO_2 film obtained on silicon had a higher percentage of exposed {001} facets. Accordingly, the TiO_2 film deposited on silicon is expected to have better sensitivity to oxygen and acetone gases.

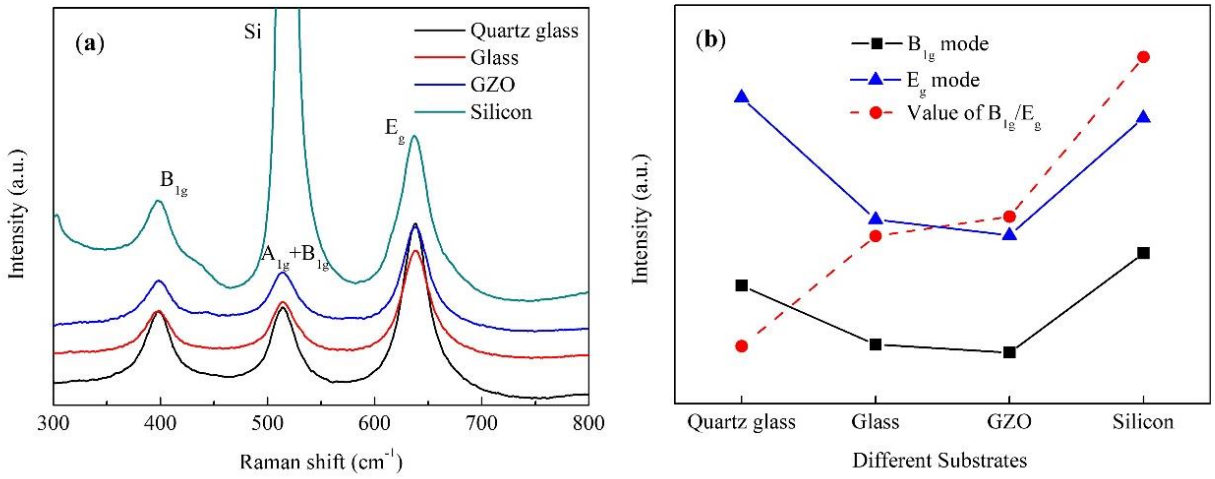

Fig. 3.17 Raman results of TiO_2 films deposited on different substrates by mist CVD. ((**a**) Raman spectra of TiO_2 films; (**b**) Raman intensity of TiO_2 films).

The surface morphology of TiO_2 films deposited on different substrates by mist CVD was evaluated by AFM (the scan area is 2 × 2 μm^2). AFM images of TiO_2 films on different substrates are shown in Fig. 3.18. As observed in the AFM images, the obtained TiO_2 films on different substrates were uniform and flat. The RMS values of the film surface roughness are summarized in Table 3.9. The RMS roughness of TiO_2 films on all substrates was less than 10 nm, indicating that TiO_2 films with good uniformity were obtained on all substrates. The surface area of the TiO_2 films, as shown in Table 3.9, were obtained from the AFM data. Usually, a larger surface area will enhance the gas adsorption on surface, which will contribute to a higher gas sensitivity. The surface area of TiO_2 films deposited on p-type silicon substrate was larger than that of TiO_2 films deposited on quartz glass, glass and GZO substrates. Therefore, the TiO_2 films deposited on p-type silicon substrate is expected to have a higher gas sensitivity than those deposited on quartz glass, glass and GZO substrates.

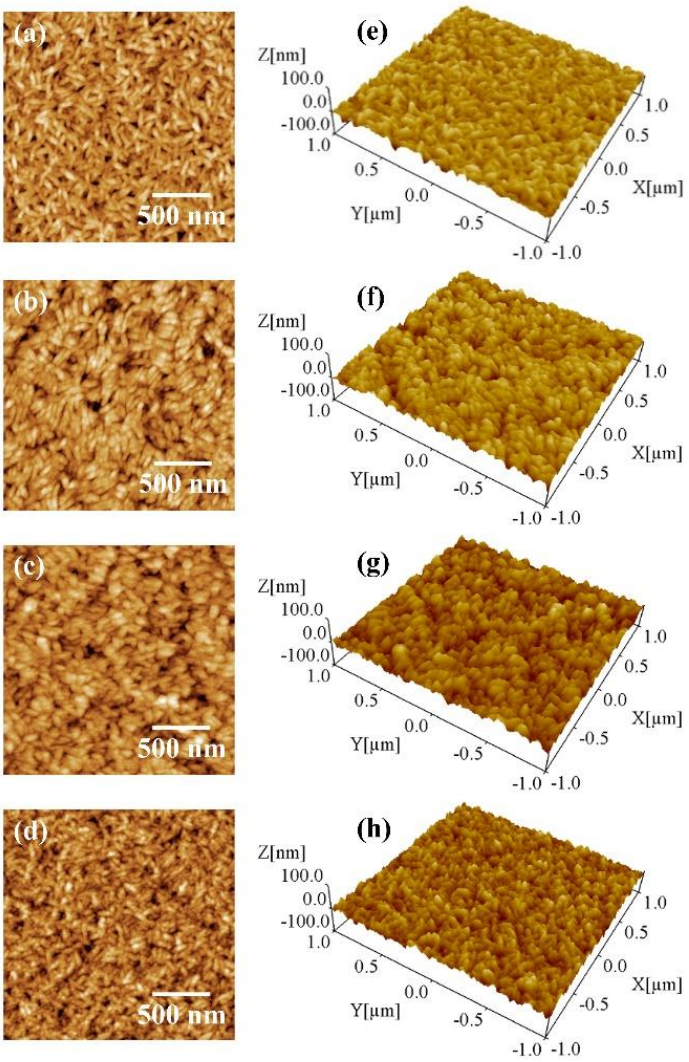

Fig. 3.18 AFM images of TiO_2 films deposited on different substrates by mist CVD.
((**a**), (**e**): quartz glass; (**b**), (**f**): glass; (**c**), (**g**): GZO; (**d**), (**h**): silicon).

Table 3.9 Surface roughness and surface area of TiO_2 films deposited on different substrates.

Substrate	Surface roughness (nm)	Surface area (μm^2)
Quartz gass	7.71	4.87
Glass	9.62	4.82
GZO	8.88	4.85
Silicon	8.18	5.04

Figure 3.19 shows the SEM images of TiO_2 films deposited on different substrates by mist CVD. In the top view images, intertwined TiO_2 nanosheets were observed on all substrates. As shown in the top view images, TiO_2 films with good uniformity were obtained on all of the

substrates. It was observed that the TiO_2 nanosheets on quartz glass and p-type silicon were more vertical to the substrates from the SEM cross section view images. From the SEM results, it was confirmed that the precise control of the growth orientation, uniformity and grain size of thin film were achieved.

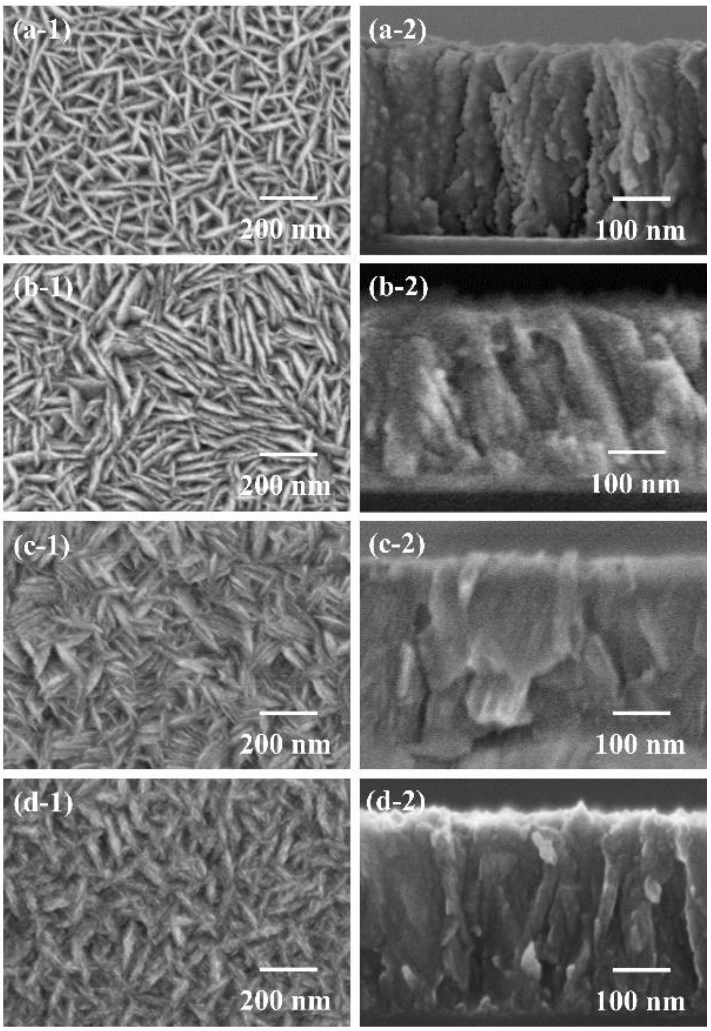

Fig. 3.19 SEM images of TiO_2 films deposited on different substrates by mist CVD.
((**a**) quartz glass; (**b**) glass; (**c**) GZO; (**d**) silicon; (**1**) top view; (**2**) cross section view).

The transmission spectra of TiO_2 films deposited on different substrates by mist CVD is shown in Fig. 3.20. The transmittance of TiO_2 films on glass, quartz glass, and GZO was higher than 75% in the visible region. It was confirmed that the substrate had little influence on the transmittance of TiO_2 films in the visible region. The high transmittance of the obtained TiO_2 films was due to the good uniformity and vertical nanostructures of TiO_2 films, as shown in the SEM results. The TiO_2 films grown on quartz glass and p-type silicon, which are more uniform

and more vertical to the substrates, are expected to have greater gas sensitivity.

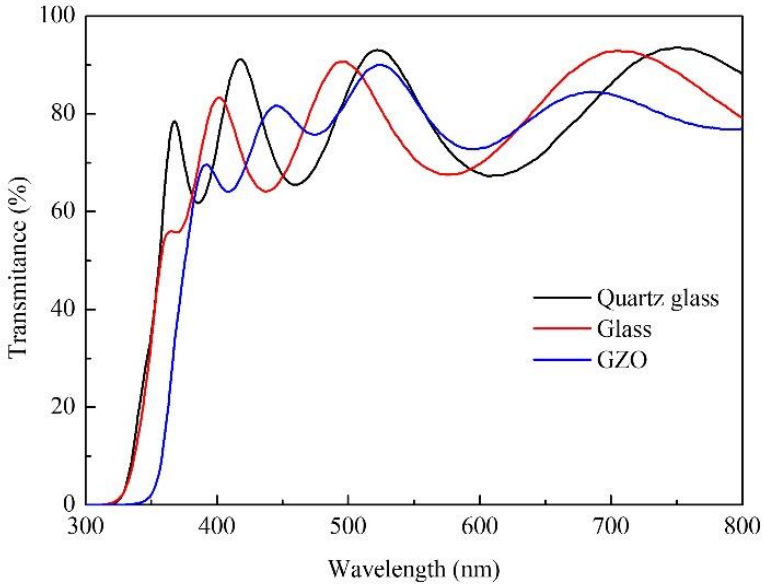

Fig. 3.20 Transmittance of TiO_2 films deposited on different substrates by mist CVD.

3.5.3 Summary

Pure anatase phase TiO_2 films were synthesized on quartz glass, glass, GZO and p-type silicon substrates by mist CVD. The TiO_2 films deposited on all substrates showed the same dominant (101) growth orientation. The crystallinity of TiO_2 films grown on different substrates increased in an order of glass, quartz glass, p-type silicon and GZO. It was confirmed by Raman spectroscopy that TiO_2 films deposited on four kinds of substrates were pure anatase phase, which was in a good agreement with the GIXRD result. The TiO_2 thin film deposited on p-type silicon showed the highest percentage of exposed {001} facets. The TiO_2 films with good uniformity were obtained on all of the substrates. The surface area of TiO_2 films deposited on p-type silicon substrate was larger than that of TiO_2 films deposited on quartz glass, glass and GZO substrates. The precise control of the growth orientation, uniformity and grain size of thin film were achieved. The transmittance of TiO_2 films on quartz glass, glass and GZO substrates was higher than 75% in the visible region.

3.6 Conclusions

In this chapter, pure anatase phase TiO_2 films were fabricated with ethanol as solvent by mist

CVD. The effects of deposition temperature, TTIP concentration, film thickness and substrate on the properties of TiO_2 films were investigated.

1) The crystallinities of TiO_2 films were significantly improved by increasing deposition temperature. Pure anatase phase TiO_2 films with good uniformity were obtained from 300 °C to 400 °C. The roughnesses of all TiO_2 films were less than 7 nm and showed a variation tendency of increase as the deposition temperature increased from 200 °C to 400 °C.

2) When the TTIP concentration increased from 0.05 mol/L to 0.40 mol/L, the aspect ratio of TiO_2 nanosheets first increased then decreased. The highest aspect ratio of TiO_2 nanosheets was obtained at a TTIP concentration of 0.20 mol/L. The deposition rate of TiO_2 films had the same variation tendency with aspect ratio. The roughnesses of all TiO_2 films were less than 10 nm regardless of TTIP concentration variation. The crystallinity of TiO_2 films showed a variation tendency of increase as the TTIP concentration increased from 0.05 mol/L to 0.40 mol/L. The best crystallinity was obtained under the TTIP concentration of 0.05 mol/L.

3) The crystallinity of TiO_2 films increases with the increasing of film thickness. The transmittance of all TiO_2 films is more than 75% in the visible region and almost independent of film thickness. The surface of obtained TiO_2 films with different thicknesses are uniform. With the thickness increasing, the roughness of TiO_2 film shows tendency of increase.

4) The TiO_2 films deposited on all substrates showed the same dominant (101) growth orientation. The crystallinity of TiO_2 films grown on different substrates increased in an order of glass, quartz glass, p-type silicon and GZO. It was confirmed by Raman spectroscopy that TiO_2 films deposited on four kinds of substrates were pure anatase phase, which was in a good agreement with the GIXRD result. The TiO_2 thin film deposited on p-type silicon showed the highest percentage of exposed {001} facets. The TiO_2 films with good uniformity were obtained on all of the substrates. The surface area of TiO_2 films deposited on p-type silicon substrate was larger than that of TiO_2 films deposited on quartz glass, glass and GZO substrates. The precise control of the growth orientation, uniformity and grain size of thin film were achieved. The transmittance of TiO_2 films on quartz glass, glass and GZO substrates was higher than 75% in the visible region.

3.7 References

[1] M.V. Baryshnikova, L.A. Filatov, A.S. Petrov, S.E. Alexandrov. CVD deposited titania thin films for gas sensors with improved operating characteristics. Chem. Vap. Depos. 21 (2015) 327-333.

[2] D.S.R. Josephine, K.J. Babu, G.P.G. Kumar, K. Sethuraman. Titanium dioxide anchored graphene oxide nanosheets for highly selective voltammetric sensing of dopamine. Microchim. Acta 184 (2017) 781-790.

[3] L. Chen, X. Liao, W. Jiang. Effect of heat treatment temperature on super-hydrophilic property of enamels with titanium dioxide thin film. J. Sol-Gel Sci. Technol. 80 (2016) 606-611.

[4] V. Scuderi, M.A. Buccheri, G. Impellizzeri, A.D. Mauro, G. Rappazzo, K. Bergum, B.G. Svensson, V. Privitera. Photocatalytic and antibacterial properties of titanium dioxide flat film. Mater. Sci. Semicond. Process. 42 (2016) 32-35.

[5] B. Scheffel, T. Modes, C. Metzner. Reactive high-rate deposition of titanium oxide coatings using electron beam evaporation, spotless arc and dual crucible. Surf. Coat. Technol. 287 (2016) 138-144.

[6] M. Mazur. Analysis of the properties of functional titanium dioxide thin films deposited by pulsed DC magnetron sputtering with various O_2: Ar ratios. Opt. Mater. 69 (2017) 96-104.

[7] B. Karunagaran, P. Uthirakumar, S.J. Chung, S. Velumani, E.K. Suh. TiO_2 thin film gas sensor for monitoring ammonia. Mater. Charact. 58 (2007) 680–684.

[8] R. Klaysri, M. Ratova, P. Praserthdam, P.J. Kelly. Deposition of Visible Light-Active C-Doped Titania Films via Magnetron Sputtering Using CO_2 as a Source of Carbon. Nanomaterials 7 (2017) 113.

[9] K.-H. Choi, K.-B. Chung, H.-K. Kim. d-orbital ordering of oxygen-deficient amorphous and anatase TiO_{2-x} channels for high mobility thin film transistors. Appl. Phys. Lett. 102 (2013) 153511.

[10] C. Jin, B. Liu, Z. Lei, J. Sun. Structure and photoluminescence of the TiO_2 films grown by atomic layer deposition using tetrakis-dimethylamino titanium and ozone. Nanoscale Res. Lett. 10 (2015) 95-104.

[11] Y. Chimupala, G. Hyett, R. Simpson, R. Mitchell, R. Douthwaite, S.J. Milne, R.D. Brydson. Synthesis and characterization of mixed phase anatase TiO_2 and sodium-doped TiO_2(B) thin films by low pressure chemical vapour deposition (LPCVD). RSC Adv. 4 (2014) 48507-48515.

[12] T. Ban, T. Nakatani, Y. Ohya. Morphology of anatase crystals and their aggregates synthesized hydrothermally from aqueous mixtures of titanium alkoxide and different alkylammonium hydroxides. J. Ceram. Soc. Jpn. 117 (2009) 268-272.

[13] S.A. Campbell, H.S. Kim, D.C. Gilmer, B. He, T. Ma, W.L. Gladfelter. Titanium dioxide (TiO_2)-based gate insulators. IBM J. Res. Dev. 43 (1999) 383-392.

[14] J. Wu, S. Hao, J. Lin, M. Huang, Y. Huang, Z. Lan, P. Li. Crystal morphology of anatase titania nanocrystals used in dye-sensitized solar cells. Cryst. Growth Des. 8 (2008) 247-252.

[15] J. Zhang, J. Liao, F. Yang, M. Xu, S. Lin. Regulation of the electroanalytical performance of ultrathin titanium dioxide nanosheets toward lead ions by non-metal doping. Nanomaterials 7 (2017) 327.

[16] P.I. Gouma, M.J. Mills. Anatase-to-rutile transformation in titania powders. J. Am. Ceram. Soc. 84 (2001) 619-622.

[17] R.L. Penn, J.F. Banfield. Formation of rutile nuclei at anatase {112} twin interfaces and the phase transformation mechanism in nanocrystalline titania. Am. Miner. 84 (1999) 871-876.

[18] Y. Zhou, K.A. Fichthorn. Microscopic view of nucleation in the anatase-to-rutile transformation. J. Phys. Chem. C 116 (2012) 8314-8321.

[19] G.H. Lee, J.M. Zuo. Growth and phase transformation of nanometer-sized titanium oxide powders produced by the precipitation method. J. Am. Ceram. Soc. 87 (2004) 473-479.

[20] D.A.H. Hanaor, C.C. Sorrell. Review of the anatase to rutile phase transformation. J. Mater. Sci. 46 (2011) 855-874.

[21] L. Romero, A.B. Jorge, P.F. McMillan, R. Binions. Enhanced photocatalytic properties of titanium dioxide thin films produced from the ac electric field assisted chemical vapor deposition of titanium (IV) chloride in toluene. ECS J. Solid State Sci. Technol. 3 (2014) N107-N113.

[22] R.A. Fisher, M.R. Watt, R. Konjeti, W.J. Ready. Atomic layer deposition of titanium oxide for pseudocapacitive functionalization of vertically-aligned carbon nanotube supercapacitor electrodes. ECS J. Solid State Sci. Technol. 4 (2015) M1-M5.

[23] B. Comert, N. Akin, M. Donmez, S. Saglam, S. Ozcelik. Titanium dioxide thin films as methane gas sensors. IEEE Sens. J. 16 (2016) 8890-8996.

[24] H. Yoon, B. Joshi, S.-H. Na, S.S. Yoon. Antibacterial activity and photocatalysis of electrosprayed titania films. J. Electrochem. Soc. 159 (2012) H823-H827.

[25] S. Dhanapandian, A. Arunachalam, C. Manoharan. Effect of deposition parameters on the properties of TiO_2 thin films prepared by spray pyrolysis. J. Sol-Gel Sci. Technol. 77 (2016) 119-135.

[26] P. Reckers, M. Dimamay, J. Klett, S. Trost, K. Zilberberg, T. Riedl, B.A. Parkinson, J. Brötz, W. Jaegermann, T. Mayer. Deep and shallow TiO_2 gap states on cleaved anatase single crystal (101) surfaces, nanocrystalline anatase films, and ALD titania ante and post annealing. J. Phys. Chem. C, 119 (2015) 9890-9898.

[27] V.G. Krishnan, A. Purushothaman, P. Elango. Effect of thickness on the physical properties and gas sensing application: anatase titanium dioxide nanofilms by automated nebulizer spray pyrolysis (ANSP). J. Mater. Sci.: Mater. Electron. 28 (2017) 11473-11481.

[28] M. Reinke, E. Ponomarev, Y. Kuzminykh, P. Hoffmann. Combinatorial characterization of TiO_2 chemical vapor deposition utilizing titanium isopropoxide. ACS Comb. Sci. 17 (2015) 413-420.

[29] X. Li, C. Li, T. Kawaharamura, D. Wang, N. Nitta, M. Furuta, H. Furuta, A. Hatta. Fabrication of zinc oxide nanostructures by mist chemical vapor deposition. Trans. Mater. Res. Soc. Jpn. 39 (2014) 161-164.

[30] H.-Y. Liu, Y.-L. Hsu, H.-Y. Su, R.-C. Huang, F.-Y. Hou, G.-C. Tu, W.-H. Liu. A comparative study of amorphous, anatase, rutile, and mixed phase TiO_2 films by mist chemical vapor deposition and ultraviolet photodetectors applications. IEEE Sens. J. 18 (2018) 4022-4029.

[31] H.-Y. Liu, S.-H. Hong, W.-C. Sun, S.-Y. Wei, S.-M. Yu. TiO_2-based metal-semiconductor-metal ultraviolet photodetectors deposited by ultrasonic spray pyrolysis technique. IEEE Trans. Electron. Devices 63 (2016) 79-85.

[32] T. Kawaharamura, K. Mori, H. Orita, T. Shirahata, S. Fujita, T. Hirao. Effect of O_3 and aqueous ammonia on crystallization of MgO thin film grown by mist chemical vapor deposition. Jpn. J. Appl. Phys. 52 (2013) 035501.

[33] P. Buerger, D. Nurkowski, J. Akroyd, S. Mosbach, M. Kraft. First-principles thermochemistry for the thermal decomposition of titanium tetraisopropoxide. J. Phys. Chem. A 119 (2015) 8376-8378.

[34] M. Reinke, Y. Kuzminykh, P. Hoffmann. Low temperature chemical vapor deposition using atomic layer deposition chemistry. Chem. Mater. 27 (2015) 1604-1611.

[35] C.J. Taylor, D.C. Gilmer, D.G. Colombo, G.D. Wilk, S.A. Campbell, J. Roberts, W.L. Gladfelter. Does chemistry really matter in the chemical vapor deposition of titanium dioxide? Precursor and kinetic effects on the microstructure of polycrystalline films. J. Am. Chem. Soc. 121 (1999) 5220-5229.

[36] M. Reinke, E. Ponomarev, Y. Kuzminykh, P. Hoffmann. Surface kinetics of titanium isopropoxide in high vacuum chemical vapor deposition. J. Phys. Chem. C 119 (2015) 27965-27971.

[37] A.M. Johnson, P.C. Stair. Alternative low-pressure surface chemistry of titanium tetraisopropoxide on oxidized molybdenum. J. Phys. Chem. C 118 (2014) 29361-29369.

[38] H. Yang, C. Sun, S. Qiao, J. Zou, G. Liu, S.C. Smith, H. Cheng, G. Lu. Anatase TiO_2 single crystals with a large percentage of reactive facets. Nature 453 (2008) 638-641.

[39] B. Sajjadi, S. Asgharzadehahmadi, P. Asaithambi, A.A.A. Raman, R. Parthasarathy. Investigation of mass transfer intensification under power ultrasound irradiation using 3D computational simulation: A comparative analysis. Ultrason. Sonochem. 34 (2017) 504-518.

[40] L. Hao, K. Miyazawa, H. Yoshida, Y. Lu. Visible-light-driven oxygen vacancies and Ti^{3+} co-doped TiO_2 coatings prepared by mechanical coating and carbon reduction. Mater. Res. Bull. 97 (2018) 13-18.

[41] M. Xing, J. Zhang, F. Chen, B. Tian. An economic method to prepare vacuum activated photocatalysts with high photo-activities and photosensitivities. Chem. Commun. 47 (2011) 4947-4949.

[42] K.H. Kim, J.S. Chun. X-ray studies of SnO_2 prepared by chemical vapour deposition. Thin Solid Films 141 (1986) 287-295.

[43] H.R. Moutinho, F.S. Hasoon, F. Abulfotuh, L.L. Kazmerski. Investigation of polycrystalline CdTe thin films deposited by physical vapor deposition, close-spaced sublimation, and sputtering. J. Vac. Sci. Technol. A 13 (1995) 2877-2883.

[44] F. Tian, Y. Zhang, J. Zhang, C. Pan. Raman spectroscopy: a new approach to measure the percentage of anatase TiO_2 exposed (001) facets. J. Phys. Chem. C 116 (2012) 7515-7519.

Chapter 4

Fabrication and characterization of anatase phase TiO_2 thin films with methanol as solvent by mist CVD method

4.1 Introduction

For anatase phase TiO_2, the surface energy of {001} facets is much higher than the {101} and other facets [1-10]. Due to the high surface energy, the {001} facets were more reactive for the adsorption of oxygen and acetone gases and the photodegradation of organic pollutants, which significantly enhanced the gas sensitivity and photocatalytic activity of the pure anatase phase TiO_2 [11,12]. Anatase TiO_2 films can be synthesized by various methods. However, the well-controlled growth of pure anatase TiO_2 thin film is still a critical issue [13-19]. For most anatase TiO_2 film deposition methods, it is difficult to control the growth of {001} facets. Thus, the anatase TiO_2 films obtained by these methods suffer from a low gas sensitivity and a low photocatalytic efficiency in the gas sensing application.

In chapter 3, pure anatase TiO_2 thin films with good uniformity and crystallinity were successfully synthesized by using a mixture of TTIP and ethanol as precursor solution by mist CVD. However, the {001} facets were not obtained from the synthesized TiO_2 films. In order to solve this problem, one alternative solution is to adjust the precursor solution.

Compared with ethanol, methanol is much easier to atomize ultrasonically. The deposition rate of TiO_2 thin films will be more controllable by using methanol as solvent. However, the TTIP is not stable in pure methanol. Recently, it was found that a stable mixture of TTIP and methanol could be obtained by adding acetylacetone as stabilizer.

Until now, the growth of preferred {001} facets could be controlled by only a few methods. Among these approaches, the F^- ion methods were mostly used to enhance the growth of {001} facets because F^- could be strongly absorbed on {001} facets. However, F^- is a dangerous ion which is corrosive to the fabrication equipment and harmful to human skin. Compared with the use of F^-, we found that changing the water-to-methanol ratio is a safer method to control the growth of {001} facets.

As discussed in chapter 3, the thermal decomposition mechanism of TTIP could be separated as two reactions including both hydrolysis (Eq. (4.1)) and pyrolysis (Eq. (4.2)) [20].

$$Ti(OC_3H_7)_4 + 2H_2O \rightarrow TiO_2 + 4C_3H_7OH \quad (4.1)$$

$$Ti(OC_3H_7)_4 \rightarrow TiO_2 + 4C_3H_6 + 2H_2O \quad (4.2)$$

The hydrolysis of TTIP was widely used to fabricate TiO_2 films by atomic layer deposition (ALD) and hydrothermal methods [21-24]. The pyrolysis of TTIP was mostly used in various chemical vapor deposition (CVD) methods [1,14,25,26]. In most of the publications, the anatase phase TiO_2 was the predominant product when TTIP was applied as precursor. Due to the influence of deposition process, the rutile phase TiO_2 was also obtained from TTIP as predominant product under some deposition conditions [25,26].

For a chemical reaction, the reaction rate constant has a significant influence on the reaction rate. As we discussed in chapter 3, when the deposition temperature of TiO_2 films was 400 °C, which is the optimized temperature obtained from our previous research, the reaction rate constant of pyrolysis was much higher than that of hydrolysis. Even the pyrolysis of TTIP could provide a small amount of water for the hydrolysis of TTIP, the amount of water generated from the pyrolysis was limited by the reaction rate of pyrolysis and much less than the amount of water added in the precursor solution. Therefore, during the decomposition of TTIP at 400 °C, the pyrolysis was dominant reaction without adding water. However, the dominant reaction of TTIP could be changed from pyrolysis to hydrolysis by adding water. In this research, the effects water-to-methanol ratio were investigated for comparing the TiO_2 films obtained from hydrolysis and pyrolysis.

4.2 Effects of film thickness on the properties of TiO_2 thin films

4.2.1 Experimental

AZO (2 wt. %) thin films with 300nm thickness were deposited on alkali-free glass sheets (Eagle XG, Corning) by a conventional 13.56 MHz RF magnetron sputtering system. The deposition condition of AZO films is shown in Table 4.1.

Following the deposition of AZO films, TiO_2 films were deposited on AZO substrates by mist CVD. The precursor solution was prepared by dissolving acetylacetone and TTIP in a mixture of water and methanol (Wako Pure Chemical Industries, Ltd., Osaka, Japan). The water-to-methanol volume ratio was set as 5 %. TiO_2 films with different thicknesses (from 100 nm to500 nm) were prepared for comparison. The deposition condition of TiO_2 films is shown in Table 4.2.

Table 4.1 Deposition condition of AZO film.

Target	AZO (2 wt.%)
Working distance (mm)	60
Working gas, flow rate (sccm)	Argon, 30
Pressure (Pa)	1
Deposition temperature (˚C)	150
RF power (W)	60

Table 4.2 Deposition condition of film thickness dependence.

Substrate	AZO on glass
Solute	TTIP, Acetylacetone
Solvent	Water, Methanol
Concentration of TTIP (mol/L)	0.02
Concentration of acetylacetone (mol/L)	0.06
Water-to-methanol ratio (%)	5
Deposition Temperature (℃)	400
Film thickness (nm)	100, 200, 300, 400, 500
Carrier Gas, Flow Rate (L/min)	N_2, 2.5
Dilution Gas, Flow Rate (L/min)	N_2, 4.5

4.2.2 Results and discussion

The SEM images of TiO_2 films deposited with different thicknesses by mist CVD are displayed in Fig. 4.1. From the top view SEM images, the TiO_2 films deposited with different thicknesses showed good uniformity. When the film thickness increased from 100 nm to 300 nm, the average grain size of TiO_2 films increased. With the film thickness increased from 300 nm to 500 nm, the

average grain size of TiO_2 films decreased.

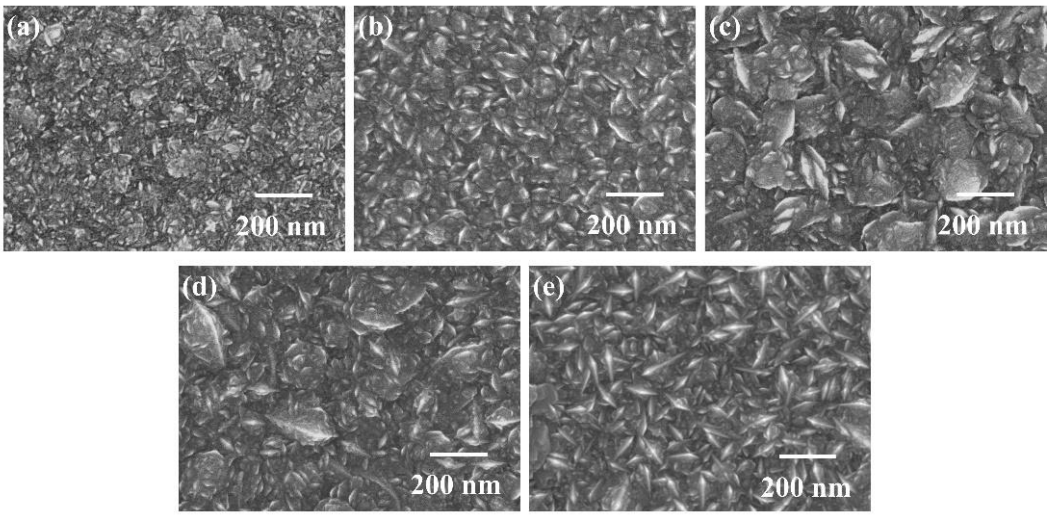

Fig. 4.1 SEM images of TiO_2 films deposited with different thicknesses by mist CVD method. ((**a**) 100 nm; (**b**) 200 nm; (**c**) 300 nm; (**d**) 400 nm; (**e**) 500 nm).

Figure 4.2 shows the AFM images of TiO_2 films with different thicknesses deposited by mist CVD. The obtained TiO_2 films with different thicknesses are uniform. The RMS values of the surface roughness and surface area were obtained from the AFM data (the scan area is 2×2 μm^2) and summarized in Table 4.3. With the thickness increasing from 100 nm to 500 nm, the RMS roughness of TiO_2 film increased gradually, and the surface area showed a trend of increase.

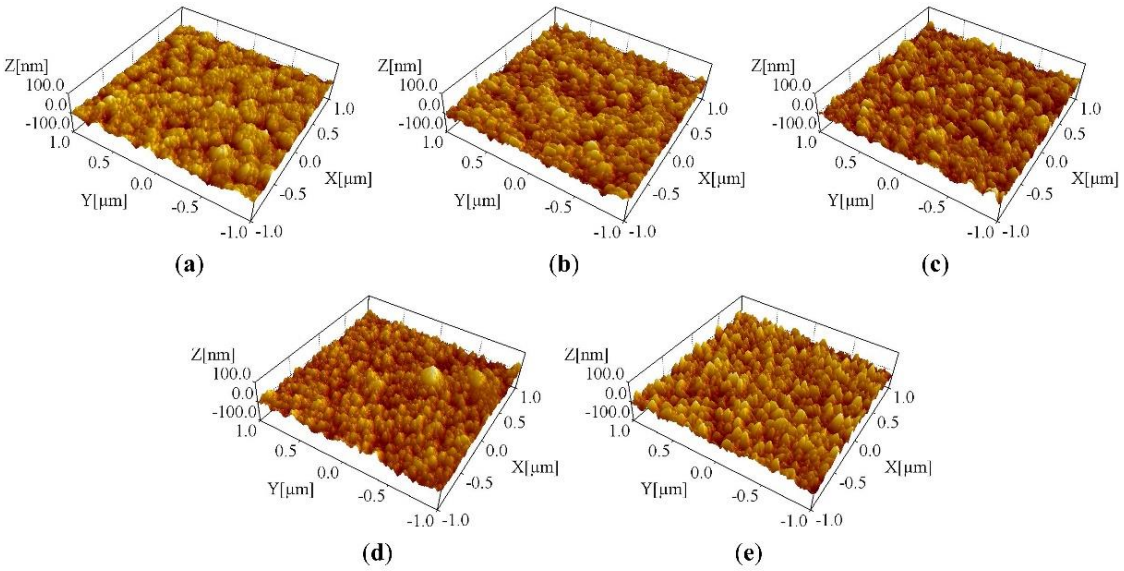

Fig. 4.2 AFM images of TiO_2 films deposited with different thicknesses by mist CVD method. ((**a**) 100 nm; (**b**) 200 nm; (**c**) 300 nm; (**d**) 400 nm; (**e**) 500 nm).

Table 4.3 Surface roughness and surface area of TiO_2 films with different thicknesses.

Film thickness (nm)	Surface roughness (nm)	Surface area (μm^2)
100	8.22	4.43
200	11.2	5.29
300	11.7	5.21
400	12.1	5.25
500	15.0	5.67

The GIXRD patterns of TiO_2 films with different thicknesses deposited by mist CVD are shown in Fig. 4.3. The observed peaks are corresponding to the diffractions from (101), (004), (105), (211), (204), and (215) surface of the anatase phase of TiO_2. With the thickness of TiO_2 film increasing from 100 nm to 300 nm, the (101) peak was dominant. When the thickness of TiO_2 film increasing from 300 nm to 500 nm, the intensity of (004) peak was enhanced significantly, and both (101) peak and (004) peak became dominant. This result indicated the growth of {001} facets was enhanced.

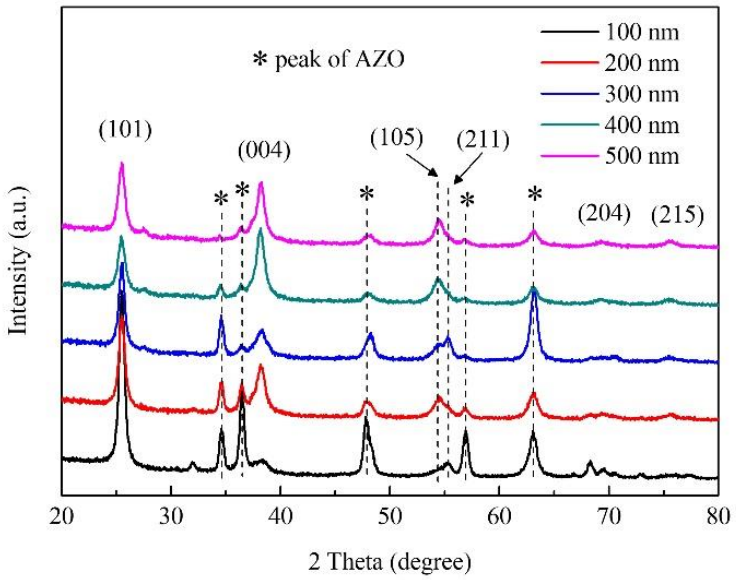

Fig. 4.3 GIXRD patterns of TiO_2 films with different thicknesses deposited by mist CVD.

Figure 4.4 shows the Raman spectra of TiO_2 films with different thicknesses deposited by mist CVD. Three peaks are observed in the Raman spectra. The peaks at 396 cm^{-1} and 634 cm^{-1} are corresponding to the B_{1g} mode and E_g mode of anatase phase TiO_2 respectively. The peak at 514

cm^{-1} is a doublet of the A_{1g} and B_{1g} modes of the anatase phase TiO_2. No peaks of the rutile or brookite phase TiO_2 are observed in the Raman spectra. It indicates the TiO_2 films are pure anatase phase, which is consistent with the GIXRD result. With the thickness of film increasing from 100 nm to 500 nm, the intensity of all Raman peaks showed a trend of increase, which indicates that the crystallinity of TiO_2 films increased gradually.

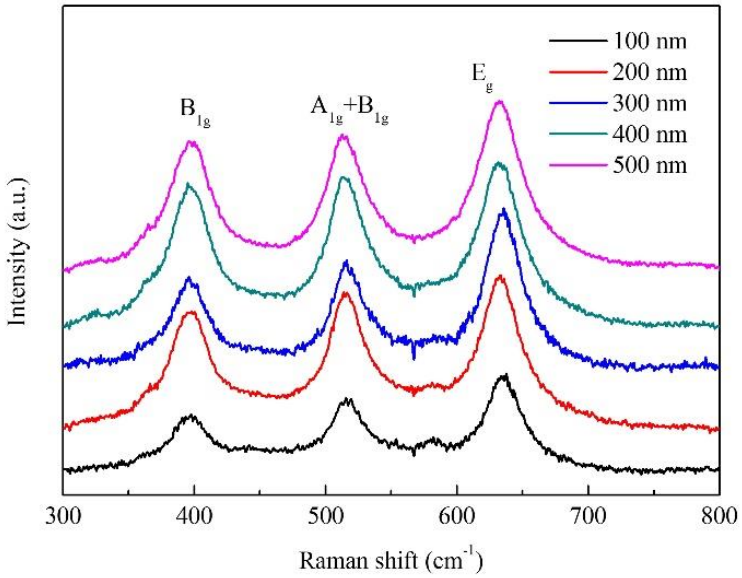

Fig. 4.4 Raman spectra of TiO_2 films with different thicknesses deposited by mist CVD.

The transmission spectra of TiO_2 films with different thicknesses deposited by mist CVD is shown in Fig. 4.5. With the thickness of film increasing from 100 nm to 500 nm, the transmittance of TiO_2 films in the visible region decreased from around 80 % to around 65 % gradually. These changes of the transmittance could be attributed to the change of film surface roughness. With the increasing of surface roughness, the scattering of light was enhanced, which decreased the transmittance of TiO_2 films. Due to the relative high surface roughness, the transmittance of TiO_2 films deposited with a thickness of 500 nm was lower than other samples.

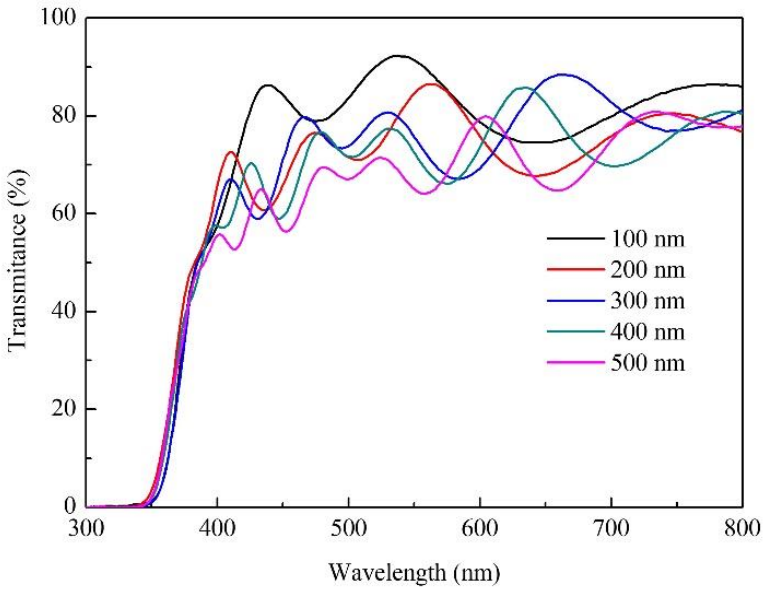

Fig. 4.5 Transmittance of TiO_2 films deposited with different thicknesses by mist CVD.

4.2.3 Summary

Pure anatase phase TiO_2 films with different thicknesses were fabricated with methanol as solvent by mist CVD. The effects of film thickness on the properties of TiO_2 films were investigated. Uniform TiO_2 films with different thicknesses were obtained. With the thickness increasing, the roughness and surface area of TiO_2 film showed tendency of increase. The crystallinity of TiO_2 films increases with the increasing of film thickness. With the thickness increasing, the transmittance of TiO_2 films decreased from around 80 % to around 65 % gradually.

4.3 Effects of water to methanol ratio on the properties of TiO_2 thin films

4.3.1 Experimental

The deposition condition is shown in Table 4.4. The precursor solution was prepared by dissolving acetylacetone and TTIP in water and methanol. In order to investigate the effect of water-to-methanol ratio on structural, optical and photocatalytic properties of TiO_2 films, the water-to-methanol volume ratio was set as 0 %, 1 %, 5 %, 10 % and 20 % for comparison. The TiO_2 films of 300 nm thickness were deposited on glass substrates (EAGLE XG, Corning).

Table 4.4 Deposition condition of water-to-methanol ratio dependence.

Substrate	Glass
Solute	TTIP, Acetylacetone
Solvent	Water, Methanol
Concentration of TTIP (mol/L)	0.02
Concentration of acetylacetone (mol/L)	0.06
Water-to-methanol ratio (%)	0, 1, 5, 10, 20
Deposition Temperature (℃)	400
Carrier Gas, Flow Rate (L/min)	N_2, 2.5
Dilution Gas, Flow Rate (L/min)	N_2, 4.5

The measurement of photocatalytic effect was carried out by photodegrading a methyl red (MR) solution under UV light of 254 nm for 5 hours. The concentration and volume of the MR solution was 1×10^{-5} mol/L and 70 ml. The size of the anatase TiO_2 sample was 3×3 cm^2. The photon flux of the UV light was 1.11×10^{-3} W/cm^2. After the photodegradation, the absorption spectra of MR solution were measured by spectrophotometer (U-4100, Hitachi). All of the measurements were carried out at room temperature.

4.3.2 Results and discussion

The SEM images of TiO_2 films deposited under different water-to-methanol ratio by mist CVD are displayed in Fig. 4.6. The TiO_2 films deposited as a function of different water-to-methanol ratios showed good uniformity. When the water-to-methanol ratio decreased from 20 % to 0 %, the average grain size of TiO_2 films increased.

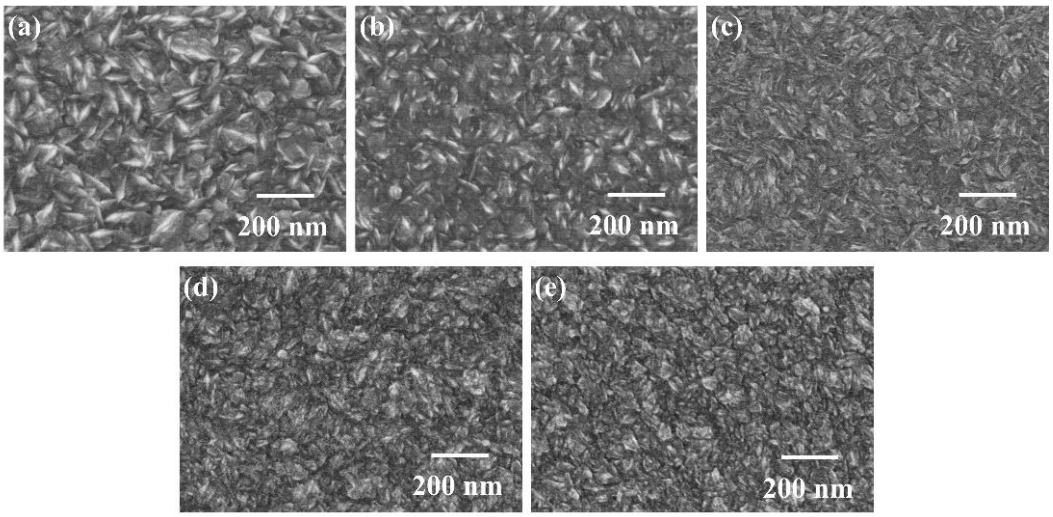

Fig. 4.6 SEM images of TiO_2 films deposited under different water-to-methanol ratio by mist CVD. ((**a**) 20 %; (**b**) 10 %; (**c**) 5 %; (**d**) 1 %; (**e**) 0 %).

Figure 4.7 shows the AFM images of TiO_2 films deposited under different water-to-methanol ratios by mist CVD. As observed in the AFM images, the TiO_2 films deposited under different water-to-methanol ratios were flat and uniform, which agreed well with the SEM results. The RMS values of the surface roughness and surface area were obtained from the AFM data (the scan area is 2 × 2 μm^2) and summarized in Table 4.5. The measurements of surface roughness and surface area were conducted several times, and the results are reproducible. The roughness of TiO_2 films changed only slightly as the water-to-methanol ratio decreased from 20 % to 5 %. The surface roughness of TiO_2 films increased roughly twice from 5.49 nm to 10.20 nm when the water-to-methanol ratio decreased from 5 % to 0 %. The surface area of TiO_2 films showed the same variation tendency as the surface roughness with a decrease in water-to-methanol ratio. The highest surface roughness and surface area of TiO_2 films were obtained with a water-to-methanol of 0 %. The lowest surface roughness and surface area of TiO_2 films were obtained with a water-to-methanol of 5 %.

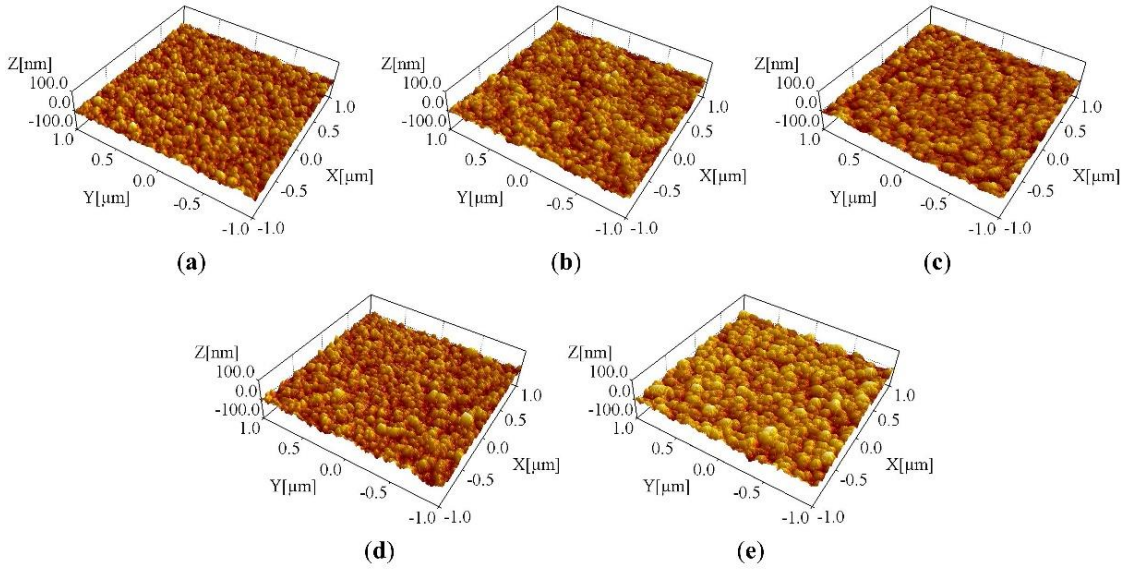

Fig. 4.7 AFM images of TiO_2 films deposited under different water-to-methanol ratio by mist CVD. ((**a**) 20 %; (**b**) 10 %; (**c**) 5 %; (**d**) 1 %; (**e**) 0 %).

The GIXRD patterns of all TiO_2 films deposited under different water-to-methanol ratios are shown in Fig. 4.8a. The observed peaks were indexed to the diffractions from (101), (004), (112), (200), (105), (211), (201), (204), and (215) surfaces of the anatase phase of TiO_2. All of the diffraction peaks were identified and corresponding to the anatase phase of TiO_2 (JCPDS 21-1272). This result suggested pure anatase phase TiO_2 films were successfully obtained for every water-to-methanol ratio investigated. As shown in Fig. 4.8b, when the water-to-methanol ratio decreased from 20 % to 0 %, the intensity of the (004) diffraction peak increased gradually while the intensity of the (101) diffraction peak decreased simultaneously. As a result, the intensity ratio of the (004) peak to (101) peak increased gradually. It was confirmed from the GIXRD results that the amount of {001} and {101} facets could be modulated and controlled by changing the water-to-methanol ratio.

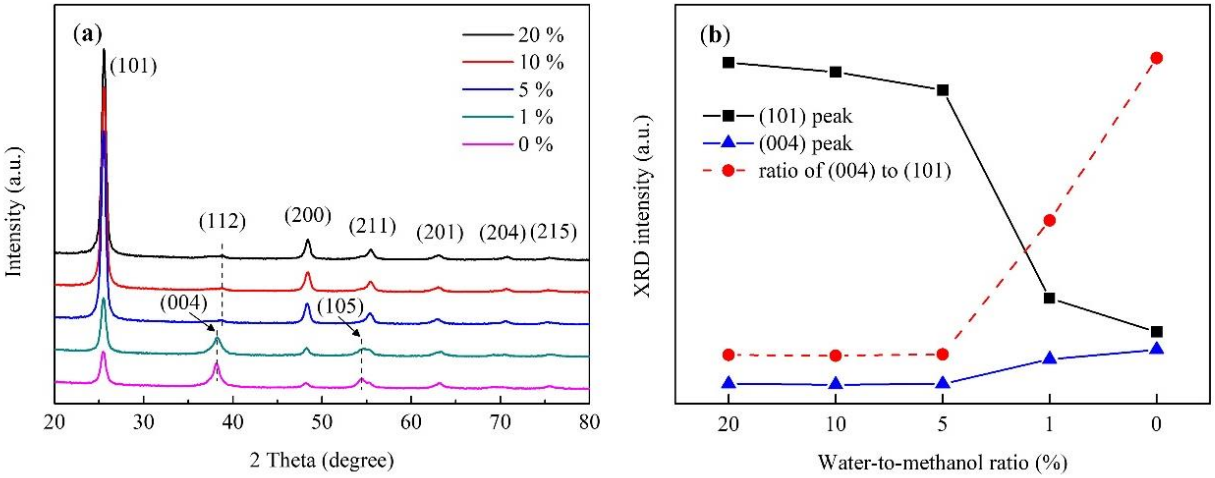

Fig. 4.8 GIXRD results of TiO_2 films deposited under different water-to-methanol ratio by mist CVD. ((**a**) GIXRD patterns of TiO_2 films; (**b**) GIXRD intensity of TiO_2 films).

Table 4.5 Surface roughness and surface area of glass and TiO_2 films

	Water-to-methanol ratio (%)	Surface roughness (nm)	Surface area (μm^2)
Glass	-	0.31	4.01
	20	5.77	4.39
	10	6.15	4.46
TiO_2 films	5	5.49	4.38
	1	8.88	5.04
	0	10.20	5.19

The Raman spectra of TiO_2 films deposited under different water-to-methanol ratios is shown in Fig. 4.9. Three peaks were observed in the Raman spectra of TiO_2 films. The peaks at 396 cm^{-1} and 634 cm^{-1} are corresponding to the B_{1g} mode and E_g mode of anatase phase TiO_2 respectively. The peak at 514 cm^{-1} is a doublet of the A_{1g} and B_{1g} modes of the anatase phase TiO_2. There were no peaks of the rutile or brookite phase TiO_2 observed in the Raman spectra, which indicated the obtained TiO_2 films were pure anatase phase. This result was in a good agreement with the GIXRD result. Compared with other samples, the E_g peak of TiO_2 film deposited with a water-to-methanol ratio of 0 % showed a slight shift, which could be attributed to the change of crystallite size [27,28].

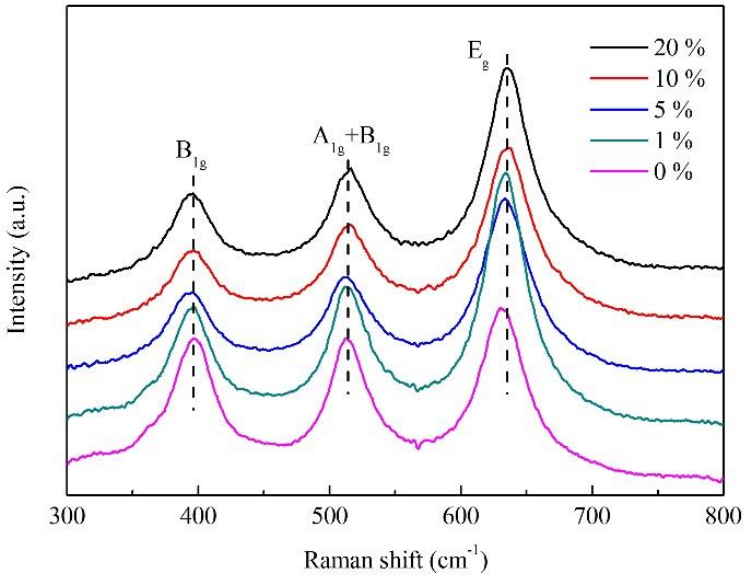

Fig. 4.9 Raman spectra of TiO_2 films deposited under different water-to-methanol ratio by mist CVD.

Figure 4.10 shows the transmission spectra of TiO_2 films deposited under different water-to-methanol ratios by mist CVD. With the water-to-methanol ratio decreasing from 20 % to 10 %, the transmittance of TiO_2 films was similar and higher than 75 % in the visible region. As the water-to-methanol ratio decreased from 10 % to 0 %, the transmittance of TiO_2 films showed a slightly decreasing tendency in the visible region. These changes of the transmittance could be attributed to the change of film surface roughness. With the increasing of surface roughness, the scattering of light was enhanced, which decreased the transmittance of TiO_2 films. Due to the relative high surface roughness, the transmittance of TiO_2 films deposited with water-to-methanol ratios of 1 % and 0 % was lower than other samples and their transmission spectra showed a slight shift.

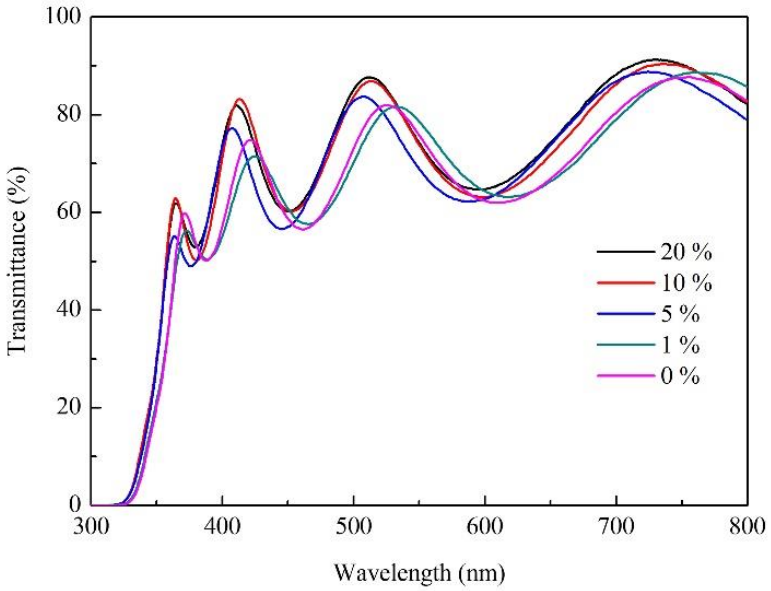

Fig. 4.10 Transmittance of TiO_2 films deposited under different water-to-methanol ratio by mist CVD.

Figure 4.11 shows the photocatalytic degradation result of MR with TiO_2 films deposited under different water-to-methanol ratios. As shown in the absorption spectra of the MR solution in Fig. 4.11a, the maximum absorption was observed at 520 nm. Compared with the original virgin MR solution, the absorption was decreased following photodegradation. The concentration of virgin MR after photodegradation was shown in Fig. 4.11b, which was calculated by Lambert-Beer's law (Eq. (4.3)) [29].

$$A = Kbc \tag{4.3}$$

where A is absorbance; K is proportional constant; b is the optical pathlength of standard cell; c is the molar concentration of solution in the standard cell. The concentration of MR after photodegradation showed a tendency to decrease when the water-to-methanol ratio decreased from 20 % to 0 %, indicating the photocatalytic efficiency of TiO_2 film increased. The reason is that the number of {001} facets was increased by decreasing the water-to-methanol ratio. However, it was found that the photocatalytic efficiency of TiO_2 film obtained with a water-to-methanol of 5 % was lower than that of TiO_2 film obtained with a water-to-methanol of 10 %. This is attributed to the fact that the TiO_2 film obtained with a water-to-methanol of 5 % had a lower surface area than that obtained with a water-to-methanol of 10 %.

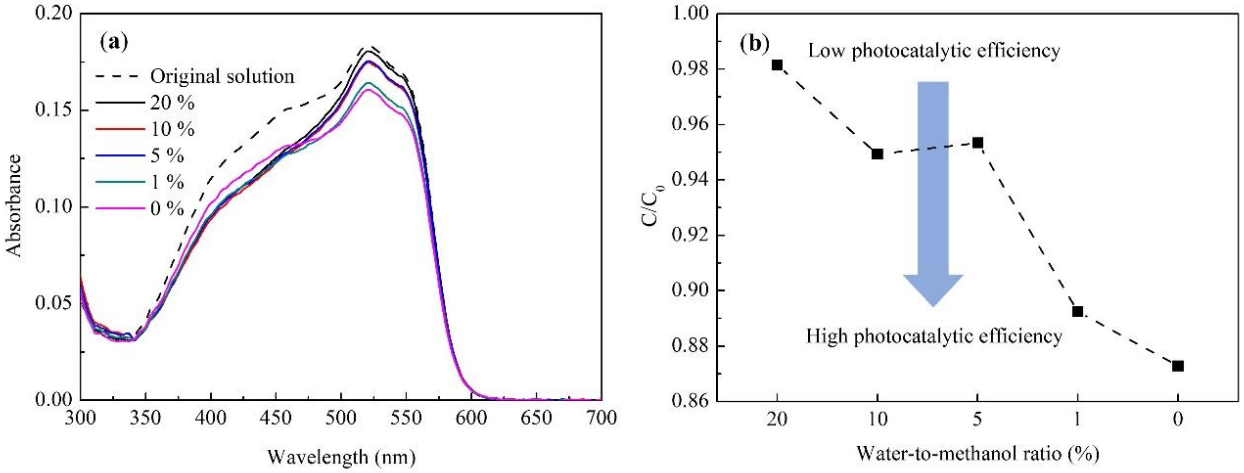

Fig. 4.11 The result of MR solution photodegradation by TiO_2 films deposited under different water-to-methanol ratio by mist CVD. ((**a**) absorption spectra of MR solution; (**b**) the concentration of MR solution after photodegradation).

4.3.3 Summary

Pure anatase phase TiO_2 films were fabricated with different water-to-methanol ratios by mist CVD. The effects of water-to-methanol ratio on the properties of TiO_2 films were investigated. During the deposition, the growth of {001} facets and surface area were significantly influenced by the water-to-methanol ratio. By decreasing the water-to-methanol ratio, the growth of {001} facets was enhanced, while the growth of {101} facets was suppressed. The surface roughness and surface area of TiO_2 films showed the same trend of increasing with a decrease of the water-to-methanol ratio. The highest surface roughness and maximized surface area was obtained with pure methanol as solvent. The transmittance of all TiO_2 films was higher than 70 % in the visible region. The photocatalytic efficiency of TiO_2 films showed an increasing trend with the decrease of the water-to-methanol ratio. The TiO_2 films deposited with pure methanol as solvent showed the highest photocatalytic efficiency due to a maximum number of {001} facets and an optimum surface area. These obtained TiO_2 films have high potential for photocatalyst applications.

4.4 Conclusions

In this chapter, pure anatase phase TiO_2 films were fabricated on AZO and glass substrates with methanol as solvent by mist CVD. The effects of film thickness and water-to-methanol ratio on the properties of TiO_2 films were revealed.

1) Uniform TiO_2 films with different thicknesses were obtained. With the thickness increasing, the roughness and surface area of TiO_2 film showed tendency of increase. The crystallinity of TiO_2 films increases with the increasing of film thickness. With the thickness increasing, the transmittance of TiO_2 films decreased from around 80 % to around 65 % gradually.

2) During the deposition, the growth of {001} facets and surface area were significantly influenced by the water-to-methanol ratio. By decreasing the water-to-methanol ratio, the growth of {001} facets was enhanced, while the growth of {101} facets was suppressed. The surface roughness and surface area of TiO_2 films showed the same trend of increasing with a decrease of the water-to-methanol ratio. The highest surface roughness and maximized surface area was obtained with a water-to-methanol of 0 %. The transmittance of all TiO_2 films was higher than 70 % in the visible region. The photocatalytic efficiency of TiO_2 films showed an increasing trend with the decrease of the water-to-methanol ratio. The TiO_2 films deposited with pure methanol as solvent showed the highest photocatalytic efficiency due to a maximum number of {001} facets and an optimum surface area, which has high potential for photocatalyst applications.

4.5 References

[1] M.V. Baryshnikova, L.A. Filatov, A.S. Petrov, S.E. Alexandrov. CVD deposited titania thin films for gas sensors with improved operating characteristics. Chem. Vap. Depos. 21 (2015) 327-333.

[2] T.-J. Ha, C.-S. Park, M.-H. Hong, H.-H. Park. Introduction of a pore connection network into mesoporous TiO_2 films to enhance CO gas sensitivity. J. Electrochem. Soc. 162 (2015) B180-B184.

[3] M. Epifani, A. Helwig, J. Arbiol, R. Díaz, L. Francioso, P. Siciliano, G. Mueller, J. R. Morante. TiO_2 thin films from titanium butoxide: synthesis, Pt addition, structural stability, microelectronic processing and gas-sensing properties. Sens. Actuators B Chem. 130 (2008) 599-608.

[4] E. Sennik, N. Kilinc, Z. Z. Ozturk. Electrical and VOC sensing properties of anatase and rutile TiO_2 nanotubes. J. Alloys Compd. 616 (2014) 89-96.

[5] B. Zhang, F. Wei, Q. Wu, L. Piao, M. Liu, Z. Jin. Formation and evolution of the high-surface-energy facets of anatase TiO_2. J. Phys. Chem. C 119 (2015) 6094-6100.

[6] D.-P. Song, M.-J. Chen, Y.-C. Liang, C.-Y. Wu, Z.-J. Xie, Q.-S. Bai. Molecular dynamics simulation study on surface structure and surface energy of anatase. Model. Simul. Mat. Sci. Eng. 18 (2010) 075002.

[7] M. Lazzeri, A. Vittadini, A. Selloni. Structure and energetics of stoichiometric TiO_2 anatase surfaces. Phys. Rev. B 63 (2001) 155409.

[8] M. Liu, L. Piao, L. Zhao, S. Ju, Z. Yan, T. He, C. Zhou, W. Wang. Anatase TiO_2 single crystals with exposed {001} and {110} facets: facile synthesis and enhanced photocatalysis. Chem. Commun. 46 (2010) 1664-1666.

[9] U. Diebold. The surface science of titanium dioxide. Surf. Sci. Rep. 48 (2003) 53-229.

[10] X.-Q. Gong, A. Selloni. Reactivity of anatase TiO_2 nanoparticles: the role of the minority (001) surface. J. Phys. Chem. B 109 (2005) 19560-19562.

[11] Y. Yang, Y. Liang, G. Wang, L. Liu, C. Yuan, T. Yu, Q. Li, F. Zeng, G. Gu. Enhanced gas-sensing properties of the hierarchical TiO_2 hollow microspheres with exposed high-energy {001} crystal facets. ACS Appl. Mater. Interfaces 7 (2015) 24902-24908.

[12] W. Zeng, T. Liu, Z. Wang, S. Tsukimoto, M. Saito, Y. Ikuhara. Oxygen adsorption on anatase TiO_2 (101) and (001) surfaces from first principles. Mater. Trans. 51 (2010) 171-175.

[13] C. Jin, B. Liu, Z. Lei, J. Sun. Structure and photoluminescence of the TiO_2 films grown by atomic layer deposition using tetrakis-dimethylamino titanium and ozone. Nanoscale Res. Lett. 10 (2015) 95-104.

[14] Y. Chimupala, G. Hyett, R. Simpson, R. Mitchell, R. Douthwaite, S. J. Milne, R. D. Brydson. Synthesis and characterization of mixed phase anatase TiO_2 and sodium-doped TiO_2 (B) thin films by low pressure chemical vapour deposition (LPCVD). RSC Adv. 4 (2014) 48507-48515.

[15] L. Romero, A.B. Jorge, P.F. McMillan, R. Binions. Enhanced photocatalytic properties of titanium dioxide thin films produced from the ac electric field assisted chemical vapor deposition of titanium (IV) chloride in toluene. ECS J. Solid State Sci. Technol. 3 (2014) N107-N113.

[16] K.H. Choi, K.B. Chung, H.K. Kim. d-orbital ordering of oxygen-deficient amorphous and anatase TiO_{2-x} channels for high mobility thin film transistors. Appl. Phys. Lett. 102 (2013) 153511.

[17] R.A. Fisher, M.R. Watt, R. Konjeti, W.J. Ready. Atomic layer deposition of titanium oxide for pseudocapacitive functionalization of vertically-aligned carbon nanotube supercapacitor electrodes. ECS J. Solid State Sci. Technol. 4 (2015) M1-M5.

[18] B. Comert, N. Akin, M. Donmez, S. Saglam, S. Ozcelik. Titanium dioxide thin films as methane gas sensors. IEEE Sens. J. 16 (2016) 8890-8996.

[19] H. Yoon, B. Joshi, S.-H. Na, S.S. Yoon. Antibacterial activity and photocatalysis of electrosprayed titania films. J. Electrochem. Soc. 159 (2012) H823-H827.

[20] P. Buerger, D. Nurkowski, J. Akroyd, S. Mosbach, M. Kraft. First-principles thermochemistry for the thermal decomposition of titanium tetraisopropoxide. J. Phys. Chem. A 119 (2015) 8376-8378.

[21] Y. Jang, B. Yang, J. Shin, J. An. Ultraviolet light-induced wettability control of ultrathin atomic layer deposited TiO_2 film surface. Thin Solid Films 642 (2017) 151-156.

[22] K. Vibulyaseak, S. Bureekaew, M. Ogawa. Size-controlled synthesis of anatase in a mesoporous silica, SBA-15. Langmuir 33 (2017) 13598-13603.

[23] W. Li, L. Li, X. Wu, J. Li, L. Jiang, H. Yang, G. Ke, G. Cao, B. Deng, W. Xu. High infrared blocking cellulose film based on amorphous to anatase transition of TiO_2 via atomic layer deposition. ACS Appl. Mater. Interfaces 10 (2018) 21056-21060.

[24] H. Choi, J. Shin, C. Shin. Impact of source/drain metal work function on the electrical characteristics of anatase TiO_2-based thin film transistors. ECS J. Solid State Sci. Technol. 6 (2017) P379-P382.

[25] E.H. Kim, M.H. Lim, M.S. Lah, S.M. Koo. Synthesis and characterization of heteroleptic titanium MOCVD precursors for TiO_2 thin films. Dalton Trans. 47 (2018) 2415-2421.

[26] C. Edusi, G. Sankar, I.P. Parkin. The effect of solvent on the phase of titanium dioxide deposited by aerosol-assisted CVD. Chem. Vap. Depos. 18 (2012) 126-132.

[27] W.F. Zhang, Y.L. He, M.S. Zhang, Z. Yin, Q. Chen. Raman scattering study on anatase TiO_2 nanocrystals. J. Phys. D: Appl. Phys. 33 (2000) 912-916.

[28] X. Xue, W. Ji, Z. Mao, H. Mao, Y. Wang, X. Wang, W. Ruan, B. Zhao, J.R. Lombardi. Raman investigation of nanosized TiO_2: effect of crystallite size and quantum confinement. J. Phys. Chem. C 116 (2012) 8792-8797.

[29] X. Wu, Z. Zhang, C. Xia, B. Chen, X. Jin, Z. Huang, Y.-G. Liu, M. Fang, X. Min. Magnetically recoverable Ni@C composites: The synthesis by carbonization and adsorption for Fe^{3+}. J. Alloys Compd. 718 (2017) 15-21.

Chapter 5

Fabrication and characterization of ZnO nanorods and ZnO-TiO_2 core-shell nanorods by chemical bath deposition and mist CVD method

5.1 Introduction

Thin film sensors have been widely investigated in various fields. Compared with traditional sensor materials, thin-film sensors have attracted considerable interest since they are easy for realizing the integration and miniaturization in structure, as well as, higher sensitivity and shorter response time than traditional sensors [1-3].

In chapter 3 and chapter 4, pure anatase TiO_2 thin films with good uniformity and crystallinity were successfully synthesized by by mist CVD. However, it was difficult to increase the surface area of obtained TiO_2 films significantly by changing the deposition parameters. In order to solve this problem, one solution is to fabricate a core-shell structure by coating a TiO_2 shell onto ZnO nanostructure.

Compared with TiO_2, ZnO is much easier to fabricate into various nanostructures. Previous studies reported ZnO nanorods could be coated with TiO_2 layer by solution method, sol-gel method and atomic layer deposition [4-6]. However, the phase controlling, thickness controlling and poor uniformity of TiO_2 layer are still unsolved issues. Compared with other reported methods, the mist CVD [7] was proven to be an effective method to synthesize pure anatase phase TiO_2 thin films according to our previous research [8,9].

ZnO nanostructures could be fabricated via various methods including vapor-liquid-solid process, pulse laser deposition, chemical vapor deposition, electrochemical, hydrothermal method and chemical bath deposition [10-14]. However, some of these methods require expensive equipment, high temperature and high vacuum conditions. Comparing with those methods required for expensive experimental conditions, chemical bath deposition (CBD) method supplies a simple procedure to synthesis nanostructures at low temperature. It was reported that ZnO nanostructures were fabricated by CBD method with optimized experimental conditions such as temperature, growing time and concentrations [15-17]. In our previous research, well-arrayed ZnO nanorods were successfully fabricated by CBD method [18-20]. In addition, we developed

a novel technique using novel multi-annealing process to successfully obtained ZnO nanostructures [21,22].

In this chapter, in order to obtain the ZnO nanostructures with large surface area and excellent chemical stability, the well-aligned ZnO nanorods were be fabricated by CBD method. Then, the fabricated ZnO nanorods were coated with TiO_2 film by mist CVD method. The obtained ZnO-TiO_2 core-shell nanorods are expected to have larger surface area to enhance their sensing property for applying in gas sensors.

5.2 Effects of solution concentration on the properties of ZnO nanorods

5.2.1 Experimental

AZO (2 wt. %) thin films with 300nm thickness were deposited on alkali-free glass sheets (Eagle XG, Corning Inc., Corning, NY, USA) by a conventional 13.56 MHz RF magnetron sputtering system. The deposition condition of AZO film was the same as Table 4.1 in section 4.2. Following the deposition of AZO films, ZnO nanorods were fabricated on AZO substrates by CBD. During the CBD process, the substrates were immersed in a solution containing $Zn(NO_3)_2$ and hexamethylenetetramine ($C_6H_{12}N_4$, HMTA) for 5 hours at 95 °C. The deposition condition of ZnO nanorods is shown in Table 5.1.

Table 5.1 Deposition condition of ZnO nanorods with different solution concentration.

Solute	$Zn(NO_3)_2$, HMTA
Solvent	Ultrapure water
Concentration $Zn(NO_3)_2$ (mmol/L)	25, 20, 15, 10, 5
Concentration HMTA (mmol/L)	12.5, 10, 7.5, 5, 2.5
Concentration ratio of $Zn(NO_3)_2$ to NMTA	2:1
Deposition temperature (°C)	95
Deposition time (h)	5

5.2.2 Results and discussion

Figure 5.1 shows the SEM images of ZnO nanorods deposited with different solution concentrations. From the top view images, well-arrayed ZnO nanorods with hexagonal structure

were obtained with solution concentration decreasing from 100 % to 40 %. No ZnO nanorods were observed when the solution concentration decreased to 20 %. From the cross section view images, it was found that the ZnO nanorods grew vertically on AZO substrates and the average length of ZnO nanorods was around 600 nm. With the solution concentration decreasing from 100 % to 40 %, the density of ZnO nanorods decreased. With solution concentration decreasing from 40 % to 20 %, the hexagonal structure get worse.

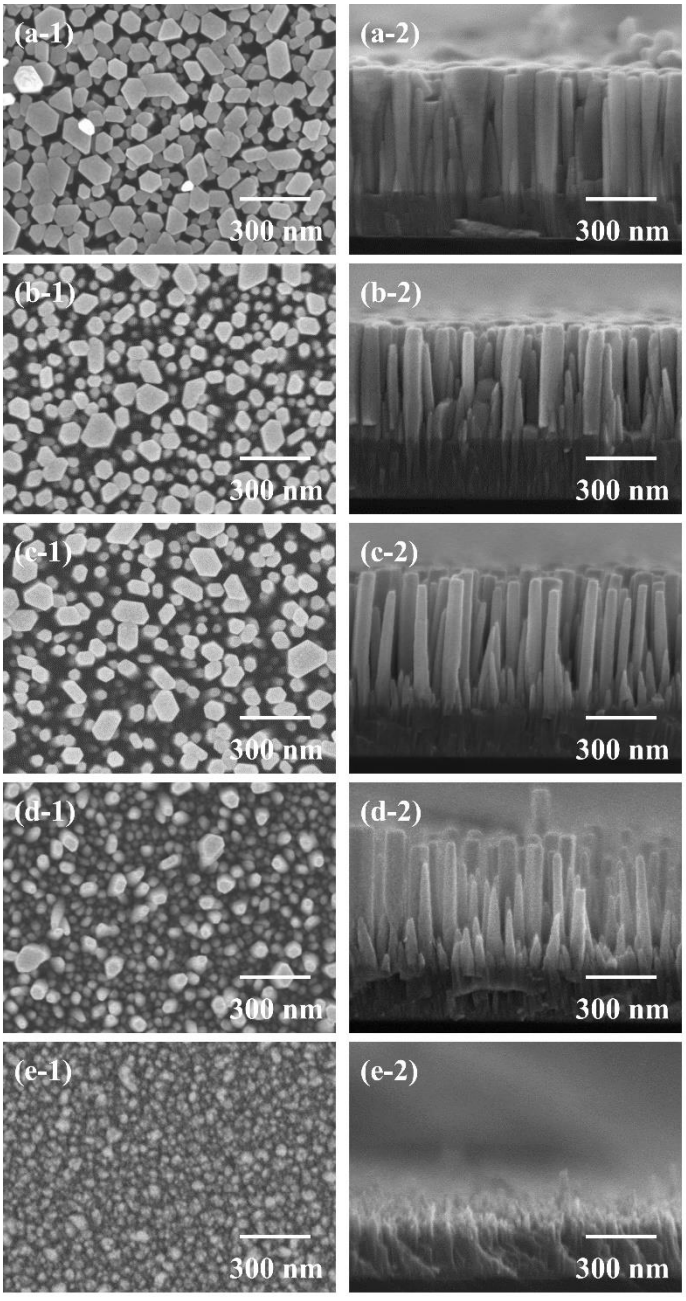

Fig. 5.1 SEM images of ZnO nanorods deposited with different solution concentrations. ((**a**) 100 %; (**b**) 80 %; (**c**) 60 %; (**d**) 40 %; (**e**) 20 %; (**1**) top view; (**2**) cross section view).

Figure 5.2a shows the XRD patterns of ZnO nanorods deposited with different solution concentrations. It was found that all XRD patterns of ZnO nanorods exhibited a dominant (002) diffraction peak, which indicated that the preferentially oriented growth was in the (0001) orientation and perpendicular to the substrate. This result agreed well with the SEM results.

The XRD intensity and FWHM of (002) diffraction peak are shown in Fig. 5.2b. With the solution concentration decreasing from 100 % to 20 %, the intensity of (002) peak showed a trend of decrease, and the FWHM of (002) peak showed a trend of increase. This indicated that the crystallinity of ZnO nanorods were getting worse with the decreasing of solution concentration. It was found that the highest intensity and narrowest FWHM of (002) peak were obtained with a solution concentration of 80 % , which suggested the best crystallinity of ZnO nanorods was obtained.

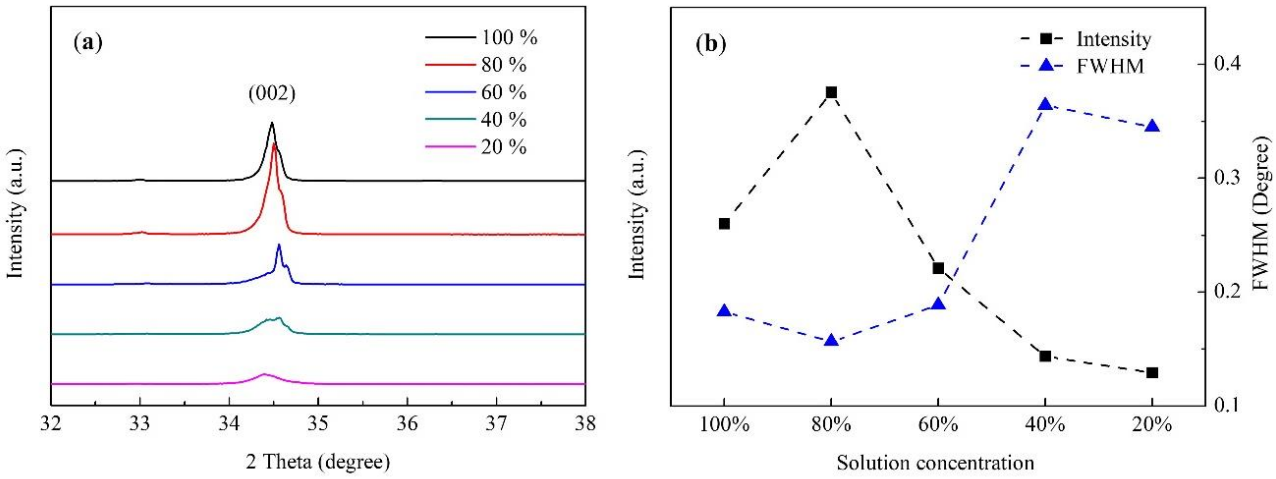

Fig. 5.2 XRD results of ZnO nanorods deposited with different solution concentrations.
((**a**) XRD patterns of ZnO nanorods; (**b**) intensity and FWHM of XRD peaks).

The transmission spectra of ZnO nanorods deposited with different solution concentrations is shown in Fig. 5.3. With the solution concentration decreasing from 100 % to 20 %, the transmittance of ZnO nanorods in the visible region increased from around 35 % to around 80 % gradually. This was attributed to the decreasing of ZnO nanorods density.

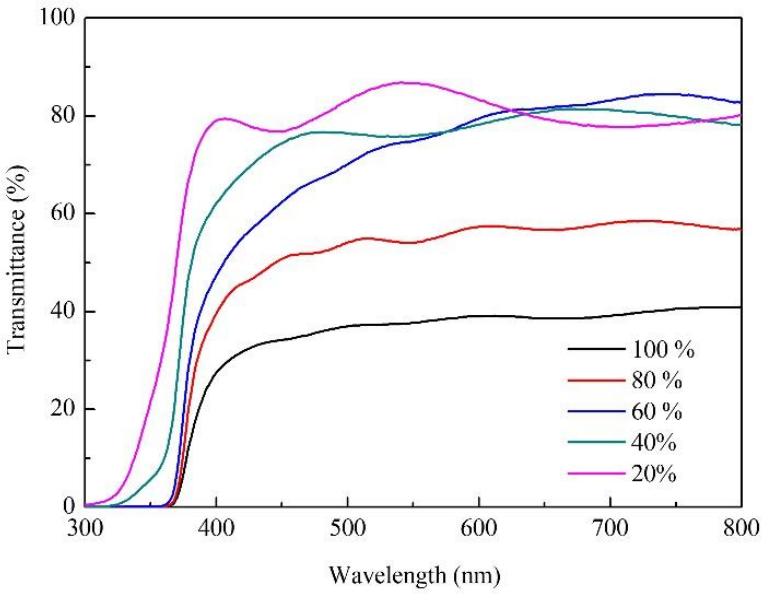

Fig. 5.3 Transmission spectra of ZnO nanorods deposited with different solution concentrations.

The PL spectra of ZnO nanorods deposited with different solution concentrations is shown in Fig. 5.4. It was found that the ZnO nanorods showed both a weak ultraviolet (UV) emission and a strong visible emission peak centered at 631 nm. The UV emission peak of as-deposited ZnO nanorods corresponded with the band gap of ZnO. The visible emission peak of ZnO nanorods could be attributed to oxygen vacancies and oxygen interstitials.

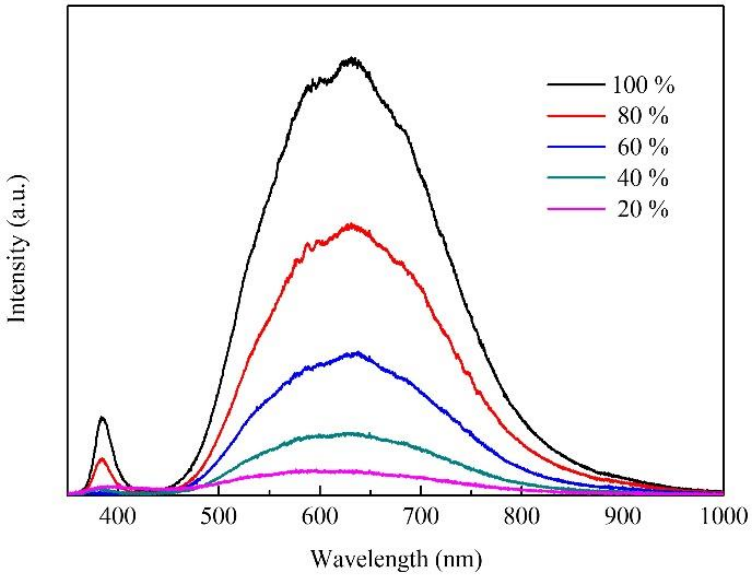

Fig. 5.4 PL spectra of ZnO nanorods deposited with different solution concentrations.

5.2.3 Summary

Well-arrayed ZnO nanorods were fabricated on AZO substrate by CBD method. The effects of solution concentration on the properties of ZnO nanorods were investigated. The solution concentration had a significant influence on the morphological, structural, and optical properties of ZnO nanorods. It was found that well-arrayed ZnO nanorods with hexagonal structure were obtained with solution concentration from 100 % to 40 %. With the decreasing of solution concentration, the crystallinity of ZnO nanorods showed a tendency of decrease, and the transmittance of ZnO nanorods increased gradually in visible range.

5.3 Effects of deposition time on the properties of ZnO nanorods

5.3.1 Experimental

AZO thin films with 300nm thickness were deposited on alkali-free glass sheets by RF magnetron sputtering system. The deposition condition of AZO film was the same as Table 4.1 in section 4.2. Following the deposition of AZO films, ZnO nanorods were fabricated on AZO substrates by CBD. During the CBD process, the substrates were immersed in a solution containing $Zn(NO_3)_2$ and HMTA for 5 hours at 95 °C. The deposition condition of ZnO nanorods is shown in Table 5.2.

Table 5.2 Deposition condition of ZnO nanorods with different deposition time.

Solute	$Zn(NO_3)_2$, HMTA
Solvent	Ultrapure water
Concentration $Zn(NO_3)_2$ (mmol/L)	15
Concentration HMTA (mmol/L)	7.5
Deposition temperature (℃)	95
Deposition time (h)	5, 10

5.3.2 Results and discussion

The SEM images of ZnO nanorods deposited with deposition time of 5 hours and 10 hours are shown in Fig. 5.5. From the top view images, well-arrayed ZnO nanorods with hexagonal

structure were obtained under different deposition time. The average diameter of ZnO nanorods increased when the deposition time increased from 5 hours to10 hours. From the cross section view SEM images, it was found that the ZnO nanorods deposited under different deposition time grew vertically on AZO substrates, and the length of ZnO nanorods deposited under 10 hours was almost twice as the length of that deposited under 5 hours.

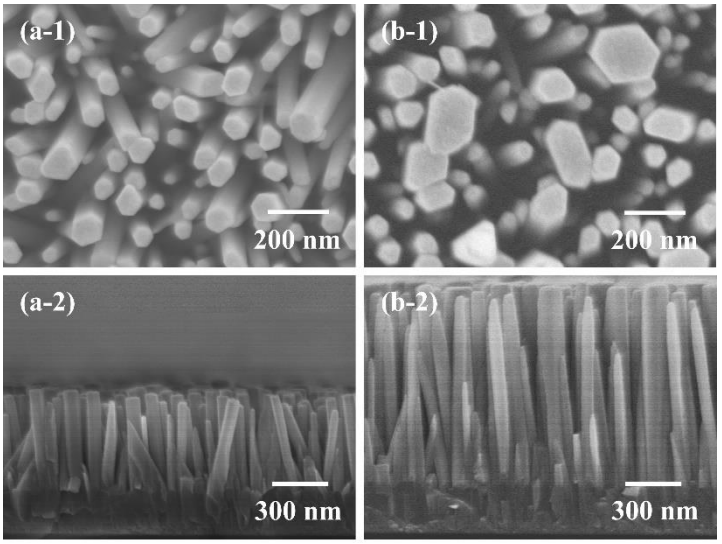

Fig. 5.5 SEM images of ZnO nanorods deposited with different time.
((**a**) 5 h; (**b**) 10 h; (**1**) top view; (**2**) cross section view).

The XRD patterns of ZnO nanorods deposited under 5 hours and 10 hours are shown in Fig. 5.6. In two of XRD patterns, only one strong diffraction peak was observed at 34.52° of 2 theta. This diffraction peak was identified as the (002) diffraction of ZnO. With the deposition time increased from 5 hours to 10 hours, the intensity of (002) diffraction peak increased significantly, which indicated the crystallinity of ZnO nanorods was enhanced with the growing time increasing.

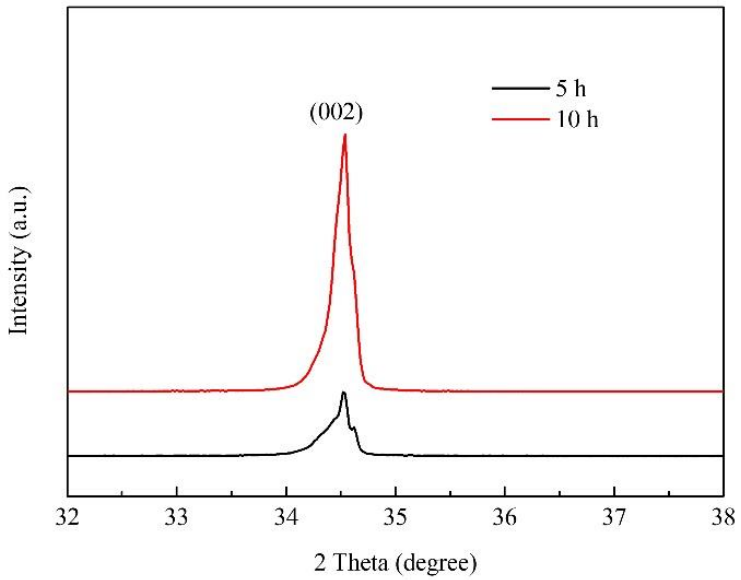

Fig. 5.6 XRD patterns of ZnO nanorods deposited with different time.

Figure 5.7 shows the transmission spectra of ZnO nanorods deposited under 5 hours and 10 hours. With the deposition time increasing from 5 hours to 10 hours, the transmittance of ZnO nanorods in the visible region decreased from around 75 % to around 35 %. This was attributed to the length increasing of ZnO nanorods.

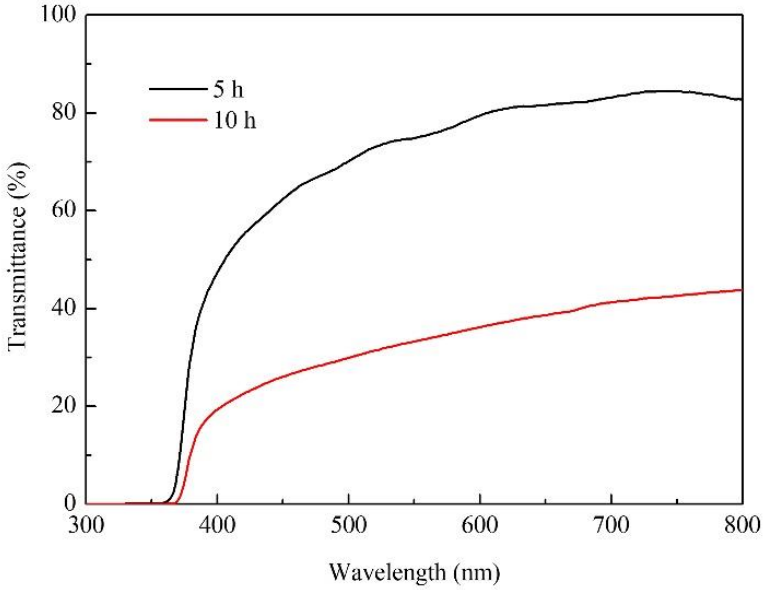

Fig. 5.7 Transmission spectra of ZnO nanorods deposited with different time.

5.3.3 Summary

Well-arrayed ZnO nanorods were fabricated on AZO substrate under different deposition time. The effects of deposition time on the properties of ZnO nanorods were investigated. The morphological, structural and optical properties of ZnO nanorods were significantly influenced by the deposition time. Well-arrayed ZnO nanorods with hexagonal structure were obtained with with deposition time of 5 hours and 10 hours. With the deposition time increasing from 5 hours to 10 hours, the crystallinity of ZnO nanorods increased significantly, and the transmittance of ZnO nanorods in the visible region decreased from around 75 % to around 35 %.

5.4 Fabrication and characterization of ZnO-TiO_2 core-shell nanorods

5.4.1 Experimental

AZO thin films with 300nm thickness were deposited on alkali-free glass sheets by RF magnetron sputtering system. The deposition condition of AZO film was the same as Table 4.1 in section 4.2. Following the deposition of AZO films, ZnO nanorods were fabricated on AZO substrates by CBD. During the CBD process, the substrates were immersed in a solution containing $Zn(NO_3)_2$ and HMTA for 5 hours at 95 °C. The deposition condition of ZnO nanorods is shown in Table 5.3. After the deposition, the obtained ZnO nanorods were coated with TiO_2 by mist CVD method. The deposition condition of coating is shown in Table 5.4.

Table 5.3 Deposition condition of ZnO nanorods.

Solute	$Zn(NO_3)_2$, HMTA
Solvent	Ultrapure water
Concentration $Zn(NO_3)_2$ (mmol/L)	15
Concentration HMTA (mmol/L)	7.5
Deposition temperature (°C)	95
Deposition time (h)	5

Table 5.4 Deposition condition of TiO_2 coating.

Solute	TTIP
Solvent	Ethanol
Concentration (mol/L)	0.10
Deposition temperature (˚C)	400
Carrier gas, flow rate (L/min)	Compressed air, 2.5
Dilution gas, flow rate (L/min)	Compressed air, 4.5
Coating time (min)	0.5, 2, 5, 10, 15

5.4.2 Results and discussion

As shown in Fig. 5.8, a schematic model is proposed to describe the mechanism of ZnO/TiO_2 core-shell nanorods fabrication. First, the ZnO nanorods were prepared on AZO film (acted as a seed layer) by CBD method. After the CBD process, the obtained ZnO nanorods were set in the reaction chamber of mist CVD. During the mist CVD process, the mist droplets—a mixture of TTIP and ethanol—were transformed from the solution of precursors by ultrasonic transducers. Following that, the mist droplets were transported onto the surface of ZnO nanorods by carrier and dilution gases. During the transportation of mist droplets in the reaction chamber, the size of mist droplets decreased from a few micrometers to a few nanometers with the effects of heat, evapotranspiration and burst. Finally, anatase phase TiO_2 particle shells were deposited on the surface of ZnO nanorods due to the pyrolysis reaction of TTIP at 400 °C [8].

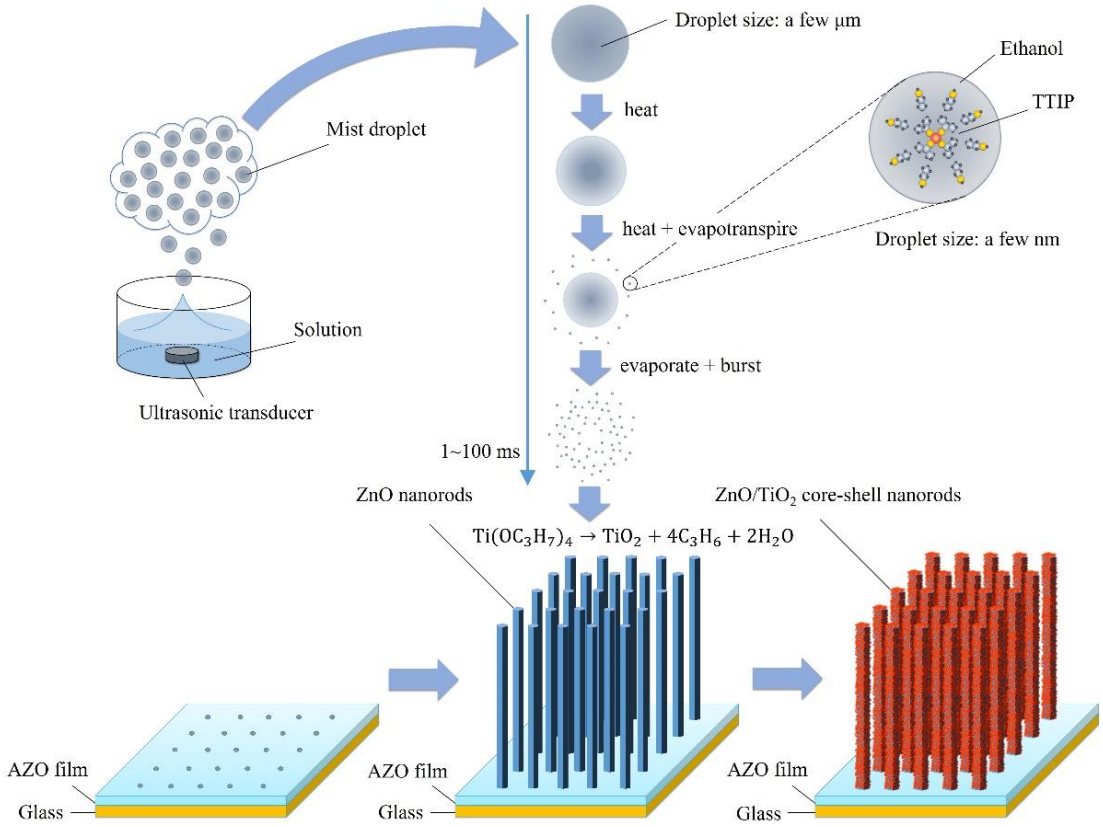

Fig. 5.8 Mechanism of ZnO/TiO_2 core-shell nanorods fabrication.

Figure 5.9 shows the SEM images of as-deposited ZnO nanorods and ZnO nanorods coated with TiO_2 by mist CVD. From the top view images, uniform ZnO nanorods with hexagonal structure were obtained on AZO substrate after CBD process. The inserted images in the top view images show the surface of a single ZnO nanorod. Compared with the as-deposited ZnO nanorods, it was difficult to observe the surface change of ZnO nanorods coated with TiO_2 for 30 seconds, 2 minutes and 5 minutes. When the TiO_2 coating time increased to 10 minutes and 15 minutes, TiO_2 particles were observed on the surface of ZnO nanorods. Compared with the relatively smooth surface of as-deposited ZnO nanorods, the ZnO nanorods coated TiO_2 for 15 minutes showed a rough surface with uniform TiO_2 particles, indicating that the surface area of nanorods had increased. From the cross section view images, it was found that the ZnO nanorods grew vertically on AZO substrates and the average length of ZnO nanorods was around 600 nm. The SEM results revealed that the TiO_2 particle layers on ZnO nanorods were uniform.

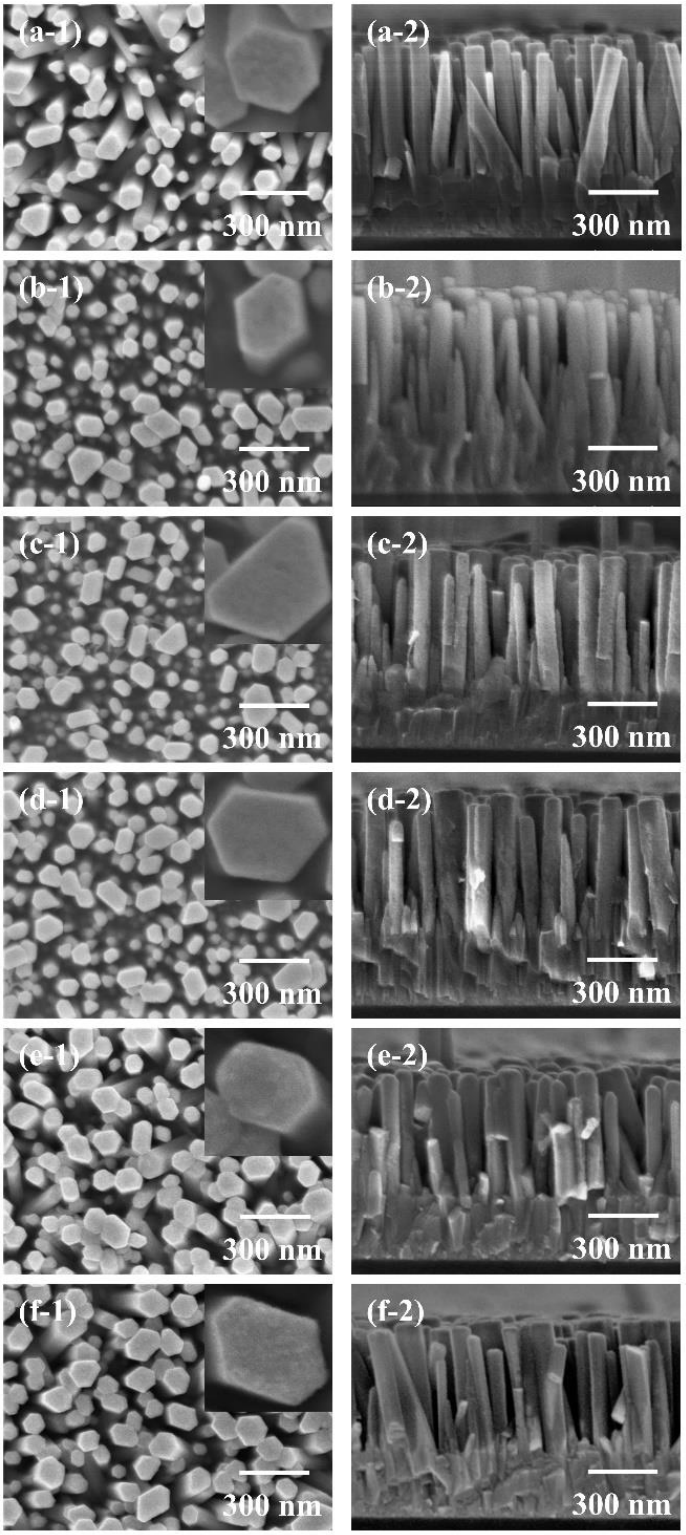

Fig. 5.9 SEM images of (**a**) as-deposited ZnO nanorods and ZnO nanorods coated with TiO_2 by mist CVD ((**b**) 30s; (**c**) 2 min; (**d**) 5min; (**e**) 10min; (**f**) 15 min; (**1**) top view; (**2**) cross section view).

The EDS elemental mapping images of ZnO nanorods coated with TiO_2 for 10 minutes are shown in Fig 5.10. The elemental mappings of zinc, titanium and oxygen are shown in Fig. 5.10b, Fig. 5.10c and Fig. 5.10d respectively. As shown in Fig. 5.10c, the titanium element was confirmed from the bottom to the top of ZnO nanorods, indicating that the whole surface of ZnO nanorods was successfully coated with TiO_2 particles. As the electron mobility and chemical stability are essential attributes of materials, this TiO_2 shell onto the whole surface of ZnO will significantly improve the chemical stability of ZnO nanorods and the electron mobility of TiO_2 thin films.

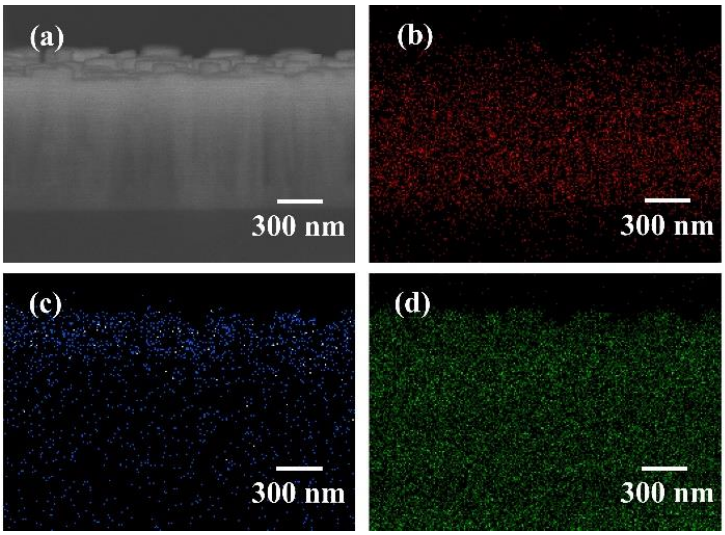

Fig. 5.10 The EDS elemental mapping images of ZnO nanorods coated with TiO_2 for 10 minutes ((**a**) FE-SEM image; (**b**) zinc element mapping image; (**c**) titanium element mapping image; (**d**) oxygen element mapping image).

Figure 5.11 shows the GIXRD patterns of as-deposited ZnO nanorods and ZnO nanorods coated with TiO_2 by mist CVD. The observed peaks corresponded with the diffractions from (100), (002), (101), (102), (110), (103), and (103) crystal planes of ZnO respectively. It was clear that the (103) peaks were the dominant peaks, which was due to the low incidence angle (0.35 °) employed in GIXRD. After coating TiO_2 for 30 seconds and 2 minutes, the intensity of ZnO peaks between 30 ° and 40 ° decreased, which suggested the growth of TiO_2 on the surface of ZnO nanorods. When the TiO_2 coating time increased from 2 minutes to 15 minutes, the intensity of these ZnO peaks showed a trend of increase. This could be attributed to the annealing effects during mist CVD process, which was operated at 400 ˚C. The inserted image showed the detail of GIXRD patterns from 20 ° to 30 °. There was no peak of TiO_2 observed from the ZnO nanorods

coated with TiO_2 for 30 seconds, 2 minutes and 5 minutes, which might be due to the insufficient thickness of TiO_2 layer. A (101) diffraction peak, which corresponded with anatase phase TiO_2, was observed at 2 theta of 25.3 ° when the TiO_2 coating time was increased to 10 minutes and 15 minutes. The intensity of the TiO_2 (101) diffraction peak increased as the TiO_2 coating time increased, which indicated the thickness of TiO_2 layer had increased.

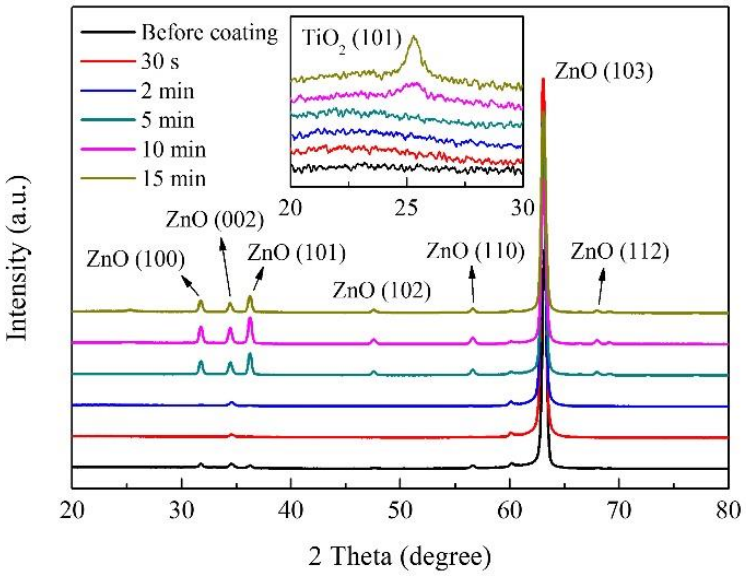

Fig. 5.11 GIXRD patterns of as-deposited ZnO nanorods and ZnO nanorods coated with TiO_2 by mist CVD.

Figure 5.12 shows the Raman spectra of as-deposited ZnO nanorods and ZnO nanorods coated with TiO_2 by mist CVD. The Raman peaks at 438 cm^{-1} and 582 cm^{-1} were assigned to the E_{2h} mode and E_1 (LO) mode of ZnO respectively. Three more peaks were observed in the Raman spectrum of ZnO nanorods coated with TiO_2 under 15 minutes. The peaks at 398 cm^{-1}, 639 cm^{-1} and 515 cm^{-1} corresponded with the B_{1g} mode, E_g mode and a doublet of the A_{1g} and B_{1g} modes of anatase phase TiO_2, which suggested that the ZnO nanorods were coated with TiO_2 successfully. This result agreed well with that from EDS and GIXRD measurements.

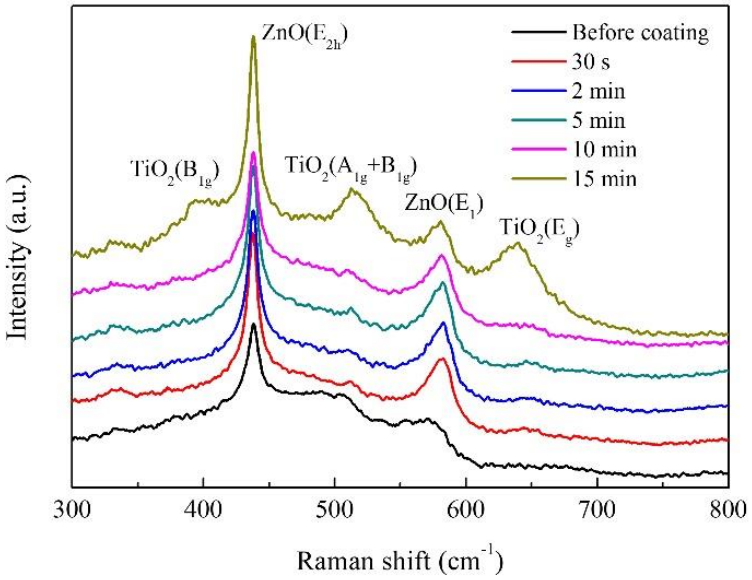

Fig. 5.12 Raman spectra of as-deposited ZnO nanorods and ZnO nanorods coated with TiO_2 by mist CVD.

The PL spectra of TiO_2 film on glass, as-deposited ZnO nanorods and ZnO nanorods coated with TiO_2 by mist CVD are shown in Fig. 5.13a. The inserted image shows the detail of PL spectra from 340 nm to 420 nm. It was found that the as-deposited ZnO nanorods showed a weak ultraviolet (UV) emission peak centered at 370 nm and a strong visible emission peak centered at 632 nm. The UV emission peak of as-deposited ZnO nanorods corresponded with the band gap of ZnO (around 3.37 eV). Compared with the as-deposited ZnO nanorods, the UV emission peak of the ZnO nanorods coated with TiO_2 for 30 seconds and 2 minutes showed a slight red shift. As the TiO_2 coating time increased from 2 minutes to 15 minutes, the UV emission red shifted gradually to 382 nm, which corresponded with the band gap of anatase phase TiO_2 (around 3.2 eV). It was found that PL emission peak of TiO_2 from 400 nm to 700 nm was not observed from the ZnO nanorods coated with TiO_2. This PL quenching of TiO_2 suggested the charge transfer from TiO_2 to ZnO.

According to the curve fitting for as-deposited ZnO nanorods visible emission, as shown in Fig. 5.13b, the visible emission peak of as-deposited ZnO nanorods was divided into four emission peaks (dashed line). The emission peaks of as-deposited ZnO nanorods located at 545 nm (~2.27 eV) and 614 nm (~2.02 eV) could be attributed to oxygen vacancies [23-26]. The emission peaks of as-deposited ZnO nanorods located at 689 nm (~1.80 eV) and 780 nm (~1.59 eV) could be attributed to oxygen interstitials [23]. It was observed that the visible emission of ZnO nanorods

showed a red shift after coated with TiO_2. After ZnO nanorods was coated with TiO_2 for 30 seconds, the peak intensity of the visible emission decreased steeply. As the TiO_2 coating time increased from 30 seconds to 15 minutes, the peak intensity of the visible emission first increased and then decreased. The highest visible emission peak intensity of ZnO/TiO_2 core-shell nanorods was obtained with a TiO_2 coating time of 10 minutes. The curve fitting of visible emission of ZnO nanorods coated TiO_2 for 10 minutes is shown in Fig. 5.13c. After curve fitting, the visible emission peak was divided into four emission peaks (dashed line). As the discussion of as-deposited ZnO nanorods above, the emission peaks located at 550 nm and 612 nm could be attributed to oxygen vacancies in ZnO nanorods, and the emission peak located at 685 nm could be attributed to oxygen interstitials. The broad emission peak centered at 812 nm (~1.53 eV) could be attributed to and oxygen interstitials in ZnO nanorods and titanium interstitials [27,28]. Based on the results of curve fitting, the red shift of ZnO nanorods visible emission was attributed to the intensity decrease of the emissions located at around 550 nm and around 612 nm, which was due to the annealing effects during mist CVD process.

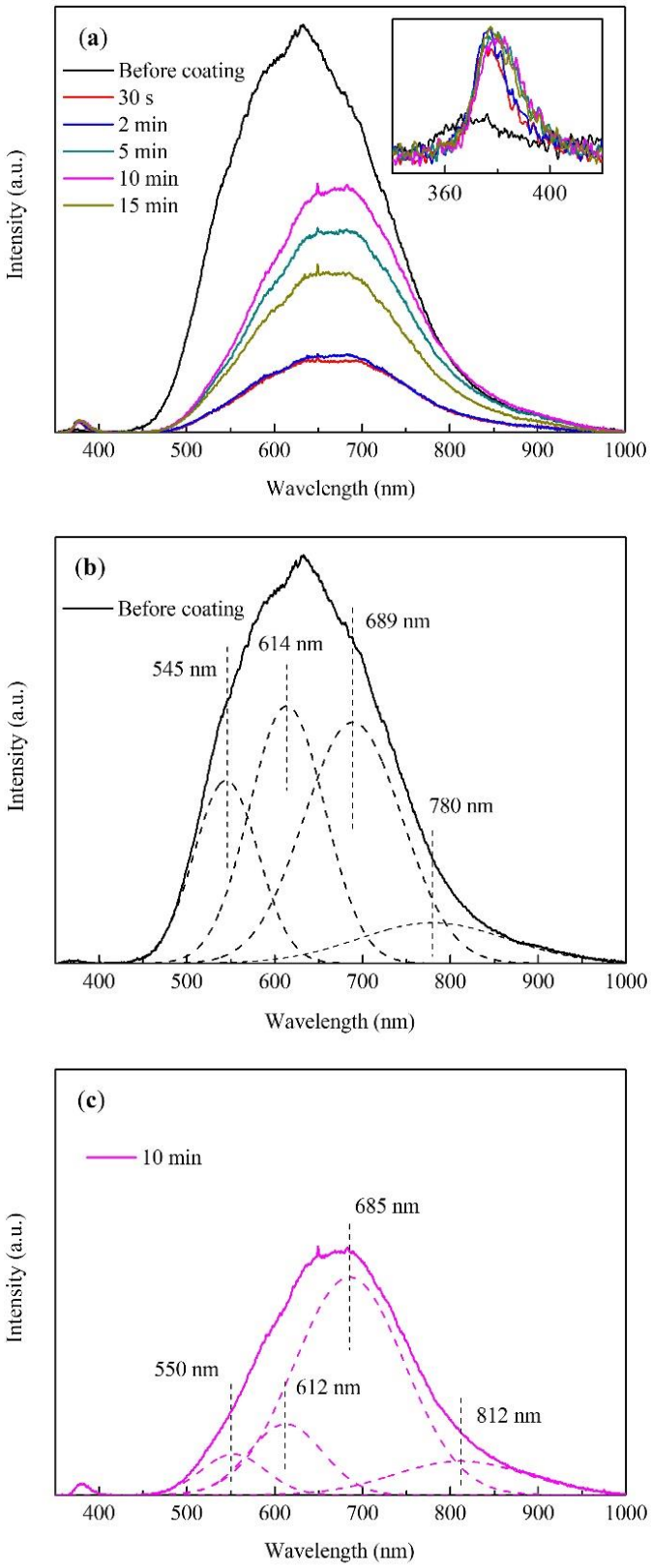

Fig. 5.13 (**a**) PL spectra of TiO_2 film on glass, as-deposited ZnO nanorods and ZnO nanorods coated with TiO_2 by mist CVD; (**b**) PL spectra curve fitting of as-deposited ZnO nanorods; (**c**) PL spectra curve fitting of ZnO nanorods coated with TiO_2 for 10 min.

It was proved by PL results that all of the defects in ZnO were decreased by coating TiO_2 onto ZnO. The oxygen interstitials in ZnO were decreased slightly after coating TiO_2. The oxygen vacancies in ZnO were significantly decreased due to the annealing effects during mist CVD process.

The transmission spectra of as-deposited ZnO nanorods and ZnO nanorods coated with TiO_2 by mist CVD is shown in Fig. 5.14a. The transmittance of as-deposited ZnO nanorods was around 75% in the visible region. The transmittance decreased to around 65 % gradually with the TiO_2 coating time increased from 30 seconds to 15 minutes.

The bandgap (E_g) of as-deposited ZnO nanorods and ZnO nanorods coated with TiO_2 could be obtained from the transmittance and absorbance of ZnO nanorods using the following equations [29]:

$$(\alpha h\nu)^2 = A(h\nu - E_g) \tag{5.1}$$

$$\alpha = \frac{1}{d}\ln\left(\frac{1}{T}\right) \tag{5.2}$$

where α is the absorption coefficient, hν the incidence photon energy, A a constant, d the film thickness, and T the transmittance. As shown in Fig. 5.14b, a plot of $(\alpha h\nu)^2$ as a function of hν was made to determine E_g by linear fitting. After fitting, the E_g of as-deposited ZnO nanorods was around 3.34 eV, which corresponded with the band gap of bulk ZnO (3.37 eV). The E_g of ZnO/TiO_2 core-shell nanorods was around 3.28 eV, which corresponded with the band gap of anatase phase TiO_2 (3.2 eV).

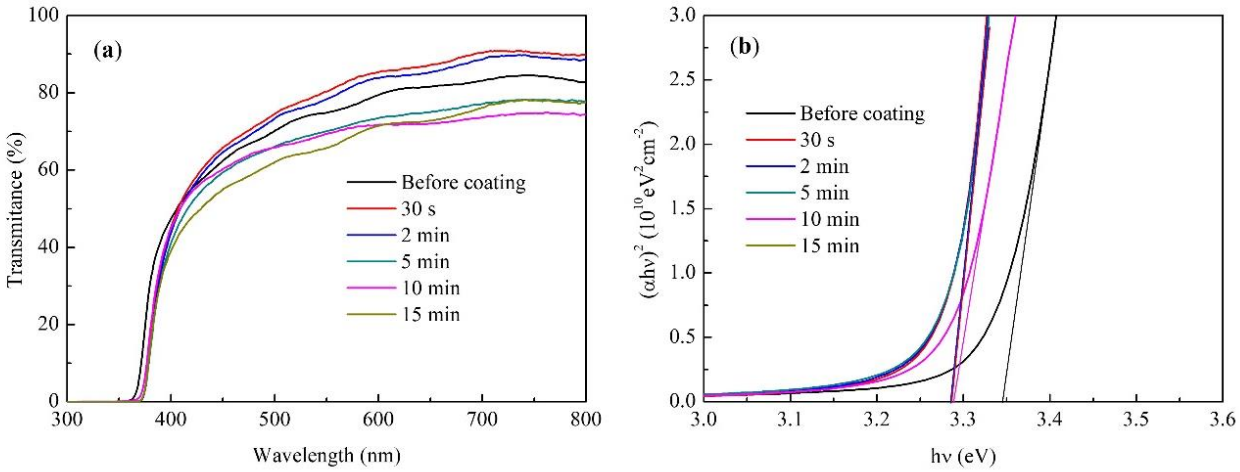

Fig. 5.14 (**a**) Transmission spectra of as-deposited ZnO nanorods and ZnO nanorods coated with TiO_2 by mist CVD; (**b**) Variation of $(ahv)^2$ of the as-deposited ZnO nanorods and ZnO nanorods coated with TiO_2 as a function of the photon energy (hν).

5.4.3 Summary

Well-arrayed ZnO/TiO_2 core-shell nanorods had been successfully fabricated on AZO substrate. It was found that mist CVD was a successful method for coating TiO_2 thin layers on the ZnO nanorods. The TiO_2 shells on ZnO nanorods were confirmed as pure anatase phase. The surface area of ZnO nanorods was significantly increased with increase in TiO_2 coating time. The transmittance of ZnO nanorods decreased from 75 % to 65 % after 15 minutes coating TiO_2. The well-arrayed ZnO/TiO_2 core-shell nanorods will contribute to a high surface-to-volume ratio and excellent chemical stability, which are expected to be applied as sensing material to improve the performance of gas sensors.

5.5 Conclusions

In this chapter, well-arrayed ZnO nanorods and well-arrayed ZnO/TiO_2 core-shell nanorods were fabricated on conductive AZO films. The effects of solution concentration and deposition time on the properties of ZnO nanorods were investigated. The effects of TiO_2 film coating time on the properties of ZnO/TiO_2 core-shell nanorods were investigated.

1) The solution concentration had a significant influence on the morphological, structural, and optical properties of ZnO nanorods. It was found that well-arrayed ZnO nanorods with hexagonal structure were obtained with solution concentration from 100 % to 40 %. With the decreasing of

solution concentration, the crystallinity of ZnO nanorods showed a tendency of decrease, and the transmittance of ZnO nanorods increased gradually in visible range.

2) The morphological, structural and optical properties of ZnO nanorods were significantly influenced by the deposition time. Well-arrayed ZnO nanorods with hexagonal structure were obtained with with deposition time of 5 hours and 10 hours. With the deposition time increasing from 5 hours to 10 hours, the crystallinity of ZnO nanorods increased significantly, and the transmittance of ZnO nanorods in the visible region decreased from around 75 % to around 35 %.

3) The TiO_2 shells on ZnO nanorods were confirmed as pure anatase phase, which will contribute to good gas sensitivity as sensing material. The surface area of ZnO nanorods was significantly increased with increase in TiO_2 coating time. The transmittance of ZnO nanorods decreased from 75 % to 65 % after 15 minutes coating TiO_2. The well-arrayed ZnO/TiO_2 core-shell nanorods will contribute to an excellent chemical stability, and relatively large surface-to-volume ratio for gas absorption, which are expected to be applied as sensing material to improve the performance of gas sensors.

5.6 References

[1] M.V. Baryshnikova, L.A. Filatov, A.S. Petrov, S.E. Alexandrov. CVD deposited titania thin films for gas sensors with improved operating characteristics. Chem. Vap. Depos. 21 (2015) 327-333.

[2] M. Epifani, A. Helwig, J. Arbiol, R. Díaz, L. Francioso, P. Siciliano, G. Mueller, J.R. Morante. TiO_2 thin films from titanium butoxide: Synthesis, Pt addition, structural stability, microelectronic processing and gas-sensing properties. Sens. Actuator B 130 (2008) 599-608.

[3] E. Sennik, N. Kilinc, Z.Z. Ozturk. Electrical and VOC sensing properties of anatase and rutile TiO_2 nanotubes. J. Alloys Compd. 616 (2014) 89-96. .

[4] R. Zhao, L. Zhu, F. Cai, Z. Yang, X. Gu, J. Huang, L. Cao. ZnO/TiO_2 core-shell nanowire arrays for enhanced dye-sensitized solar cell efficiency. Appl. Phys. A Mater. Sci. Process. 113 (2013) 67-73.

[5] G.K.L. Goh, H.Q. Le, T.J. Huang, B.T.T. Hui. Low temperature grown ZnO@TiO_2 core shell nanorod arrays for dye sensitized solar cell application. J. Solid State Chem. 214 (2014) 17-23.

[6] L.E. Greene, M. Law, B.D. Yuhas, P. Yang. ZnO-TiO_2 core-shell nanorod/P3HT solar cells. J. Phys. Chem. C 111 (2007) 18451-18456.

[7] T. Kawaharamura, K. Mori, H. Orita, T. Shirahata, S. Fujita, T. Hirao. Effect of O_3 and aqueous ammonia on crystallization of MgO thin film grown by mist chemical vapor deposition. Jpn. J. Appl. Phys. 52 (2013) 035501.

[8] Q. Zhang, C. Li. Pure anatase phase titanium dioxide films prepared by mist chemical vapor deposition. Nanomaterials 8 (2018) 827.

[9] Q. Zhang, C. Li. Effect of substrates on structural properties of pure anatase phase titanium dioxide thin films prepared by mist chemical vapor deposition. ECS J. Solid State Sci. Technol. 7 (2018) P654-P659.

[10] S.E. Ahn, J.S. Lee, H. Kim, S. Kim, B.H. Kang, K.H. Kim, G.T. Kim. Photoresponse of sol-gel-synthesized ZnO nanorods. Appl. Phys. Lett. 84 (2004) 5022-5024.

[11] T. Okada, B.H. Agung, Y. Nakata. ZnO nano-rods synthesized by nano-particle-assisted pulsed-laser deposition. Appl. Phys. A 79 (2004) 1417-1419.

[12] X. Liu, X. Wu, H. Cao, R.P.H. Chang. Growth mechanism and properties of ZnO nanorods synthesized by plasma-enhanced chemical vapor deposition. J. Appl. Phys. 95 (2004) 3141-3147.

[13] A. Yengantiwar, R. Sharma, O. Game, A. Banpurkar. Growth of aligned ZnO nanorods array on ITO for dye sensitized solar cell. Curr. Appl. Phys. 11 (2011) S113-S116.

[14] S. Chu, D. Li, P.-C. Chang, J.G. Lu. Flexible dye-sensitized solar cell based on vertical ZnO nanowire arrays. Nanoscale Res. Lett. 6 (2011) 38.

[15] V.-M. Guérin, J. Rathousky, T. Pauporté. Electrochemical design of ZnO hierarchical structures for dye-sensitized solar cells. Sol. Energy Mater. Sol. Cells 102 (2012) 8-14.

[16] M. Thambidurai, N. Muthukumarasamy, D. Velauthapillai, C. Lee. Chemical bath deposition of ZnO nanorods for dye sensitized solar cell applications. Journal of Materials Science: Materials in Electronics 24 (2013) 1921-1926.

[17] G.R. Patil, R.S. Gaikwad, M.B. Shelar, R.S. Mane, S.H. Han, B.N. Pawar. Role of concentration and temperature on well-aligned ZnO nanorod by low-temperature wet chemical bath deposition method. Archives of Physics Research 3 (2012) 401-406.

[18] X. Li, C. Li, T. Kawaharamura, D. Wang, N. Nitta, M. Furuta, H. Furuta, A. Hatta. Influence of substrates on formation of zinc oxide nanostructures by a novel reducing annealing method. Nanosci. Nanotechnol. Lett. 6 (2014) 174-180.

[19] X. Li, C. Li, S. Hou, A. Hatta, J. Yu, N. Jiang. Thickness of ITO thin film influences on fabricating ZnO nanorods applying for dye-sensitized solar cell. Compos. Part B Eng. 74 (2015) 147-152.

[20] S. Hou, C. Li. Aluminum-doped zinc oxide thin film as seeds layer effects on the alignment of zinc oxide nanorods synthesized in the chemical bath deposition. Thin Solid Films 605 (2016) 37-43.

[21] S. Hou, C. Li. Fabricated ZnO Nanorods on transparent conductive Ga-Doped ZnO film as photoanodes applying for dye-sensitized solar cell. Nanosci. Nanotechnol. Lett. 8 (2016) 561-566.

[22] C. Li, T. Kawaharamura, T. Matsuda, H. Furuta, T. Hiramatsu, M. Furuta, T. Hirao. Intense green cathodoluminescence from low-temperature-deposited ZnO film with fluted hexagonal cone nanostructures. Appl. Phys. Express 2 (2009) 091601.

[23] C.T. Lee. Fabrication methods and luminescent properties of ZnO materials for light-emitting diodes. Materials (Basel) 3 (2010) 2218-2259.

[24] Y. Liang, S. Wicker, X. Wang, E.S. Erichsen, F. Fu. Organozinc precursor-derived crystalline ZnO nanoparticles: synthesis, characterization and their spectroscopic properties. Nanomaterials 8 (2018) 22.

[25] S. Vijayalakshmi, S. Venkataraj, R. Jayavel. Characterization of cadmium doped zinc oxide (Cd: ZnO) thin films prepared by spray pyrolysis method. J. Phys. D: Appl. Phys. 41 (2008) 245403.

[26] L. Saikia, D. Bhuyan, M. Saikia, B. Malakar, D.K. Dutta, P. Sengupta. Photocatalytic performance of ZnO nanomaterials for self sensitized degradation of malachite green dye under solar light. Appl. Catal. A Gen. 490 (2015) 42-49.

[27] Y. Mi, Y. Weng. Band alignment and controllable electron migration between rutile and anatase TiO_2. Sci. Rep. 5 (2015) 1-10.

[28] S.A.M. Lima, F.A. Sigoli, M. Jafelicci Jr, M.R. Davolos. Luminescent properties and lattice correlation defects on zinc oxide. Int. J. Inorg. Mater. 3 (2001) 749-754.

[29] R.S. Reddy, A. Sreedhar, A.S. Reddy, S. Uthanna. Effect of film thickness on the structural morphological and optical properties of nanocrystalline ZnO films formed by RF magnetron sputtering. Adv. Mater. Lett. 3 (2012) 239-245.

Chapter 6

Gas sensitivity characterization of TiO_2 thin films

6.1 Introduction

In chapter 3 and chapter 4, pure anatase phase TiO_2 thin films with good uniformity, good crystallinity, excellent thermal stability and enhanced {001} facets were successfully synthesized by mist CVD. In this chapter, the gas sensitivity of TiO_2 thin films to ethanol vapor was investigated.

As a typical n-type semiconductor, TiO_2 shows an extensive gas sensitivity to both oxidative gases and reductive gases. When TiO_2 is heated to the required higher operating temperature in ambient air, due to the surface oxygen vacancies, oxygen molecules are easily absorbed on the surface of TiO_2 and thereby through this oxidation process will be trapping electrons from the conduction band to form anionic oxygen. This oxidation process on the surface of TiO_2 leads to a decrease of the electron density, as shown in Equation (6.1) [1]. As the oxidation process continues at steadily higher temperatures, additional adsorbed oxygen molecules will attract more electrons, thereby promoting more electron transfer from the TiO_2 conduction band and form O^- and O^{2-} ions as shown in Equation (6.2) and Equation (6.3) [1]. In the following step after exposure to the reducing target gas to be tested, oxygen ions react with the target gas molecules and electrons are transferred back to the TiO_2 conduction band, which increases the electron density. In other words, in this process step the reductant transfers electrons to the oxidant TiO_2. The detailed explanation of this reduction reaction is shown as Equation (6.4) [1].

$$O_2(gas) + e^- \leftrightarrow O_2^-(adsorption) \quad (6.1)$$

$$\frac{1}{2}O_2 + e^- \leftrightarrow O^-(adsorption) \quad (6.2)$$

$$\frac{1}{2}O_2 + 2e^- \leftrightarrow O^{2-}(adsorption) \quad (6.3)$$

$$X + O^{\delta-} \leftrightarrow X' + \delta e^{-} \quad (6.4)$$

where X is the target gas, X' the gas after the reaction, δ the number of electron, which depends on the reaction as shown in Equation (6.2) and Equation (6.3).

The schematics of Fig. 6.1a and Fig. 6.1b explain the detailed oxidation step on the surface of the and electron adsorption from the conduction band to form an oxygen ion layer on the surface of TiO_2 nanosheet. This oxidation step leads to a decrease in the electron density (lose of electrons) on the exposed active TiO_2 surface, which will cause the formation of depletion layer on the surface. The band bending on TiO_2 surface will bring a barrier for carrier transport between the particles, which will cause the decrease of film conductivity.

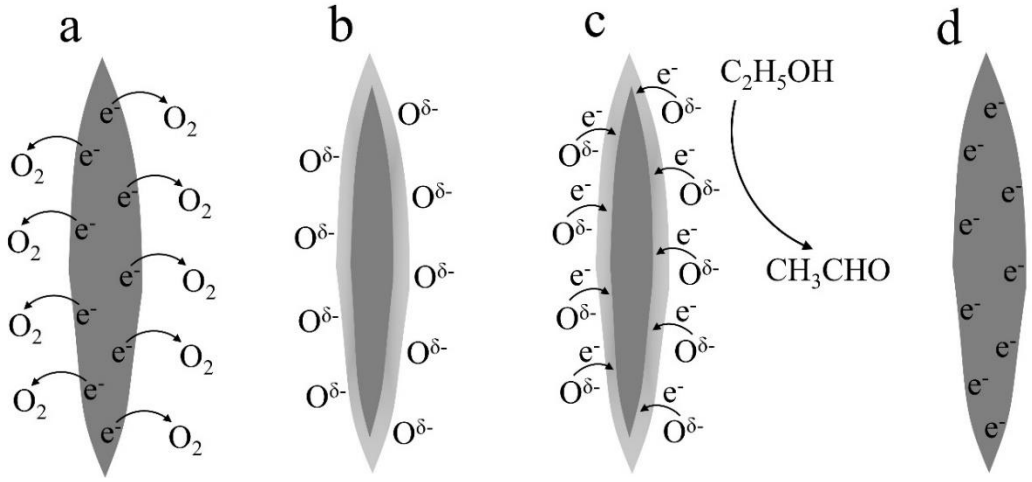

Fig. 6.1 Schematic depiction of the sensing mechanism of TiO_2 nanosheet exposed to ethanol vapors.

Then the third step is to introduce the reducing target gas to be tested (in our case ethanol) to the gas sensor in a controlled test equipment environment. As shown in the schematics of Fig. 6.1c and Fig. 6.1d, the ethanol molecules react with the oxygen ions on the TiO_2 surface, thereby reducing the oxygen ions and causing a transfer of electrons back to the TiO_2 conduction band. Following this process step, the electron (majority carrier in TiO_2) concentration in the conduction band increases. As a result, the thickness of the depletion layer decreases (as shown in Fig. 6.2), which leads to an increase in conductivity (or equivalently a decrease in resistivity) [2-10].

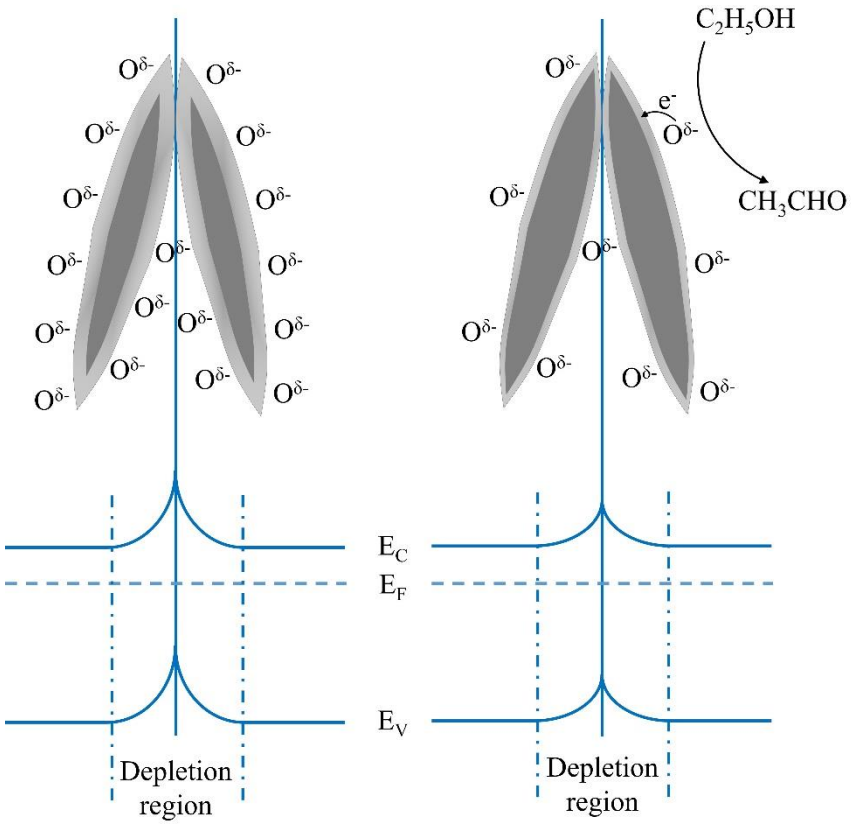

Fig. 6.2 Schematics of band diagram compared with the grain boundary when TiO_2 nanosheets surface is exposed to oxygen and ethanol vapor.

Figure 6.3 shows a TiO_2 gas sensor after exposure to ethanol vapor. Initially TiO_2 gas sensor was heated in air to form oxygen negative ions on the surface, which causes the change in resistance. The TiO_2 gas sensor experiences an increase in the resistance during the oxidation process due to the interaction with oxygen leading to a decrease in the electron concentration.

When a target gas (reducing gas) is introduced into the TiO_2 gas sensor, the gas molecules interact with the oxygen ions on the semiconductor surface and electrons are released back into the conduction band, which leads to an increase in the electron concentration. The result shows the resistance of TiO_2 decreases as the electron concentration increases after the surface interaction with the target gas [1].

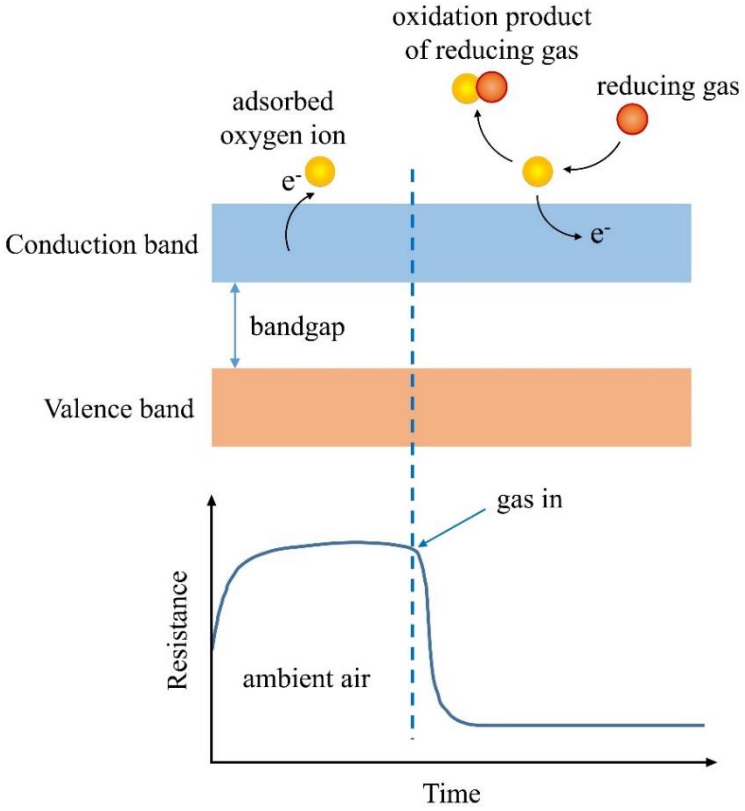

Fig. 6.3 Schematic diagram of the TiO_2 sensor upon exposure to the reducing gas.

6.2 Experimental

Pure anatase phase TiO_2 thin films were fabricated on p-type silicon substrates with different TTIP concentrations. The deposition condition of TiO_2 thin films were the same as that discussed in section 3.3. After fabrication, the gas sensitivity measurement was performed with a homemade measurement system at Old Dominion University. The instrument of gas sensitivity measurement system was introduced in chapter 2. The measurement was carried out with ethanol vapor with working temperature from 100 °C to 320 °C. The resistivity of samples in the atmosphere of ethanol was recorded to evaluate the gas sensitivity. The reponse of samples to ethanol vapor was calculated from resistivity of samples by following equation:

$$Response = \frac{R_{air} - R_{gas}}{R_{air}} \tag{6.5}$$

where R_{air} is the resistance of sample exposed in air, R_{gas} is the resistance of sample exposed in target gas (ethanol vapor).

6.3 Results and discussion

Figure 6.4 shows the gas sensitivity measurement result (with different working temperatures) of TiO_2 film deposited with a TTIP concentration of 0.40 mol/L. With the working temperature increased 100 °C to 200 °C, the ethanol vapor sensitivity of TiO_2 film was almost same. With the working temperature increased 200 °C to 320 °C, the ethanol vapor sensitivity of TiO_2 film first increased then decreased, and the highest sensitivity of TiO_2 film was obtained with a working temperature of 300 °C. The film deposited with different TTIP concentrations showed the same optimum working temperature of 300 °C.

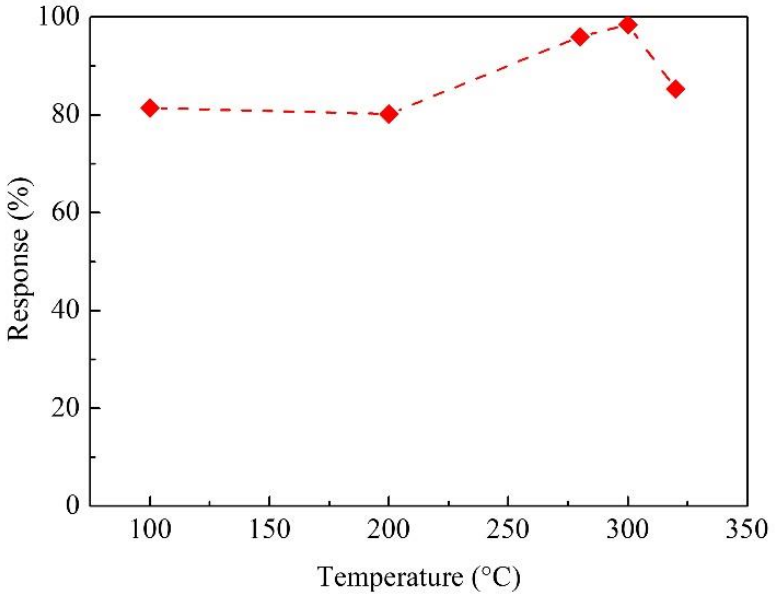

Fig. 6.4 Gas sensitivity measurement result (with different working temperatures) of TiO_2 films deposited with a TTIP concentration of 0.40 mol/L

Figure 6.5 shows the result of gas sensitivity measurement (with a working temperature of 320 °C) of TiO_2 film deposited with a TTIP concentration of 0.40 mol/L. The TiO_2 film showed a high response around 85.3 % to ethanol vapor with a working temperature of 320 °C. The recovery time (at 320 °C) of TiO_2 film deposited with a TTIP concentration of 0.40 mol/L was around 140 s.

Figure 6.6 shows the result of gas sensitivity measurement (with the optimum working temperature of 300 °C) of TiO_2 films deposited with different TTIP concentrations. With TTIP concentration increased from 0.05 mol/L to 0.10 mol/L, the sensitivity of TiO_2 film increased. With TTIP concentration increased from 0.10 mol/L to 0.20 mol/L, the sensitivity of TiO_2 film

increased slightly. With TTIP concentration increased from 0.20 mol/L to 0.30 mol/L, the sensitivity of TiO_2 film decreased dramaticly. With TTIP concentration increased from 0.30 mol/L to 0.40 mol/L, the sensitivity of TiO_2 film increased to the same level as that of TiO_2 film deposited with a TTIP concentration of 0.05 mol/L.

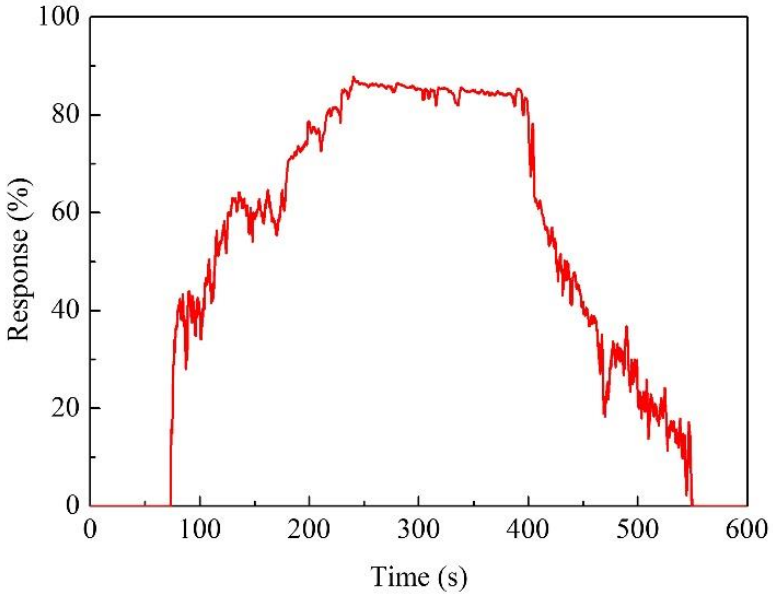

Fig. 6.5 Gas sensitivity measurement result (with a working temperature of 320 °C) of TiO_2 films deposited with a TTIP concentration of 0.40 mol/L.

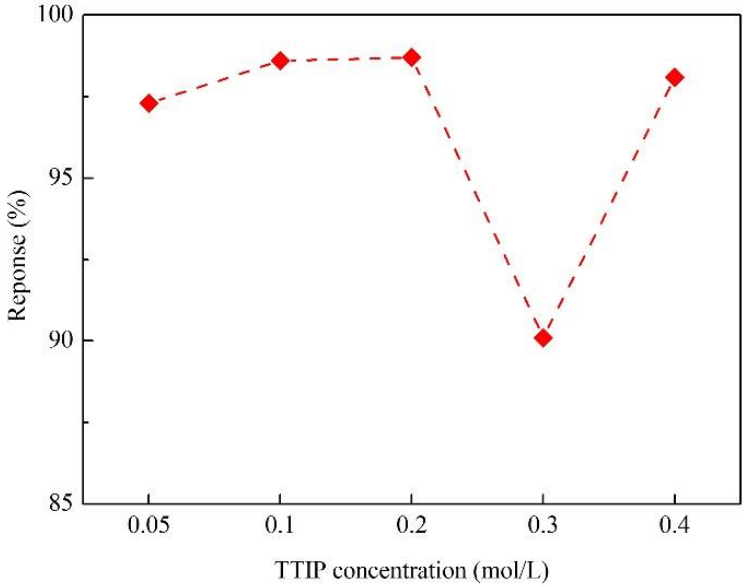

Fig. 6.6 Gas sensitivity measurement result (with a working temperature of 300 °C) of TiO_2 films deposited with different TTIP concentrations.

6.4 Conclusions

The ethanol vapor sensitivity of TiO_2 at different working temperatures was investigated. With the working temperature increased from 100 °C to 320 °C, the ethanol vapor sensitivity of TiO_2 film first increased then decreased. The TiO_2 film deposited with different TTIP concentrations showed the same optimum working temperature of 300 °C. Compared with other samples, the TiO_2 deposited with a TTIP concentration of 0.20 mol/L showed optimum sensitivity to ethanol vapor at 300 °C.

6.5 References

[1] C. Supab, H. Niyom, W. Ekasiddh. Metal-oxide nanowires for gas sensor. Nanowires-Recent Advances, Chapter 1 (2012).

[2] L.W. Wang, Y.F. Kang. ZnO Nanorods gas sensor for ethanol detection. Sensors and Actuator B 162 (2012) 237-243.

[3] G. Sakai, N. Matsunaga, K. Shimanoe, N. Yamazoe. Theory of gas-diffusion controlled sensitivity for thin film semiconductor gas sensor. Sens. Actuators B Chem. 80 (2001) 125-131.

[4] J.R. Brown, M.T. Cheney, P.W. Haycock, D.J. Houlton, A.C. Jones, E.W. Williams. The gas-sensing properties of tin oxide thin films deposited by metallorganic chemical vapor deposition. J. Electrochem. Soc. 144 (1997) 295-299.

[5] M.V. Baryshnikova, L.A. Filatov, A.S. Petrov, S.E. Alexandrov. CVD deposited titania thin films for gas sensors with improved operating characteristics. Chem. Vap. Depos. 21 (2015) 327-333.

[6] J. Zhang, C. Zhao, P.A. Hu, Y.Q. Fu, Z. Wang, W. Cao, B. Yang, F. Placido. A UV light enhanced TiO_2/graphene device for oxygen sensing at room temperature. RSC Adv. 3 (2013) 22185-22190.

[7] B. Comert, N. Akin, M. Donmez, S. Saglam, S. Ozcelik. Titanium dioxide thin films as methane gas sensors. IEEE Sens. J. 16 (2016) 889-8896.

[8] D.S.R. Josephine, K.J. Babu, G.P.G. Kumar, K. Sethuraman. Titanium dioxide anchored graphene oxide nanosheets for highly selective voltammetric sensing of dopamine. Microchim. Acta 184 (2017) 781-790.

[9] M. Epifani, A. Helwig, J. Arbiol, R. Díaz, L. Francioso, P. Siciliano, G. Mueller, J.R. Morante. TiO_2 thin films from titanium butoxide: Synthesis, Pt addition, structural stability, microelectronic processing and gas-sensing properties. Sens. Actuator B 130 (2008) 599-608.

[10] E. Sennik, N. Kilinc, Z.Z. Ozturk. Electrical and VOC sensing properties of anatase and rutile TiO_2 nanotubes. J. Alloys Compd. 616 (2014) 89-96.

Chapter 7

Conclusions

In this thesis, the fabrication of pure anatase phase TiO_2 thin films in applications of gas sensors was investigated to solve the shortcomings and technical challenges in current state-of-the-art TiO_2 gas sensors.

Pure anatase phase TiO_2 thin films with good uniformity, good crystallinity, excellent thermal stalibity and optimum {001} facets were fabricated by a novel designed mist chemical vapor deposition system. To further increase the surface-to-volume ratio of TiO_2, TiO_2 films were coated onto ZnO nanorods to fabricate ZnO/TiO_2 core-shell nanostructures.

The main conclusions of this thesis were summarized as followed:

1. Fabrication of anatase phase TiO_2 thin films with ethanol as solvent

In this part, pure anatase phase TiO_2 films were fabricated with ethanol as solvent by mist CVD. The effects of deposition temperature, concentration of TTIP, film thickness and substrate on the properties of TiO_2 films were investigated.

The crystallinities of TiO_2 films were significantly improved by increasing deposition temperature. Pure anatase phase TiO_2 films with good uniformity were obtained from 300 °C to 400 °C. The roughnesses of all TiO_2 films were less than 7 nm and showed a variation tendency of increase as the deposition temperature increased from 200 °C to 400 °C.

When the concentration of TTIP increased from 0.05 mol/L to 0.40 mol/L, the aspect ratio of TiO_2 nanosheets first increased then decreased. The highest aspect ratio of TiO_2 nanosheets was obtained at a titanium tetraisopropoxide concentration of 0.20 mol/L. The deposition rate of TiO_2 films had the same variation tendency with aspect ratio. The roughnesses of all TiO_2 films were less than 10 nm regardless of TTIP concentration variation. The crystallinity of TiO_2 films showed a variation tendency of increase as the TTIP concentration increased from 0.05 mol/L to 0.40 mol/L. The best crystallinity was obtained under the titanium tetraisopropoxide concentration of 0.05 mol/L.

The crystallinity of TiO_2 films increases with the increasing of film thickness. The transmittance of all TiO_2 films is more than 75% in the visible region and almost independent of film thickness. The surface of obtained TiO_2 films with different thicknesses are uniform. With the thickness increasing, the roughness of TiO_2 film shows tendency of increase.

The TiO_2 films deposited on all substrates showed the same dominant (101) growth orientation. The crystallinity of TiO_2 films grown on different substrates increased in an order of glass, quartz glass, p-type silicon and GZO. It was confirmed by Raman spectroscopy that TiO_2 films deposited on four kinds of substrates were pure anatase phase, which was in a good agreement with the GIXRD result. The TiO_2 thin film deposited on p-type silicon showed the highest percentage of exposed {001} facets. The TiO_2 films with good uniformity were obtained on all of the substrates. The surface area of TiO_2 films deposited on p-type silicon substrate was larger than that of TiO_2 films deposited on quartz glass, glass and GZO substrates. The precise control of the growth orientation, uniformity and grain size of thin film were achieved. The transmittance of TiO_2 films on quartz glass, glass and GZO substrates was higher than 75% in the visible region.

2. Fabrication of anatase phase TiO_2 thin films with methanol as solvent

In this part, pure anatase phase TiO_2 films were fabricated on AZO and glass substrates with methanol as solvent by mist CVD. The effects of film thickness and water-to-methanol ratio on the properties of TiO_2 films were investigated.

Uniform TiO_2 films with different thicknesses were obtained. With the thickness increasing, the roughness and crystallinity of TiO_2 film showed tendency of increase. The of TiO_2 films increases with the increasing of film thickness. With the thickness increasing, the transmittance of TiO_2 films decreased from around 80 % to around 65 % gradually.

During the deposition, the growth of {001} facets and surface area were significantly influenced by the water-to-methanol ratio. By decreasing the water-to-methanol ratio, the growth of {001} facets was enhanced, while the growth of {101} facets was suppressed. The surface roughness and surface area of TiO_2 films showed the same trend of increasing with a decrease of the water-to-methanol ratio. The highest surface roughness and maximized surface area was obtained with pure methanol as solvent. The transmittance of all TiO_2 films was higher than 70 % in the visible region. The photocatalytic efficiency of TiO_2 film showed an increasing trend with the decrease of the water-to-methanol ratio. The TiO_2 film deposited with a water-to-methanol of 0 % showed the highest photocatalytic efficiency due to a maximum number of {001} facets and an optimum surface area.

Uniform TiO_2 films with different thicknesses were obtained. With the thickness increasing, the roughness and crystallinity of TiO_2 film showed tendency of increase. The of TiO_2 films increases with the increasing of film thickness. With the thickness increasing, the transmittance of TiO_2 films decreased from around 80 % to around 65 % gradually.

3. Fabrication of ZnO nanorods and ZnO/TiO_2 core-shell nanorods.

In this part, well-arrayed ZnO nanorods and well-arrayed ZnO/TiO_2 core-shell nanorods were fabricated on AZO films. The effects of solution concentration and deposition time on the properties of ZnO nanorods were investigated. The effects of TiO_2 film coating time on the properties of ZnO/TiO_2 core-shell nanorods were investigated.

The solution concentration had a significant influence on the morphological, structural, and optical properties of ZnO nanorods. It was found that well-arrayed ZnO nanorods with hexagonal structure were obtained with solution concentration from 100 % to 40 %. With the decreasing of solution concentration, the crystallinity of ZnO nanorods showed a tendency of decrease, and the transmittance of ZnO nanorods increased gradually in visible range.

The morphological, structural and optical properties of ZnO nanorods were significantly influenced by the deposition time. Well-arrayed ZnO nanorods with hexagonal structure were obtained with with deposition time of 5 hours and 10 hours. With the deposition time increasing from 5 hours to 10 hours, the crystallinity of ZnO nanorods increased significantly, and the transmittance of ZnO nanorods in the visible region decreased from around 75 % to around 35 %.

TiO_2 layer was successfully coated on ZnO nanorods. The TiO_2 shells on ZnO nanorods were confirmed as pure anatase phase, which will contribute to high chemical stability and good sensing properties. The surface area of ZnO nanorods was significantly increased with increase in TiO_2 coating time. The transmittance of ZnO nanorods decreased from 75 % to 65 % after 15 minutes coating TiO_2. The well-arrayed ZnO/TiO_2 core-shell nanorods will contribute to an excellent chemical stability, and relatively large surface-to-volume ratio for gas absorption, which are expected to applied as sensing material to improve the performance of gas sensors.

4. Sensitivity characterization of TiO_2 thin films

In this part, the sensing properties of TiO_2 thin film to ethanol vapor at different working temperatures were investigated. With the working temperature increased from 100 °C to 320 °C, the ethanol vapor sensitivity of TiO_2 film first increased then decreased. All of TiO_2 films showed the same optimum working temperature of 300 °C regardless of TTIP concentration variation. The TiO_2 deposited with a TTIP concentration of 0.20 mol/L showed optimum sensitivity to ethanol vapor.

List of publications

(A) Peer reviewed journal papers

First author:

1) Effects of Water-to-Methanol Ratio on the Structural, Optical and Photocatalytic Properties of Titanium Dioxide Thin Films Prepared by Mist Chemical Vapor Deposition.
Qiang Zhang, Chaoyang Li
Catalysis Today, (In Press, online). (JCR Q1, IF=4.888)

2) TiO_2 Coated ZnO Nanorods by Mist Chemical Vapor Deposition for Application as Photoanodes for Dye-Sensitized Solar Cells.
Qiang Zhang, Chaoyang Li
Nanomaterials, 9, 1339 (2019). (JCR Q1, IF=4.034)

3) Effect of Substrates on Structural Properties of Pure Anatase Phase Titanium Dioxide Thin Films Prepared by Mist Chemical Vapor Deposition.
Qiang Zhang, Chaoyang Li
ECS Journal of Solid State Science and Technology, P654-P659, 37-43 (2018). (JCR Q2, IF=1.795)

4) Pure Anatase Phase Titanium Dioxide Films Prepared by Mist Chemical Vapor Deposition.
Qiang Zhang, Chaoyang Li
Nanomaterials, 8, 827 (2018). (JCR Q1, IF=4.034)

(B) Proceeding papers

First author:

1) Effects of Water-to-Methanol Ratio on the Structural, Optical and Photocatalytic Properties of Titanium Dioxide Thin Films Prepared by Mist Chemical Vapor Deposition.
Qiang Zhang, Chaoyang Li, Taishi Nakamura, Masaya Morimoto
2019 26th International Workshop on Active-Matrix Flatpanel Displays and Devices (AM-FPD), 1-2 (2019).

2) Effect of Substrates on Structural Properties of Pure Anatase Phase Titanium Dioxide Thin Films Prepared by Mist Chemical Vapor Deposition.
Qiang Zhang, Chaoyang Li
ECS Transactions, 85, 113-118 (2018).

3) Effects of deposition temperature and thermal annealing on the structural properties of titanium dioxide thin films prepared by mist chemical vapor deposition.

Qiang Zhang, Chaoyang Li

2017 24th International Workshop on Active-Matrix Flatpanel Displays and Devices (AM-FPD), 244-246 (2017).

Co-author:

1) Titanium Dioxide Thin Film Coated ZnO Nanorods for Sensitivity Improvement Applying for Displays.

Chaoyang Li, **Qiang Zhang**

SID Symposium Digest of Technical Papers, 49, 1616-1618 (2018).

2) Low-temperature Fabrication of ZnO Nanorods Using Chemical Bath Deposition Method for Sensing Application in Display.

Chaoyang Li, **Qiang Zhang**

SID Symposium Digest of Technical Papers, 50, 1630-1633 (2019).

(C) International conferences with proceeding

First author:

1) Effects of water-to-methanol ratio on the structural, optical and photocatalytic properties of titanium dioxide thin films prepared by mist chemical vapor deposition.

Qiang Zhang, Chaoyang Li

Third International Conference on Catalysis and Chemical Engineering, February 2019, Houston, USA. (Poster presentation).

2) ZnO Nanorods Fabricated by Chemical Bath Deposition for Dye-sensitized Solar Cell Application

Qiang Zhang, Chaoyang Li, Taishi Nakamura, Masaya Morimoto

The 26th International Workshop on Active-Matrix Flatpanel Displays and Devices (AM-FPD-19), July 2019, Kyoto, Japan. (Poster presentation).

3) Effect of Substrates on Structural Properties of Pure Anatase Phase Titanium Dioxide Thin Films Prepared by Mist Chemical Vapor Deposition.

Qiang Zhang, Chaoyang Li

233rd ECS, May 2018, Seattle, USA. (Oral presentation)

4) Effects of Solution Concentration on the Structural and Optical Properties of Titanium Dioxide Thin Films Prepared by Mist Chemical Vapor Deposition.

Qiang Zhang, Chaoyang Li

IUMRS-ICAM 2017, August 2017, Kyoto, Japan. (Oral presentation, Winner of Award for encouragement of research)

5) Effects of Deposition Temperature and Thermal Annealing on the Structural Properties of Titanium Dioxide Thin Films Prepared by Mist Chemical Vapor Deposition.

Qiang Zhang, Chaoyang Li

The 24th International Workshop on Active-Matrix Flatpanel Displays and Devices (AM-FPD-17), July 2017, Kyoto, Japan. (Poster presentation)

Co-author:

1) Low-temperature Fabrication of ZnO Nanorods Using Chemical Bath Deposition Method for Sensing Application in Display.

Chaoyang Li, **Qiang Zhang**

SID Symposium Digest of Technical Papers, 50, 1630-1633 (2019).

2) Titanium Dioxide Thin Film Coated ZnO Nanorods for Sensitivity Improvement Applying for Displays.

Chaoyang Li, **Qiang Zhang**

SID Symposium Digest of Technical Papers, 49, 1616-1618 (2018).

(D) Domestic conferences with proceeding as first author:

First author:

1) Effects of Oxygen on the Structural Properties of Zinc Oxide Films on AZO Substrate Prepared by Radio Frequency Magnetron Sputtering

Qiang Zhang, Chaoyang Li

SPP36/SPSM31, January 2019, Kochi, Japan. (Oral presentation).

2) Effects of Solution Concentration on the Growth of Zinc Oxide Nanorods Prepared by Chemical Bath Deposition

Qiang Zhang, Chaoyang Li

MRS-J 2017, December 2017, Yokohama, Japan. (Oral presentation).

Acknowledgements

I would like to express my sincere gratitude to my supervisor Prof. Chaoyang Li for her brilliant guidance and endless support during my Ph.D. study and research. She is a tremendous mentor to me. Her advice on both research as well as on my career has been priceless. Her strict attitude to research makes me a better researcher. I have learned so much from her on both research and lifestyle. I am honored to be one of her students.

I would also like to thank my co-supervisors, Prof. Toshiyuki Kawaharamura and Prof. Hiroshi Furuta for their helpful comments and suggestions in my research. Their support to my experiments and analysis makes my research smooth and efficient.

I would like to thank my committee members, Prof. Helmut Baumgart and Prof. Akimitsu Hatta for the support of doing the research in their laboratory. In addition, I would like to thank Prof. Mamoru Furuta for the support while doing my research in the cleanroom. My sincere appreciations are extended, to Associate Prof. Hisao Makino for the support of XRD measurement.

I would also like to give my special appreciations to my senior, Dr. Shengwen Hou and Dr. Xin Li for their excellent guidance and support in my research. They have mentored me to be a real researcher.

I would like to thank the staff of International Relation Division of KUT. They made my life in Japan convenient and colourful. I have experienced many aspects of traditional Japanese culture with their support. They helped me experience a totally different and exciting Japan.

I would also like to thank all of my friends who supported me in doing experiment, analysis, and writing as well as cheering me up when I was upset with the problems I cannot solve. They are really like my family in this university. They colour my social life. I cherish all the valuable moments we had together.

A special thank you is due for my family. Words cannot express how grateful I am to my wife for all of the sacrifices that she had made on my behalf. Her understanding and support sustained me the whole time.